Spring 2019

Optical Excitation of Metastable Krypton and Photoassociative Spectroscopy of Ultracold RbAr

Grady R. White
Old Dominion University

OPTICAL EXCITATION OF METASTABLE KRYPTON AND PHOTOASSOCIATIVE SPECTROSCOPY OF ULTRACOLD RbAr

by

Grady R. White
B.A. May 2008, St. Mary's College of Maryland
M.S. May 2011, Old Dominion University

A Dissertation Submitted to the Faculty of
Old Dominion University in Partial Fulfillment of the
Requirements for the Degree of

DOCTOR OF PHILOSOPHY

PHYSICS

OLD DOMINION UNIVERSITY
May 2019

Approved by:

Charles Sukenik (Director)

David Burdige (Member)

Alexander Godunov (Member)

Charles Hyde (Member)

Lepsha Vuskovic (Member)

ABSTRACT

OPTICAL EXCITATION OF METASTABLE KRYPTON AND PHOTOASSOCIATIVE SPECTROSCOPY OF ULTRACOLD RbAr

Grady R. White
Old Dominion University, 2019
Director: Dr. Charles Sukenik

In this dissertation we discuss results from two separate bodies of work. In the first, we investigate all-optical excitation methods to produce metastable-state krypton. The high energies required to excite rare gases out of their ground state present a unique challenge in the context of laser experiments. Laser physics work with rare gases often relies on excitation within an rf discharge. All-optical excitation is a promising replacement for RF discharges, avoids problems caused by ion production, and may eventually allow for higher efficiencies. We examine three separate methods of all-optical metastable-state production: using an ArF excimer laser, using the third harmonic of the Jefferson Lab free-electron laser (FEL), and using a commercially available UV lamp. In the second body of work, we perform photoassociation spectroscopy in an ultracold, hetero-nuclear Rb + Ar^* system. Photoassociation is a method that may be used to both 1) produce ultracold molecules, and 2) perform high-resolution spectroscopy on excited molecular states. Most work within the field has been performed within all alkali-metal systems. We examine a unique noble gas alkali system within a dual species magneto-optical trap. We have performed a comprehensive search for evidence of excitation to molecular levels of RbAr. We illuminate atom pairs with a photoassociation laser in a spectral region detuned a few GHz below an atomic asymptote of argon, analogous to previous work in the homonuclear argon or krypton systems. We discuss our methodology and findings. We conclude with a discussion of how our results may be applied to future spectroscopic searches.

ACKNOWLEDGEMENTS

First and foremost, I must acknowledge the love, patience, and support that my wife has given me throughout my time in graduate school. I am beyond lucky to have her in my life.

I am profoundly grateful for the guidance of Dr. Charles Sukenik, who mentored me from a budding graduate student into a physicist. He has seemingly limitless expertise in experimental work, of which he endeavored to transfer as much as he could to me. His former postdoc, Dr. Will Williams, was and continues to be of immense help, especially during my first two years in the group. Thank you to Jack Mills and Josh Frechem for their hands-on contributions that they made to my work, and to Aye Lu Win, Maha Omar, Stetson Roof, Lindsay Thornton, Jeremy Peshl, and Christian Shultz for their companionship through the years.

Thank you to my committee members, Dr. David Burdige, Dr. Alexander Godunov, Dr. Charles Hyde, and Dr. Lepsha Vuskovic, who provided invaluable feedback.

In addition, much of the work would not have been possible without help from outside collaborators. I am very grateful for the opportunities and financial support made possible by Dr. Z.-T. Lu, Dr. Wei Jiang, and the rest of the ATTA team at Argonne National Laboratory. Here in Hampton Roads, I must acknowledge the generous contributions made by the late Jeff Balla at NASA Langley, and the FEL staff at Jefferson Lab.

I have tremendous gratitude to my parents and the rest of my family for their continuous enthusiasm and encouragement. And finally, thank you to my two cats, Garfield and Oreo, for ensuring that I never slept in...

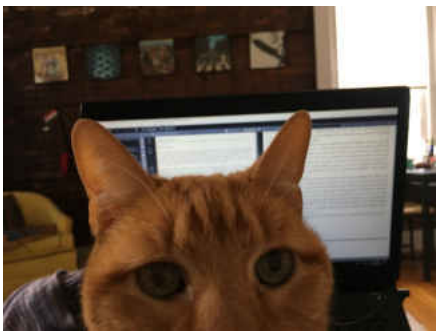

TABLE OF CONTENTS

Page

LIST OF TABLES

LIST OF FIGURES

CHAPTER 1

INTRODUCTION

This dissertation covers two separate projects. They are linked in that both rely on similar techniques to work with noble gases that are in long-lived atomic states known as metastable states, but are otherwise independent of each other. The first project is a study of three separate all-optical methods to excite ground state Kr atoms into a metastable state. Several non-optical techniques currently exist, however each method comes with its own set of benefits and drawbacks. We examine these schemes with the hope of eventually making Kr atoms easier to work with in table-top atomic physics experiments. An application of particular note is Atom Trap Trace Analysis (ATTA), which uses metastable Kr samples to radiokrypton date water samples. The second project is photoassociation spectroscopy within a dual species Rb + Ar^* magneto-optical trap. We scan a photoassociation laser across a wide frequency range, and search for excited molecular spectra. Our system is unusual in that it consists of an alkali-metal and a metastable rare gas.

1.1 METASTABLE KR BACKGROUND

Access to fresh water has been a continual concern to societies across the world. In the future, overexploitation and climate change are likely to make fresh water access an issue of global prominence. Underground aquifers are, and will continue to be, an invaluable resource that demand our care and attention. While groundwater serves as a major source of both drinking water and agricultural water [4], we find that we often have inadequate knowledge of how our aquifers are interconnected with the complex systems around them. By using long-lived radioactive isotopes as tracers, we may determine how long bodies of water have been out of contact with the atmosphere, and map out previously hidden transport mechanisms [5].

Radiocarbon dating is a well-known technique typically used to date the age of organic samples. Initially using ^{14}C, radiocarbon dating relies on the fact that the relative abundance of carbon isotopes in the atmosphere has been steady for millennia. The decay of existing ^{14}C isotopes is balanced by the creation of new

^{14}C via collisions between cosmic radiation and nitrogen. When a sample of carbon is removed from the atmosphere, for example it becomes part of a plant, it loses its source of new ^{14}C isotopes. However, the existing unstable isotopes continue to decay at predictable rates. By comparing the ratio of ^{14}C to the stable ^{12}C, one may determine the age of the sample [6].

Despite its usefulness, radiocarbon dating is not a good fit for determining the length of time that groundwater has been out of contact with the atmosphere. Carbon found within aquifers comes from both organic and inorganic sources, undermining the assumptions made above [7]. Other atoms, however, do not experience this problem. Similar to ^{14}C, krypton has two long-lived radioactive isotopes that may serve as tracers, ^{81}Kr and ^{85}Kr. When water comes into contact with the atmosphere, krypton gas dissolves into it and functions like a time stamp. Production of new ^{81}Kr and ^{85}Kr ceases when the water flows underground. We may measure the length of time that the sample has been removed from the atmosphere by measuring the abundance ratios of these long-lived isotopes to the stable ^{84}Kr isotope. In addition to being a reliable tracer within groundwater, ^{81}Kr and ^{85}Kr have different half-lives than ^{14}C, making them useful over different age ranges. Figure 1 shows the range of ages that a number of different radioisotopic techniques can measure [8].

For several decades, researchers have been using the now well-developed techniques of low level counting [9] and accelerator mass spectrometry [10] to detect trace levels of rare isotopes. Two newer methods include ion-based mass spectroscopy and photon burst mass spectrometry. However, of interest to this work is atom trap trace analysis (ATTA). While each of the mentioned methods has its own strengths and weaknesses, ATTA is unique in its ability to tolerate impurities due to other isotopes and molecules [11].

ATTA is an atom counting method that relies on using narrow bandwidth lasers to access atomic transitions and resonantly scattered photons. The photons are detected and counted with a couple-charged device (CCD) camera. The atomic transitions are narrow and selective enough that very small isotopic shifts ($\sim$ 50 MHz) may be resolved. However, the technique cannot be used at room temperature, where the line widths of each species are Doppler-broadened into each other. The atoms must first be cooled. As atoms enter the ATTA apparatus, they are collimated into an atomic beam by a 2D magneto-optical trap (MOT) before being slowed down within a Zeeman slower, which is described in detail later. The slow atoms emerge into the

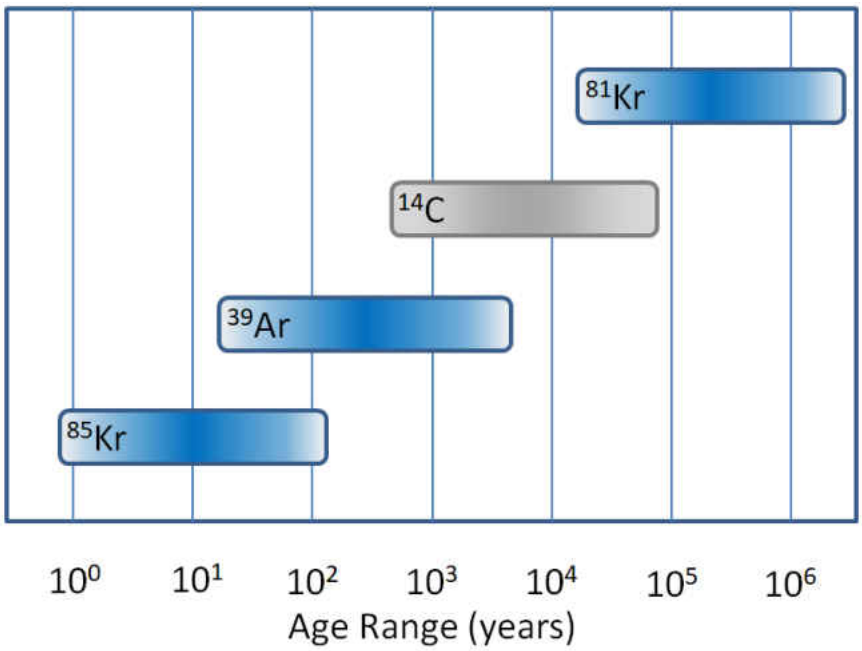

FIG. 1: A diagram displaying the age ranges that the various radioisotope dating methods may measure. ATTA can detect and measure ^{81}Kr, ^{85}Kr, and ^{39}Ar. ^{14}C was included as a reference. The work in this dissertation focused on metastable Kr, so we have not discussed ATTA's ^{39}Ar capabilities.

main vacuum chamber, where they are cooled and trapped within a 3D magneto-optical trap. It is at these ultracold temperatures where counting is performed. The result is a precision in the parts-per-quadrillion range.

While this discussion has revolved around measuring the age of groundwater samples, ATTA is by no means limited to that task. In addition to groundwater [12], the technique has been used to date samples from ocean water and from a glacier. In its previous iteration, ATTA-3, required a sample size of 100 L to 200 L of water. However with recent improvements in efficiency, it is reaching the point where ice core samples from the Arctic and Antarctic may be dated [13].

1.1.1 PREVIOUS WORK EXCITING METASTABLE KRYPTON

ATTA relies on laser cooling to reduce temperatures within Kr samples and minimize Doppler broadening. Once at an ultracold temperature, spectroscopic signatures of each isotope within a sample may be resolved. However, there is an additional

complication when working with Kr gas. Laser cooling requires a closed atomic structure that allows a single electronic transition to be continuously driven. As a noble gas, ground state Kr atoms require a 10 eV photon to excite. Current technology does not provide us with any lasers capable of driving this energic transition within a table-top laboratory experiment. ATTA overcomes this challenge by collisionally exciting Kr atoms within an RF discharge. With an approximate efficiency of 10^{-3}, a portion of the sample is excited to the $5s[3/2]_2$ metastable state, which has a lifetime of about 40 seconds [14]. From the metastable state, the cycling transition $5s[3/2]_2 \rightarrow 5p[5/2]_3$ is accessible, and laser cooling may commence.

The RF discharge adds its own set of complications. Ions created within the plasma are continuously accelerated into the chamber walls, where they become embedded. Simultaneously, the plasma discharge frees previously embedded atoms and releases them into the plasma. The effect can lead to cross contamination between samples via an exchange of atoms. To minimize contamination, the system is flushed with an N_2 discharge for 14 hours between each 10 hour run. Nonetheless, some cross contamination remains and adds to uncertainty in the age of the sample [15].

In a completely different approach, atoms may be excited to the $5s[3/2]_2$ metastable state via a multiphoton excitation. Removing the plasma from the system eliminates the problem of embedded ions and cross contamination, both improving ATTA's up-time and improving its efficiency. In addition, optical excitation methods have the potential to allow for higher excitation efficiencies than the RF discharge currently does. In 2002 L. Young et al. used a homemade plasma lamp in conjunction with a Ti:Sapphire laser to produce metastable Kr within a vapor cell. This was accomplished by relying on a three-photon excitation scheme [16]. Working with Z.-T. Lu's ATTA group in 2007, Young completed a similar experiment within an atomic beam [17]. Unfortunately the home-built lamps had an extremely short working lifetime, and their MgF_2 windows failed after approximately an hour.

In this work we examine three separate optical excitation options. The first option is an ArF excimer laser located at NASA Langley Research Center in Hampton, VA, which produces high intensity 193 nm pulses. The second option is the free-electron laser located at the Thomas Jefferson National Accelerator Facility in Newport News, VA, which has a third harmonic in the 10 eV range we require. The final option is an ultraviolet lamp that is now commercially available, and has the potential to be a reliable alternative to the short-lived home-built lamps previously used.

Midway through testing the commerically built lamp, funding uncertainties compelled us to switch projects and focus on photoassociation spectroscopy, which now makes up the second half of this dissertation. However, in the meantime, other groups have conducted further research on all-optical metastable production, including work that relies on other home-built RF discharge lamps [13][18], and work that relies on 216 nm two-photon excitation before a subsequent decay into the metastable state [19].

1.2 PHOTOASSOCIATION BACKGROUND

In 1975 T. Hansch and A. Schawlow proposed using an exchange of linear momentum between photons and atoms as a method of cooling neutral atoms. By the end of the next decade, researchers had successfully demonstrated cooling of atoms within optical molasses and trapping of atoms within a MOT [20]. Using these methods, ultracold temperatures (< 1 mK) were achieved. Since then, an enormous range of uses has been found for ultracold atoms. From atom counting (as described in the previous section) [8] to clocks [21], interferometry, [22] and quantum simulation [23], cold atoms are used in a quickly expanding number of fields.

Ultracold molecules have proven to be more difficult to produce. Laser cooling techniques rely on repeatedly accessing the same transition, each time exchanging a small amount of momentum. With their more complex rotational and vibrational structure, molecules are quickly optically pumped into dark states where they remain inaccessible to cooling lasers. It is only within the last seven years that direct laser cooling of molecules has been demonstrated, and even then, only within a class of molecules where branching ratios to other vibrational states are highly suppressed [24]. Generally, an unrealistic number of laser systems would be required to laser cool most molecules. Despite these difficulties, a number of techniques have been developed to produce cold or ultracold molecules, including *buffer gas cooling* (400 mK), which relies on thermalization of molecules with cold He atoms, and *photoassociation of ultracold atoms* (< 1 mK), in which cold molecules are formed out of already cold atoms [25]. Ultracold molecules represent an emerging frontier with applications in high precision molecular spectroscopy, quantum chemistry, condensed matter physics, and quantum computing [26].

Of particular interest to this study is photoassociation and its implications on molecular spectroscopy. Photoassociation is the process by which a resonant photon

is absorbed during the collision of two free atoms, resulting in the formation of an excited diatomic molecule. Scanning a spectroscopy laser across these molecules will often yield interesting spectroscopic information about the molecular electronic, vibrational, and rotational states. Signatures of molecular excitation are generally detectable atom loss through radiative decay, or ion production. However, until the advent of laser cooling, photoassociation spectroscopy was of limited use. The spread in collision energies at room temperatures is on the order of 10 THz, which is huge when compared to natural line widths on the order of 10 MHz. Conducting these experiments at ultracold temperatures reduces the thermal spread to less than the natural line width, and allows individual molecular features to be resolved. As such, these experiments are often performed within a MOT, or within a denser trap variant such as a dark MOT or far-off resonance trap (FORT), which provide the cold dense environments that maximize molecular excitation and allow resolution of molecular features. [27]

1.2.1 PREVIOUS WORK IN PHOTOASSOCIATION

Like most work within the field of ultracold physics, research into photoassociation spectroscopy (PAS) began with a focus on the alkali metals. While most of this early work was done in homonuclear systems, by as early as 1995, studies into collisions within heteronuclear systems had begun [28]. K. Jones et al. [29] wrote an excellent review paper that covers the first 17 years of the field. It is worth pointing out that far less work has been done in heteronuclear systems than in homonuclear systems. This is largely due to the fact that heteronuclear work generally requires a more complex dual species apparatus.

With the exception of helium, where interest is driven by BoseEinstein condensateS, fewer still are the number of studies on heteronuclear systems where one atom is in a metastable state. These cases are unique systems in which the atoms' combined internal energies exceed ionization energies, leading to Penning ionization (PI) and associative ionization (AI) to be dominate trap loss mechanisms. Some of the groundwork for these studies was laid by our research group in 2006, when H. Busch studied PI and AI loss rates in an Ar^* + Rb MOT [30]. Other A^* + B collisional and photoassociation (PA) work include a study in He^* + Rb, whose results were in line with H. Busch's [31], and more recently, work involving heteronuclear He^* [32].

Contained within this disseration is a study on PAS of Ar^* + Rb within a dual

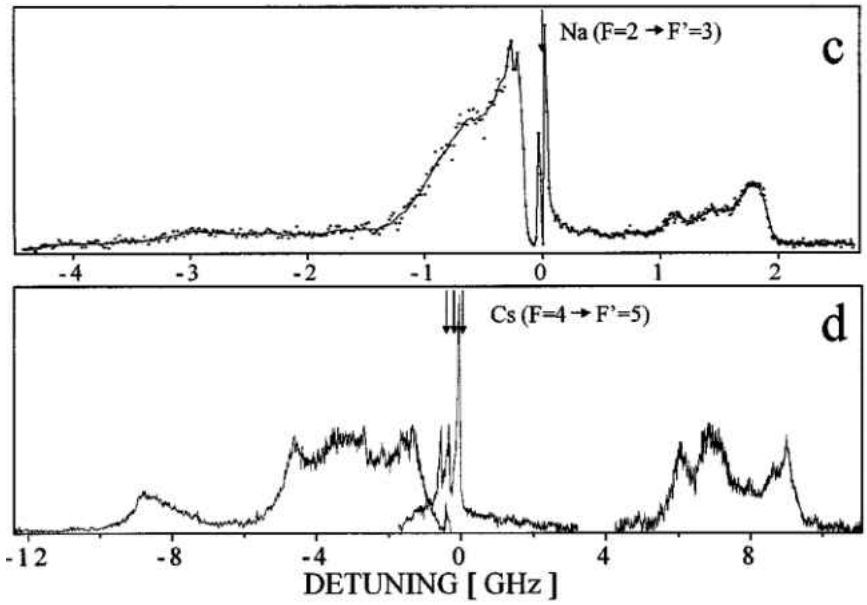

FIG. 2: Photoassociation results from Shaffer et al. Figure credit: Shaffer et al. [1].

species MOT, just below the Ar* $4p[5/2]_3$ + Rb $5^2S_{1/2}$ asymptote. It is similar in scope and design to Ref. [33], in which PAS was performed on a heteronuclear system consisting of Na and Cs. The resulting spectra from that experiment may be seen in Fig. 2. This work picks up where previous graduate students have left off. H. Busch initially built the dual species MOT we use, and characterized trap loss mechanisms [2]; M. Shaffer measured interspecies trap loss rate coefficients for Ar* + Rb and performed PAS on heteronuclear Ar_2^* [1]; and M. Omar improved upon the Ar_2^* spectra of M. Shaffer, and also performed PAS on heteronuclear Kr* [3].

1.3 OVERVIEW OF THIS DISSERTATION

Similar to this chapter, the dissertation as a whole is split into two parts. The next two chapters discuss the work in krypton, while the following three chapters discuss the RbAr photoassociation work. The seventh and final chapter is a conclusion and discussion of possible future work.

Chapter 2 discusses the theory behind all optical production of Kr*. We will describe how we may use the steady state solution to the optical Bloch equations to solve for excitation rates out of a ground state, and how these rates may be used in a system of differential equations to characterize the evolution of a multilevel system

over time.

Chapter 3 discusses the experimental work associated with the Kr^* experiments. We performed three separate experiments with three separate light sources. The chapter starts by describing the atomic beam and laser techniques we used throughout each of these experiments. It then continues on to describe each experiment in detail:

1. ArF, 193 nm excitation
2. FEL + External Cavity Diode Laser, 123 nm + 819 nm excitation
3. UV Lamp + Ti:Sapphire, 123 nm + 819 nm excitation.

Chapter 4 marks the start of the photoassociation work. This chapter describes the basics of molecular structure and photoassociation. We discuss why the work cannot be done at room temperatures, and move on to describe the theory behind the laser cooling and trapping of atoms.

Chapter 5 describes the experimental apparatus used in the photoassociation work. Photoassociation is an instrumentation-intensive project and we have substantial demands of our equipment. This chapter includes details of our vacuum systems, lasers, and detection methods, as well as techniques we developed to overlap a dual species MOT.

Chapter 6 describes both photoassociation experiments performed. We start by detailing the first of two experiments, where we justify the timing scheme used, present results, and draw conclusions. We then do the same with a second experiment developed to confirm the results of the first.

Chapter 7 closes the dissertation with a recap of our experimental results and conclusions. We introduce future prospects for both the metastable Kr and the photoassociation work, including some research that is already underway.

CHAPTER 2

EXCITATION OF METASTABLE Kr

In this chapter, we describe the two methods we used to model metastable excitation efficiencies. Both of these methods are approximations that supply us with order-of-magnitude estimates. Uncertainties about our light sources' spectral and temporal profiles preclude us from making more accurate estimates. However, they provide a guide that we may use to complete our experimental work.

Let us start by imagining a population of two-state atoms, whose structure consists of a ground state and an excited state. We may apply a resonant laser field to the system, coupling the two states and driving atoms from one state into the other. The populations will coherently oscillate between the ground and excited states, and the frequency that this oscillation occurs at is known as the Rabi frequency, Ω [34].

$$\Omega \equiv \frac{-eE_o}{\hbar}\langle e|r|g\rangle \tag{1}$$

where E_o is the amplitude of the light field, e is the electron charge, r is the electron coordinate, and $\hbar$ is the reduced Planck's constant. The Rabi frequency is governed by the intensity of the laser field and the strength of the atomic transition. If the laser field is detuned from resonance, then the effective Rabi frequency becomes Ω' and the amplitude of the Rabi oscillations is attenuated by $(\Omega/\Omega')^2$, where

$$\Omega' = \sqrt{\delta^2 + \Omega^2} \tag{2}$$

where δ is the detuning. However, these oscillations do not provide a complete picture. Excited atoms may spontaneously decay back to the ground state, emitting a photon in the process. This is known as spontaneous decay, and occurs at the radiative decay rate:

$$\Gamma = \frac{1}{\tau} \tag{3}$$

where Γ is inversely proportional to the lifetime of the state, τ. Spontaneous decay introduces decoherence to the system as a whole, and unless $\Gamma \ll \Omega$ these Rabi oscillations will function analogous to a dampened oscillator. The excitation of a

two-level atom by resonant or near-resonant radiation is described by the optical Bloch equations. They show that populations will tend to equalize over time frames where $t \gg \tau$ while the system is being driven. The steady state solution to the optical Bloch equations shows that the exited state population, N_e comes to equilibrium at [35]:

$$N_e = \frac{\Omega^2/4}{\delta^2 + \Omega^2/2 + \Gamma^2/4} \tag{4}$$

The scattering rate is equal to $R_{scat} = \Gamma N_e$, yielding the following expression:

$$R_{scat} = \frac{\Gamma}{2} \frac{\Omega^2/2}{\delta^2 + \Omega^2/2 + \Gamma^2/4} \tag{5}$$

We may model the evolution of the two-state system by using this scattering rate within the following system of differential equations:

$$\frac{dN_g}{dt} = R(-N_g(t) + N_e(t)) + N_e(t)\Gamma \tag{6}$$

$$\frac{dN_e}{dt} = R(N_g(t) - N_e(t)) - N_e(t)\Gamma \tag{7}$$

where $N_g(t)$ is the population in the ground state at time t, and $N_e(t)$ is the population in the excited state at time t. This approach remains valid as long as the rate of spontaneous decay is not negligible when compared to the Rabi frequency, and the atoms are exposed to the laser field long enough for the system to come to equilibrium. This method may easily be scaled up to include more states and more laser fields, as we will show in the next section.

2.1 123 nm + 819 nm EXCITATION SCHEME

Let us now replace the two-state system with a four-state system such as the one shown in Fig. 3. This new system consists of a ground state, two excited states, and a metastable state that cannot be accessed via electronic transition directly from the ground state. We may apply a resonant laser field to couple the ground state to the first excited state, and a second resonant laser field to couple the first excited state to the second excited state. From there, atoms may spontaneously decay down into the metastable state where they remain. The differential equations that describe this process are given in Eqns. 8 through 11.

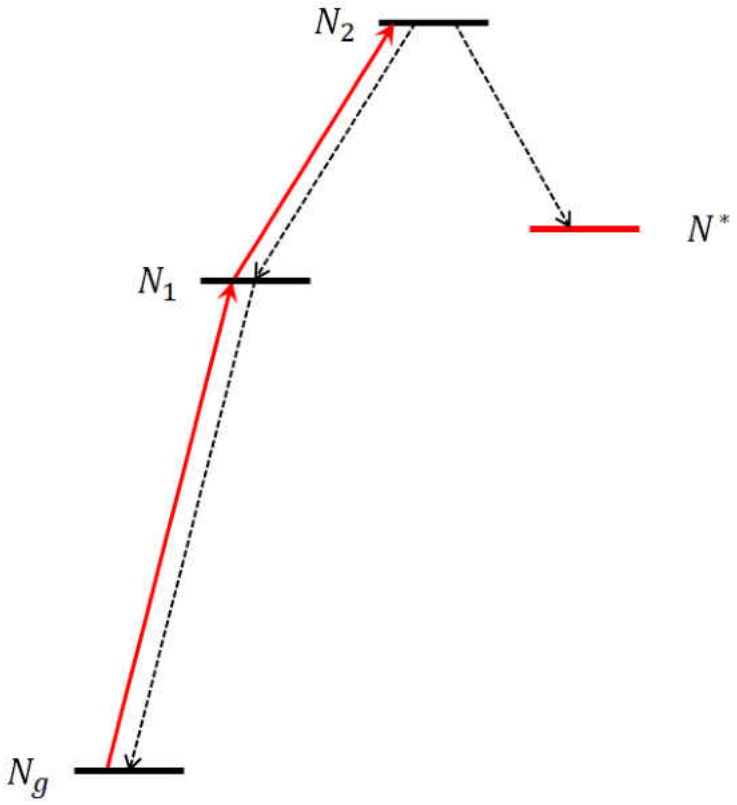

FIG. 3: A generic four-state system, consisting of a ground state, two excited states, and a metastable state as described above. The solid lines indicate excitations from absorbing photons, and the dotted lines represent decays through emission of photons. N^* denotes the metastable state.

$$\frac{dN_g}{dt} = R_1(-N_g + N_1) + N_1\Gamma_{1g} \tag{8}$$

$$\frac{dN_1}{dt} = R_1(N_g - N_1) + R_2(-N_1 + N_2) - N_1\Gamma_{1g} + N_2\Gamma_{21} \tag{9}$$

$$\frac{dN_2}{dt} = R_2(N_1 - N_2) - (\Gamma_{21} + \Gamma_{2*})N_2 \tag{10}$$

$$\frac{dN^*}{dt} = \Gamma_{2*}N_* \tag{11}$$

We may use Eqn. 5 to calculate the excitation rates. In laboratory situations we cannot easily measure the Rabi frequency, Ω. However, we routinely measure laser power and beam size, and therefore may infer intensity. We find it more convenient to take advantage of the relationship between Rabi frequency and intensity:

$$\frac{I}{I_{sat}} = \frac{2\Omega^2}{\Gamma^2} \tag{12}$$

In addition, we may define saturation parameter, s, to be:

$$s = \frac{I}{I_{sat}} \tag{13}$$

where:

$$I_{sat} = \frac{\pi}{3}\frac{hc\Gamma}{\lambda^3} \tag{14}$$

Equations 5, 12 and 13 may be used to yield a very convenient description of excitation rate:

$$R = \frac{\Gamma}{2}\frac{s}{1 + s + (2\delta/\Gamma)^2} \tag{15}$$

We may apply this generic four-state system to a krypton atom. Here, the ground state is $^1S_0$, the first excited state is $5s[3/2]_1$, the second excited state is $5p[3/2]_2$, and the metastable state is $5s[3/2]_2$. Table 1 has the lifetimes necessary to complete these calculations. The excitation out of the ground state requires a very energetic 123 nm photon to drive the first transition. The second transition may be driven with a more manageable 819 nm photon. Finally, atoms may decay into the J=2 metastable state with a branching ratio of 75%. We conducted two experiments using the above excitation scheme. In the first scheme, 123 nm photons were supplied by

Transition	λ (nm)	E(cm^{-1})	$\Gamma(\frac{1}{s})$	$\tau(s)$
N_g to N_1	123.5	80,916.77	$2.98{\cdot}10^{8}$	$3.2{\cdot}10^{-9}$
N_1 to N_2	819.0	12,206.57	$1.1{\cdot}10^{7}$	$9.1{\cdot}10^{-8}$
N_2 to N_{meta}	760.2	13,151.60	$3.1{\cdot}10^{7}$	$3.2{\cdot}10^{-8}$

TABLE 1: Table contains all the constants required to calculate the excitation and decay rates for the 123 nm and 819 nm excitation path.

a pulsed free-electron laser (FEL), and in the second scheme, they were supplied by a continuous wave (CW) UV lamp. Generally one cannot use Eqn. 5 to model the excitation within a system over very short time frames, such as the length of a FEL pulse. However, the FEL was so spectrally broad that most of the light was not near-resonance. The situation become analogous to a dampened harmonic oscillator being driven by many different frequencies simultaneously. In *The Quantum Theory of Light*, R. Loudon states that under such circumstances, the above method becomes a valid approximation [36]. In the case of the UV lamp, the time of exposure is long enough to not be a concern.

2.2 193 nm TWO-PHOTON EXCITATION SCHEME

We may also use a multiphoton excitation to directly excite to a state above the metastable state, as seen in Fig. 4. Again, we may model the evolution of the system with a set of rate equations. However, whereas previously we used Eqn. 5 to find the excitation rate out of the ground state, we now must use the 2-photon excitation rate [37]:

$$W_{ge} = \sigma_o^{(2)} g(\omega) G (I/\hbar\omega)^2 \tag{16}$$

where $\sigma_o^{(2)}$ is the two-photon absorption cross section, $g(\omega)$ is the line shape overlap, G is the two-photon statistical correlation factor and is assumed to be equal to 2 [38], I is the laser field intensity, and ω is the laser angular frequency. Two-photon cross sections tend to be very small, however the excitation rate scales with intensity squared. Usually a two-photon excitation is driven with a high intensity pulsed laser system. In such systems ionization can be a problem, and we must account for that within our system of equations. The ionization rate is given by

$$R_i = \sigma_i (I/\hbar\omega) \tag{17}$$

where σ_i is the ionization cross section. Our overall system of equations becomes:

$$\frac{dN_g}{dt} = -W_{ge} N_g \tag{18}$$

$$\frac{dN_e}{dt} = W_{ge} N_g - \Gamma_{rad} N_e - \Gamma_{e*} N_e \tag{19}$$

$$\frac{dN^*}{dt} = \Gamma_{e*} N_e - R_i N^* \tag{20}$$

$$\frac{dN_i}{dt} = R_i N^* \tag{21}$$

where Γ_{rad} corresponds to the total rate of spontaneous decay out of the excited state to states other than the metastable state. In this approximation we neglect the return of atoms back into ground state, which is negligible because 1) the population excitation out of the ground state is in itself very small, and 2) the atoms are unlikely to have time to repopulate the ground state over the short time scales our pulsed lasers are on. Applied to our Kr atom, we excite directly from the $^1S_0$ ground state to the $6p[3/2]_2$ excited state. From there, atoms may decay into the J=2 metastable state with a 77% branching ratio. Both the two-photon absorption cross section, $\sigma_o^{(2)}$, and the ionization cross section, σ_i have been experimentally measured [39]. The systems shows us that metastable production rate scales with I squared, while the ionization rate scales with I. This suggest that even though we ionize out of the metastable state, it is generally more productive to run at higher powers.

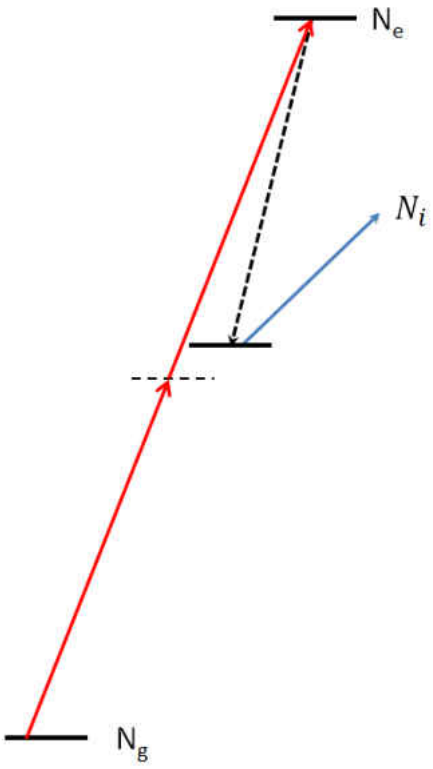

FIG. 4: A generic three-state system, showing 2-photon excitation out of the ground state, through a virtual state, to an excited state above the metastable state. The dashed arrow represents the subsequent spontaneous decay into the metastable state.

CHAPTER 3

METASTABLE Kr EXPERIMENTS

The first half of this dissertation investigates three separate metastable excitation schemes. The first option is an ArF excimer laser located at NASA Langley Research Center in Hampton, VA, which produces high intensity 193 nm pulses. The second option is the free-electron laser located at the Thomas Jefferson National Accelerator Facility in Newport News, VA, which has a third harmonic in the 10 eV range we require. The final option is an RF discharge lamp that is now commercially available, and has the potential to be a reliable alternative to the short-lived home-built lamps previously used. While each light source has its own unique experimental demands, all three experiments required the following: (1) a low pressure environment where background gas will not absorb UV photons or collisionally quench metastable atoms, (2) a system of lasers or a lamp to excite the atoms into a metastable state, and finally, (3) a method of detection for the metastable krypton atoms.

The first section in this chapter discusses our vacuum system, and why we chose to use an atomic beam. Next, we move on and discuss common laser techniques that are present through all three excitation schemes (as well as in the photoassociation work discussed in the second half of this work). Finally, we discuss the individual experiments, including efficiency calculations and detection methods, and results.

1. Vacuum System and Atomic Beam
2. Laser Techniques used in all three experiments
3. Kr Experiment 1 - ArF Excimer Laser Excitation
4. Kr Experiment 2 - Free Electron Laser Excitation
5. Kr Experiment 3 - UV Lamp Excitation
6. Conclusion of the study of metastable Kr excitation

3.1 VACUUM SYSTEMS USED IN Kr EXPERIMENTS

This research was based on work done by Z.-T. Lu and L. Young, where a home-made Kr discharge lamp was built to excite metastable Kr within an atomic beam [17]. Our main motivation for this work was to improve the Atom Trap Trace Analysis (ATTA) apparatus at Argonne National Laboratory, which is also an atomic beam. It seemed natural to conduct our work in an atomic beam as well. Beam experiments offer a number of advantages over cell experiments. Within a cell, our detection methods are limited and we are forced to rely on the decay photon released when an atom decays into a metastable state. Beam experiments allow the Kr^* to move out of the excitation region and away from the excitation lights that can swamp more subtle detection techniques. Here, the asterisk in Kr^* denotes that the atom is in a metastable state. Both fluorescence detection and channel electron multiplier (CEM) collision detection become available in a beam, and we may still search for the decay photon if we desire. In addition, once completed in an atomic beam, this work would be readily transferable to ATTA.

At its basic level, our atomic beam apparatus consisted of two regions that atoms propagate through. First, upon entering the vacuum system, Kr atoms would pass through an excitation region where Kr^* is produced. They then pass into a second region referred to as the detection region, where Kr^* atoms may be counted. See Fig. 5. In all of our experiments, the atomic beam was produced by sending Kr gas from a reservoir and through collimating capillary plates. The flow rate was controlled with a leak valve.

Our beam apparatus was modified to fit the differing needs of each of the three light sources we explored, and these modifications will be described in detail in their corresponding sections. However, in all cases, the vacuum system had the following similarities. An Edwards xDS scroll pump was used to pump down to pressures on order of 10^{-3} Torr, and turbo pumps were used to reach down to the upper end of the 10^{-9} Torr range. When the atomic beam was operating, the background pressures were 1,000 to 10,000 times higher. During all three experiments, an SRS residual gas analyzer was used to monitor the vacuum system. An aluminum cart was built to hold the vacuum chamber, and to more easily transport it off site. The cart had wheels, brakes, and a system to change the elevation of the vacuum chamber so that it could be integrated with other light sources.

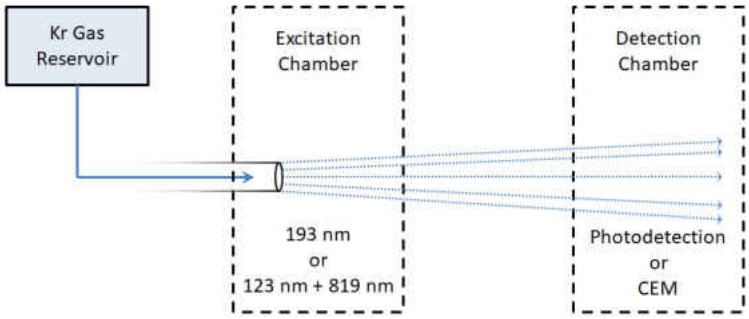

FIG. 5: A basic schematic of the experiment. Atoms are excited within the excitation chamber and move to the detection chamber. The methods used vary from experiment to experiment.

3.1.1 CALIBRATION OF ATOMIC BEAM FLUX

To extract an absolute measure of excitation efficiency, it is critical to have a well-calibrated atomic beam. This means knowing both the total number of atoms in the beam and the spatial distribution of the atoms. In this subsection, we discuss the calculation of atom number.

An atom in the collimated atomic beam will propagate through the vacuum chamber until it either collides with a background atom or collides with the chamber wall. It then random walks around the chamber until it works its way into a turbo pump and is pumped out. The atoms have a most probable velocity of 233 m/s, and the number of atoms being pumped out of the chamber quickly comes into equilibrium with the number entering the chamber when the atomic beam is operating. Over the time frames that we care about, background pressure is proportional to atomic beam flux. A residual gas analyzer (RGA) provides real-time information on background pressure, so by characterizing the relationship between atomic flux and background pressure, we may continuously monitor the beam.

In some of our later experiments we used a type of CEM commonly known as a Channeltron. The RGA relies on a filament to ionize gases, and electrons from the filament may flood the aforementioned Channeltron. This buries real signals and is potentially damaging to the Channeltron. To avoid this, when using the Channeltron we took RGA measurements directly before and directly after the data run. We found that over the course of a run the background pressure changed very little. While obviously preferable to have a continuous string of time-stamped measurements, the

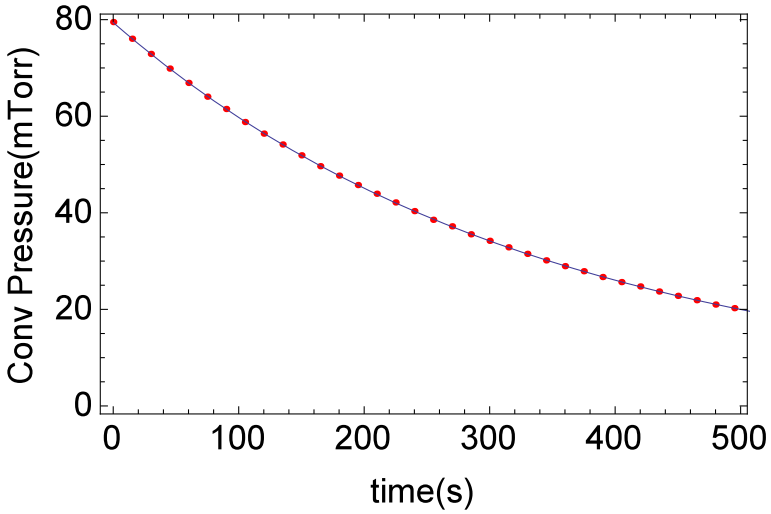

FIG. 6: A graph showing the pressure in the reservoir, as measured by the convectron.

change in pressure over time took the form of an exponential decay, allowing us to model what happened during a data run. This, combined with the small amplitude of the pressure changes, meant that we still had a strong understanding of the atomic beam flux in the moments when the RGA was turned off.

The experimental apparatus may be thought of as a Kr reservoir attached to the main vacuum chamber. For every atom leaving the reservoir, there is an atom entering the main chamber. Because we are working with a relatively low pressure noble gas, we may use the ideal gas law to determine the atom number within the reservoir. Over the course of a data run, the reservoir pressure and atom number decrease proportionally, while the reservoir volume remains constant. The temperature change is negligibly small as the reservoir is in thermal contact with the room around it. By taking regular readings from a convectron pressure gauge attached to the reservoir, we may determine pressure as a function of time, $P(t)$. See Fig. 6. The time derivative of this function gives us an expression for atom number leaving the reservoir as a function of time, $\Phi_{atom}(t)$

$$\Phi_{atom}(t) = -\frac{dN(t)}{dt} = -\frac{dP(t)}{dt}\frac{V}{kT} \tag{22}$$

where N is the number of atoms within the reservoir, and T is the room temperature.

Dividing $\Phi_{atom}(t)$ by $P_{RGA}(t)$, we obtain the ratio of atoms entering the chamber to RGA background pressure. When the calibration is done well, we find that dividing

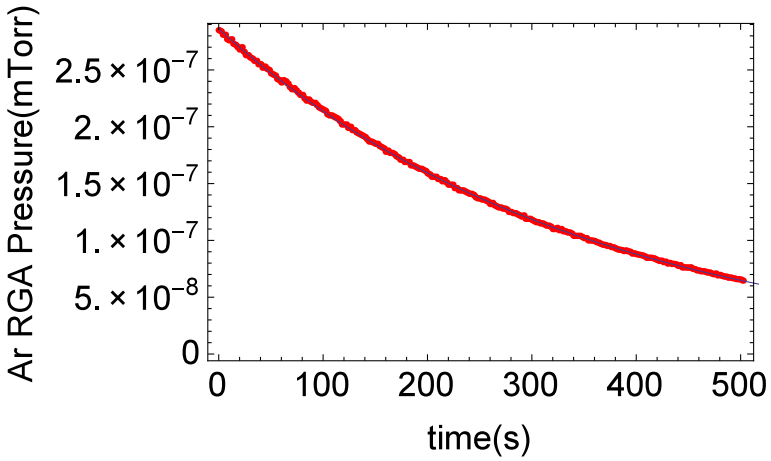

FIG. 7: A graph showing the pressure within the main chamber, as measured by the RGA. Note the curve has the same shape as the one seen in Fig. 6. Both of these graphs are representative of typical curves.

these two functions yields a flat line. We refer to its value as the "calibration factor." At any time, atomic flux may be determined by multiplying the RGA background pressure by the calibration factor.

We further improve the accuracy of the calibration factor by taking two steps. First, the convectron gauge measures different gasses differently. A true pressure of 10^{-2} Torr N_2 will be measured as 10^{-2} Torr, but a true pressure of 10^{-2} Torr Kr will be measured as $5{\cdot}10^{-3}$ Torr. While it is tempting to imagine the reservoir as 100 percent Kr, in reality a small percentage of the gas in the reservoir is a mixture of air. The actual time-of-run mix is readily available from RGA data. Accuracy of Eqn. 22 and our calibration factor can be improved by appropriately weighting the various partial pressures. Second, for unknown reasons the value of the calibration factor changes from day-to-day, as shown in Fig. 8. After investigating, we were able to rule out the following: room temperature, atmospheric pressure, equipment warm-up time, pump settings, contaminants, and improving vacuum over time in the main chamber. Thankfully, calibration factors would generally remain in agreement over the course of a single day. To work around this drift problem, we would perform several calibrations immediately before any data runs. After verification that the results were in a tight cluster, we would conduct the data run. Immediately after the experiment, we would again perform one last calibration run to ensure that our calibration factor had not drifted over the course of the data run.

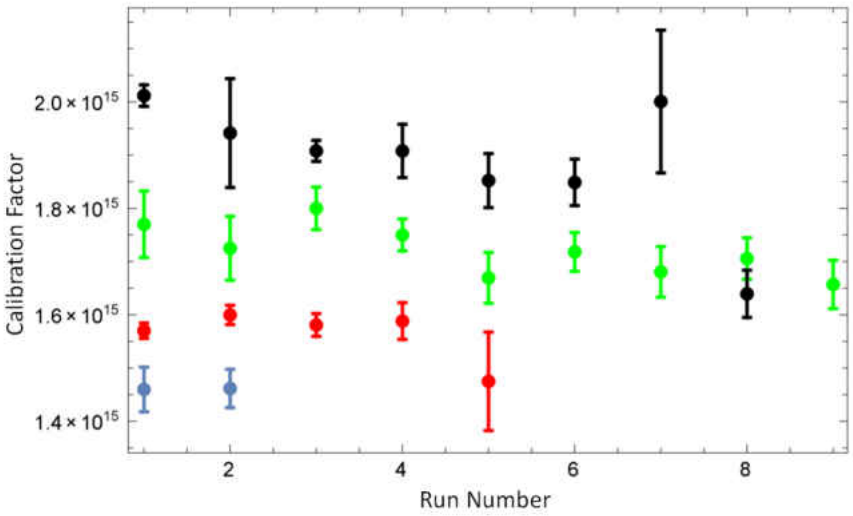

FIG. 8: We see that from day-to-day, the calibration factor can drift. This graph shows the results of 24 calibration runs taken over four different days. We see good agreement within any given day, but poor day-to-day agreement. The units are atoms/(s×Torr).

3.1.2 CALIBRATION OF ATOMIC BEAM RADIAL DISTRIBUTION

As atoms enter the excitation chamber, a capillary plate forms them into an atomic beam. The plate consists of hundreds of narrow tubes, each 200 times longer than their radius. When viewed through a microscope, our plate looks somewhat like a honeycomb with round chambers instead of the usual hexagonal. In this section, we will first discuss the angular distribution of atoms emerging from a single one of these tubes. We may then scale up and describe how the plate as a whole shapes the beam.

These calculations are greatly simplified by the fact that Kr is a noble gas, so we may neglect atom-atom interactions, as well as reactions with the tube wall. Furthermore, we operate in a low pressure regime where an atom may be reasonably expected to pass through the entire tube without colliding with another atom.

Let us consider a narrow tube of length, L, and radius, R. On one side of the tube is a gas reservoir whose atoms have a distribution of trajectories well described by a Maxwell-Boltzmann distribution. On the other side of the tube is a vacuum. As the atoms bounce around the reservoir, some will find their way into the tube entrance. Atoms emerging on the other side will fall into one of two categories: 1)

atoms that enter the tube with a correct trajectory to pass through without colliding with a wall, and 2) atoms that enter the tube with a trajectory that causes them to collide with the wall before exiting the tube. We introduce the following term, p:

$$p = \frac{L}{2R} tan(\theta) \tag{23}$$

which is only dependent on the tube geometry. When $p \leq 1$, the angular distribution is dominated by atoms that have not collided with the tube interior. When $p > 1$, the angular distribution is dominated by those atoms that have previously collided with the tube wall. Upon colliding with the wall, the atom undergoes a diffuse reflection governed by the cosine emission law as developed by Knudsen and Clausing [40],

$$dn = N_o \pi cos(\theta) d\omega \tag{24}$$

where N_o is the total atomic flux reflecting off a specific point on the wall, and dn is the portion of the flux through solid angle dω.

Upon reflection, there is a chance that the atom will now have the correct trajectory to leave the tube unimpeded. However, if it does not, its next reflection off the wall will again be governed by the cosine emission law. As the atom will have moved since the first collision, there is now a new set of trajectories that will allow it to escape the tube. The atom will continue to move in this manner until it has either reflected back into the reservoir, or has successfully traversed the length of the tube. These calculations are typically performed using Monte Carlo simulations. The topic is covered in depth in Ref. [41], and we now present the key points regarding very long cylindrical tubes. Upon leaving the tube, the angular distribution of the atomic beam, $M(\theta)$, is given by

$$M(\theta) = T cos(\theta) \tag{25}$$

where T, the transmission function is given by

$$T = \begin{cases} 1 - \frac{2N_o}{\pi}(sin^{-1}(p) + p\sqrt{1-p^2}) + \frac{4}{3\pi p}(2N_o - 1)(1 - (1-p)^{3/2}), & 0 \leq p \leq 1, \\ 1 - N_o + \frac{4}{3\pi p}(2N_o - 1), & p > 1. \end{cases}$$

In the above expression, N_o is defined by the following:

$$N_o = 1 - \frac{4R}{3L} \tag{26}$$

The radial distribution at a set distance, z, is of more practical use to us than the angular distribution. We may rewrite the $cos(\theta)$ found in Eqn. 25 in terms of r and z.

$$M(r,z) = T(1/\sqrt{1+\frac{r^2}{z^2}}) \tag{27}$$

However, Eqn. 27 is only the distribution from a single tube. Our capillary plate is made up of many. The final distribution at some point (x_i, y_j, z) further downstream is made up of the superposition of the radial distribution from each hole. Giving each hole a Cartesian coordinate, (x_m, y_n), and setting $r = \sqrt{x^2+y^2}$, we find:

$$M_{cap}(x_i, y_j, z) = \sum_{\text{Cap Plate Holes}} M(\sqrt{(x_i - x_m)^2 + (y_j - y_n)^2}, z) \tag{28}$$

We wrote a Mathematica script to give the radial distribution as a function of z and r. The script is designed to be used with a variety of tube lengths, and calculated p before determining which version of the transmission function to use. The spatial distribution of the beam at z = 1 mm, z = 10 mm, z = 100 mm, and z = 500 mm may be seen in Fig. 9.

3.2 COMMON LASER TECHNIQUES

Exciting atomic transitions in an efficient manner requires us to use narrowband lasers locked onto an atomic resonance. Generally speaking, we want our lasers to be significantly narrower than the natural linewidth of whatever transition we wish to interact with. This ensures that all of the laser output is used to drive the transition. These requirements will remain true throughout the entire body of this work, and as such, this section will describe the techniques that we find ourselves repeatedly using to lock our lasers.

3.2.1 EXTERNAL CAVITY DIODE LASERS

Semiconductor lasers permeate modern society. They are found in CD and DVD players, laser pointers, barcode readers, communication devices, and children's toys. Their popularity stems from a multitude of factors, including their cost, which can start as low as a fraction of a penny; their size, which is often on par with a small button; their high efficiency at converting electrical energy to coherent light; and

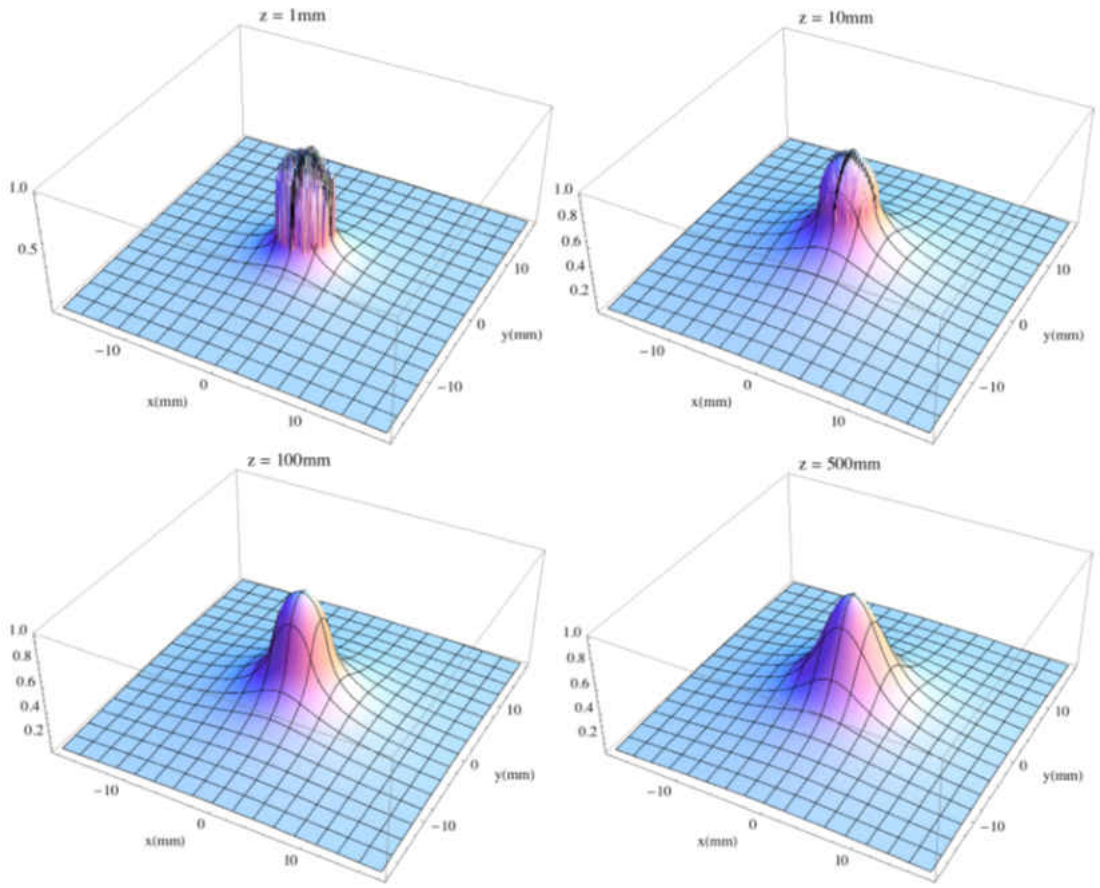

FIG. 9: Four plots showing the atomic beam profile at 1 mm, 10 mm, 100 mm, and 500 mm from the capillary plate. Initially we may resolve many smaller individual beams from the capillary plate tubes. As the discrete beams propagates further into the chamber, they merge together.

their ruggedness. For all these same reasons we find that semiconductor lasers are very common in modern atomic physics laboratories. To form a semiconductor laser, a p-n junction is built by applying the appropriate doping while growing a crystal. Light is emitted when electrons transfer across a p-n junction. Facets at either end of the crystal form an optical cavity, causing feedback from photons reflecting off the index of refraction change at the end of the crystal, and allowing stimulated emission to occur [42]. This process results in a diode laser whose center wavelength is tunable with both temperature and current. Generally, semiconductor lasers used in our laboratory only have powers in the range of 1 mW to 150 mW. However arrays of many diode lasers can be assembled to reach much higher powers. (This is how we pump our Ti:Sapphire laser.) We can tune over a much larger range by building an external cavity. In our laboratory, our external cavity diode lasers (ECDLs) have tuning ranges on the order of tens of nm, and mode-hop-free tuning ranges of around 1 GHz to 10 GHz. We use two main configurations of ECDL, Littrow and Littman-Metcalf.

In a Littrow configuration, shown in Fig. 10, the laser diode is housed in a temperature stabilized compartment. Its output is collimated into a beam with a lens and sent onto a diffraction grating. The relationship between the angle of incidence and the diffracted beam off the grating is governed by

$$n\lambda = d(sin\theta + sin\theta') \tag{29}$$

where d is the grating constant, θ is the angle of incidence, and θ' is the angle of diffraction of the n^{th} order. We see there are solutions where $\theta = \theta'$, and the resulting -1^{st} order is diffracted back into the laser diode. Here, the feedback from the -1^{st} order drives the laser cavity and selects the dominant wavelength in the diode. We may tune the Littrow-configured ECDL by adjusting the angle of the diffraction grating. In our lasers, this is done by mounting the diffraction grating onto a mirror mount, and inserting a piezoelectric transducer (PZT) into the x-axis adjustment mechanism. However, this does have the unwanted effect of shifting the angle of the 0^{th} order. It is the 0^{th} order that continues on as the output of the laser.

A Littman-Metcalf configuration, shown in Fig. 11, is similar to a Littrow configuration in that it also relies on a diffraction grating for wavelength-selective feedback. Again, the diode is housed in a temperature stabilized compartment, its output is collimated with a lens, and sent onto a diffraction grating. However, the -1^{st} order

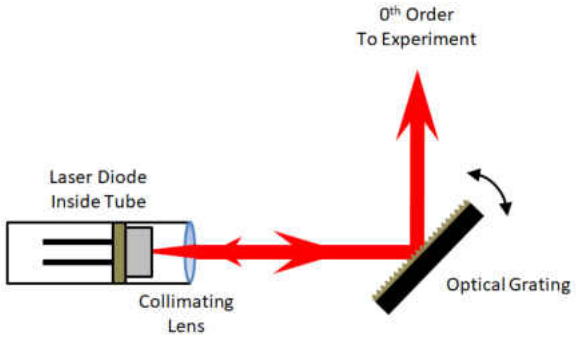

FIG. 10: A diagram of a Littrow ECDL. The cavity is formed between the laser diode and the optical grating, from where the negative first order is reflected back into the cavity. The feedback my be selectively tuned by adjusting the angle of the grating.

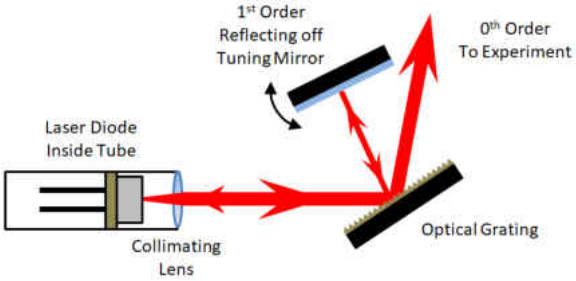

FIG. 11: A diagram of a Littman-Metcalf ECDL. The cavity is formed between the laser diode and the tuning mirror, from where the positive first order is reflected back into itself and into the laser diode. The feedback my be selectively tuned by adjusting the angle of the mirror.

is not reflected back into the diode. Instead, the $+1^{st}$ order diffracts onto a mirror, and from the mirror back into the grating and into the laser diode. To tune the laser, the angle of the mirror is adjusted. This has the advantage of allowing us to adjust the selected wavelength without shifting the angle of the 0^{th} order output. The double pass on the grating results in feedback that is low in power, but narrower than the Littrow configuration. In our experience, we have found that some of our diode lasers have pulled more easily in a Littman-Metcalf cavity, and others have pulled more easily in a Littrow cavity.

3.2.2 SATURATED ABSORPTION SPECTROSCOPY

In every experiment discussed in this work, it is critical to lock our lasers to the specific frequencies that correspond to the transitions we wish to excite. We send a portion of each laser's output through an atomic vapor cell to serve as an absolute reference. As we tune the laser frequency and it starts to approach a resonance, photons will begin to scatter out of the beam. We may detect scattering either through looking for the fluorescent photons, or by measuring the power of the laser beam after it propagates through an atomic vapor. In these resonant interactions, the scattering rate, R, is given by

$$R = \frac{\Gamma}{2}\frac{s}{1+s+(2\delta/\Gamma)^2} \tag{30}$$

where s is the saturation parameter defined in Eqn. 13 , and δ is the laser detuning. However, Eqn. 30 assumes that both atom and photon source are in the same frame of reference. In reality, atoms at room temperature have velocities ranging from a few hundred meters per second (in the case of krypton) to over a km per second (in the case of hydrogen). The distribution of velocities in a vapor is well described by a Maxwell-Boltzmann distribution. In a room temperature vapor cell, a natural line width of a few MHz will be Doppler-broadened on the order of a GHz. Our Lorentzian natural line width will approach the Doppler-broadened Gaussian line width, g_D, given as

$$g_D = \frac{c}{v_p\omega_o}e^{-(c/v_p)^2((\omega-\omega_o)/\omega_o)^2} \tag{31}$$

where v_p is the most probable speed, and $\omega - \omega_o$ is the detuning from resonance.

We need to lock our lasers to narrow atomic transitions, but at room temperature, these transitions are so Doppler-broadened that they cannot serve as an absolute frequency reference. This is illustrated in Fig. 12. However, we may resolve the unbroadened natural line widths by using a form of sub-Doppler spectroscopy called Saturated Absorption Spectroscopy (SAS).

Consider an atom with an arbitrary velocity, $\vec{v}$, and a scanning laser with frequency $\omega(t) = \omega_o + \delta(t)$, where ω_o is a resonant frequency and $\delta(t)$ is the laser detuning at time t. The laser is split into a strong beam referred to as the pump, and a weak beam referred to as the probe. As they are from the same source laser,

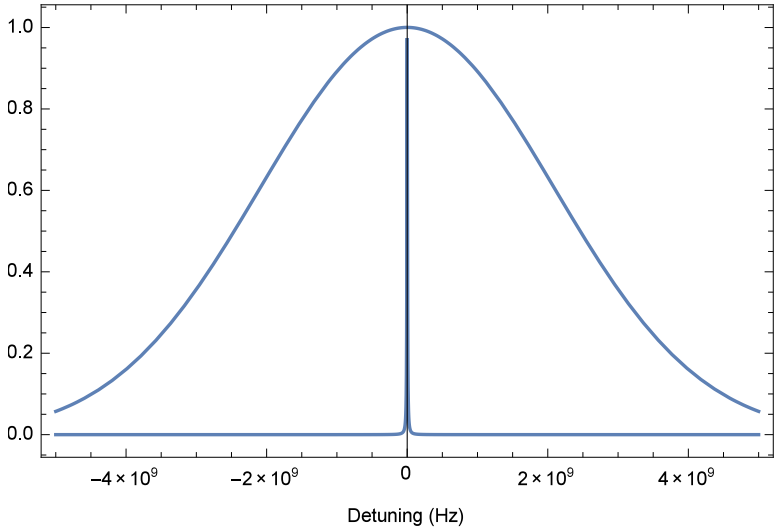

FIG. 12: A plot showing both the Lorentzian-shaped natural line width, and the Doppler-broadened line width of the Rb $5^2S_{1/2}$ to $5^2P_{3/2}$ transition. For ease of view, both functions have been normalized to their maximum scattering rate. The FWHM of the broadened distribution approaches 1 GHz, while from this far out, the Lorentzian natural line width almost appears to be a delta function. This demonstrates the problem with using room temperature vapor to lock to a specific transition.

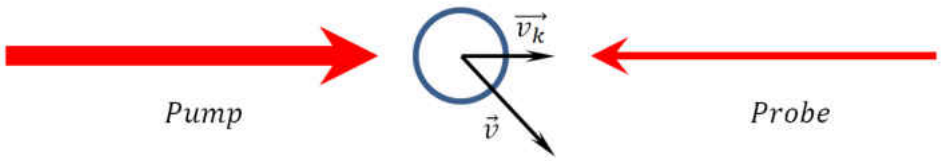

FIG. 13: A picture of an atom with an arbitrary velocity, $\vec{v}$, with two counterpropagating laser beams, the pump and the probe. The velocity has a component $\vec{v_k}$ in the same direction of the $\vec{k_{Pump}}$.

at any time both will have the same frequency, $\omega(t)$. The beams are overlapped counterpropagating with the considered atom in between as in Fig. 13.

The atom will see different Doppler shifts in the frequencies of the pump and probe lasers. In Fig. 13, the atom has a velocity to the right towards the pump beam. In this case, the atom will see the following frequencies for the pump and the probe, denoted as ω_P and ω_{pr}, which are given by

$$\omega_P = \omega_o + \delta(t) - \vec{v} \cdot \vec{k}_P \tag{32}$$

$$\omega_{pr} = \omega_o + \delta(t) - \vec{v} \cdot \vec{k}_{pr} \tag{33}$$

where $\vec{k}_P$ is the wavevector of the pump beam and $\vec{k}_{pr}$ is the wavevector of the probe beam.

Returning to our vapor cell whose velocity distribution is described by Eqn. 31, we see that both the pump and the probe will almost always interact with different velocity groups. The exception occurs when the laser source scans over resonance and $\delta(t) = 0$. At that time, atoms with a velocity such that $\vec{v} \cdot \vec{k}_P = \vec{v} \cdot \vec{k}_{pr} = 0$ will see both the pump and the probe beams as resonant.

The pump is significantly more intense than the probe, and has a higher probability to interact with any individual atom. As the probe propagates through the cell, it finds that the pump has depopulated the ground state atoms. While the laser is tuned near resonance, so that both pump and probe are interacting with the same atoms, absorption from the probe beam dramatically decreases and creates a peak centered around ω_o. At low intensities and pressures the saturated absorption peak is a close approximation to the Lorentzian described in Eqn. 30.

3.2.3 PLASMA DISCHARGE

For krypton (and later with argon), we find that we have an added complication when locking our lasers. For an absolute frequency reference, we need atoms in the metastable $5s[3/2]_2$ ($4s[3/2]_2$ for argon) state. However, all of the atoms in our room temperature Kr vapor cell are in the ground state. By inducing a plasma inside the cell, we may collisionally excite to the metastable state. We have found that we achieve a Kr^* efficiency of only 10^{-4}. While low, this is more than enough to serve as a reference for locking lasers.

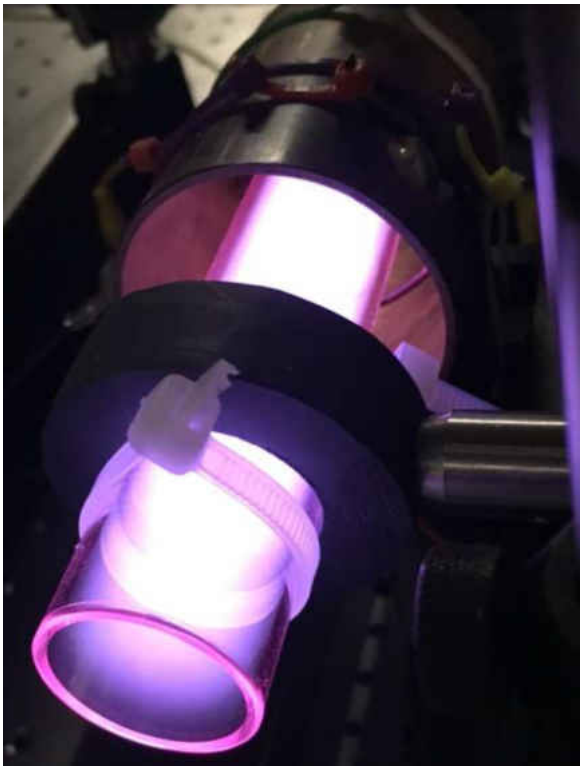

FIG. 14: A photograph of a Kr cell with an RF discharge inside. This specific cell was used to provide a reference to lock to the 819 nm transition.

In practice, we accomplish this by using a voltage-controlled oscillator (VCO) to provide an RF voltage to an amplifier, which is then sent to copper magnet wires that have been coiled into an antenna. For further control, and to protect the amplifier, a variable attenuator is placed after the VCO. The VCO output frequency is tuned with a potentiometer-regulated control voltage. By scanning the tuning frequency, temporarily increasing the power via reduced attenuation, and by sliding the cell back and forth through the coils, we may cause a plasma to ignite. Figure 14 is a picture of a Kr cell with a running discharge.

Most of our krypton cells are produced by Opthos, and are stand-alone glass tubes with vapor pressures in the range 100 mTorr. However, we have seen that some of these cells seem to fail from time to time. The cause has been difficult to pin down, but we suspect that contaminants present during the creation of the cell may be driven out of the glass walls during the discharge. So in addition to these cells we also use a home-built cell with components from Argonne National Laboratory. The home-built cell consists of a glass tube connected to a small cross piece. If it starts to fail, the cell may be attached to a vacuum system, pumped out, and refilled with krypton gas. Getters placed inside the cross piece maintain cleanliness for several months after the initial pump down.

3.2.4 PHASE-SENSITIVE LOCKING

The simplest way to lock a laser to an atomic transition is to use a side lock. In side locking, a photodetector measures the voltage that corresponds to the laser being tuned halfway up the side of the desired saturated absorption peak. If the laser frequency drifts closer to the peak center the voltage will rise, and if it drifts away the voltage will fall. A negative feedback loop works to maintain the voltage by making slight adjustments to the laser frequency. However, this method is vulnerable to the types of fluctuations that occur over time in any laboratory. Variations in signal amplitude will cause the laser to drift in frequency space, and effects of vibrational or thermal noise are not filtered out by the lock.

We may overcome these challenges by using phase-sensitive locking, which is a technique that takes advantage of the orthonormality of sine functions to remove unwanted frequencies. We recall that if $\omega_1 \neq \omega_2$:

$$0 = \int_0^T A \sin(\omega_1 t) B \sin(\omega_2 t + \phi_0) dt \tag{34}$$

and if $\omega_1 = \omega_2$ and $\phi_0 = 0$:

$$\frac{AB}{2T} = \int_0^T A \sin(\omega_1 t) B \sin(\omega_2 t + \phi_0) dt \tag{35}$$

As our laser repeatedly scans over the atomic peak, we may consider its output as a periodic signal at some frequency, ω_s. The total photodiode output is this desired signal superimposed on top of all of the different noise sources, with each source being at its own frequency. If we shift our signal's frequency far away from the noise frequencies, mix it with an external reference oscillation, and integrate for a long time, our output is a DC signal proportional to the size of our input signal.

In practice this is with a reference signal originating from a lock-in amplifier, $\sin(\omega_r + \phi_0)$. The reference modulates the laser current, which in turn modulates the laser frequency. The modulation has negligible effect on the photodiode signal if the laser is tuned more than a few tens of MHz from resonance. However, as the laser frequency starts to move up the side of the Lorentzian peak, a small change in frequency produces an increasingly large change in amplitude. Similarly, as the laser frequency crosses resonance and moves down the other side of the peak, an increase in frequency will cause a decrease in amplitude. The result is a 180 degree phase shift, centered around the top of the SAS peak.

The modulated signal is sent into the lock-in amplifier, and a mixer multiplies it with a copy of the reference, $\sin(\omega_r + \phi_0)$. At this point, the signal we care about is already at frequency ω_r due to the modulation, and we may integrate to remove the noise. While it is physically impossible to integrate from 0 to infinity, the noise frequencies are sufficiently attenuated with an integration time of a few milliseconds. This is done with a low pass filter with a time constant that is several times larger than $1/\omega_r$. The output is a DC signal proportional to the modulated signal amplitude over the integration time. A scan over the entire peak produces a phase-dependent signal like that seen in Fig. 15. While it might look like the derivative of our peak, it is actually a phase-dependent derivative-like signal, and we may flatten it or invert it by adjusting ϕ_0. The steepest portion occurs at a laser detuning of zero, and is ideal to lock our lasers to.

3.3 ArF EXCIMER LASER EXCITATION

The first light source we tested was an ArF excimer laser at NASA Langley Research Center. It produces light at 193 nm, which can excite directly from the ground

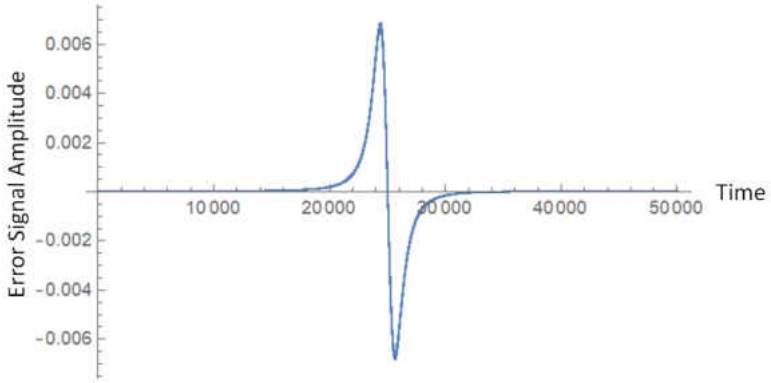

FIG. 15: An example of the error signal output of a lock-in amplifier. The units in this chart are arbitrary.

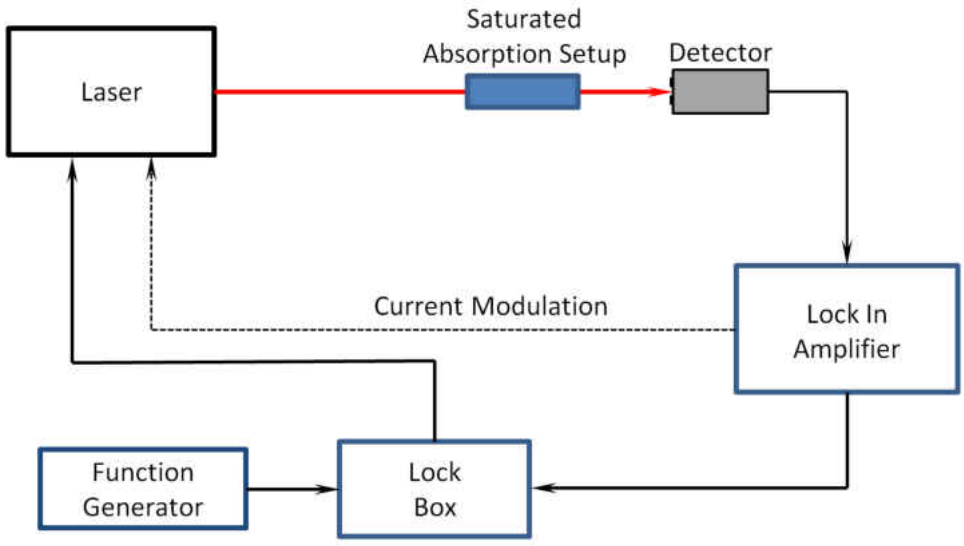

FIG. 16: A diagram of the locking feedback loop. The laser current is modulated with a sine wave from the SR830 lock-in amplifier. This modulation is then passed through to the laser light (shown in red) as a frequency modulation. The laser light is used in an SAS module to find a resonant peak, and the modulated peak is fed back into the lock-in amplifier. The output of the lock-in amplifier is sent to the lock box, where it can be used to control the laser piezo voltage, and keep the laser frequency output steady.

state to $6p^2[3/2]_2$ via a two-photon excitation. Decay into the J = 2 metastable state occurs with a branching ratio of about 77%. Two-photon transitions have very small absorption cross sections, and are generally negligible unless excited by the high intensities found in a pulsed laser beam. The ArF excimer we used provided 100 mJ pulses that were 10 ns long, and had a spectral width of 0.5 cm^{-1}. It had a repetition rate of 10 Hz. If the method proved successful, newer ArF excimer lasers with higher repetition rates could be used with ATTA to excite a larger fraction of the atomic beam. Nonetheless, the laser located at NASA Langley was an excellent fit to test our predictions.

3.3.1 ArF EXCITATION VACUUM MODIFICATIONS

We used the same atomic beam that was described in Section 3.1. Fused silica windows were used to allow the 193 nm photons into the excitation region with little loss. The laser was brought to a focus immediately in front of the capillary plate where the Kr atoms are densest. 193 nm light scatters in air, and the laser beam had to travel through about 50 cm of atmosphere before entering our vacuum. The 100 mJ pulse power was measured at our vacuum system, after the beam had already propagated through 45 cm of the air.

In later parts of the experiment, we wanted to view photons from the excitation region with a detector. A window was mounted directly above the region, but upon observation, we found there was a tremendous amount of scattered light. A fellow graduate student, Jack Mills, welded a light pipe to a gasket (see Fig. 18). It extended directly over the excitation region, and successfully blocked over 99% of the scattered light that had previously been reaching the detector.

3.3.2 ArF EXCITATION EXPECTED EFFICIENCY

In Section 2.2, we described the method used to estimate the per pulse efficiency of this metastable excitation method. Atoms are directly excited to the $6p^2[3/2]_2$ state, from which they may decay into the $5s[3/2]_2$ metastable state. A loss mechanism is added to the system, caused by the energetic 193 nm photons ionizing previously excited metastable Kr atoms. However, as mentioned in Chapter 2, the rate of excitation scales with laser intensity squared, whereas the rate of ionization scales linearly with intensity. Even with ionization, it is to our advantage to have as much light as possible. The above situation is described by the following system of

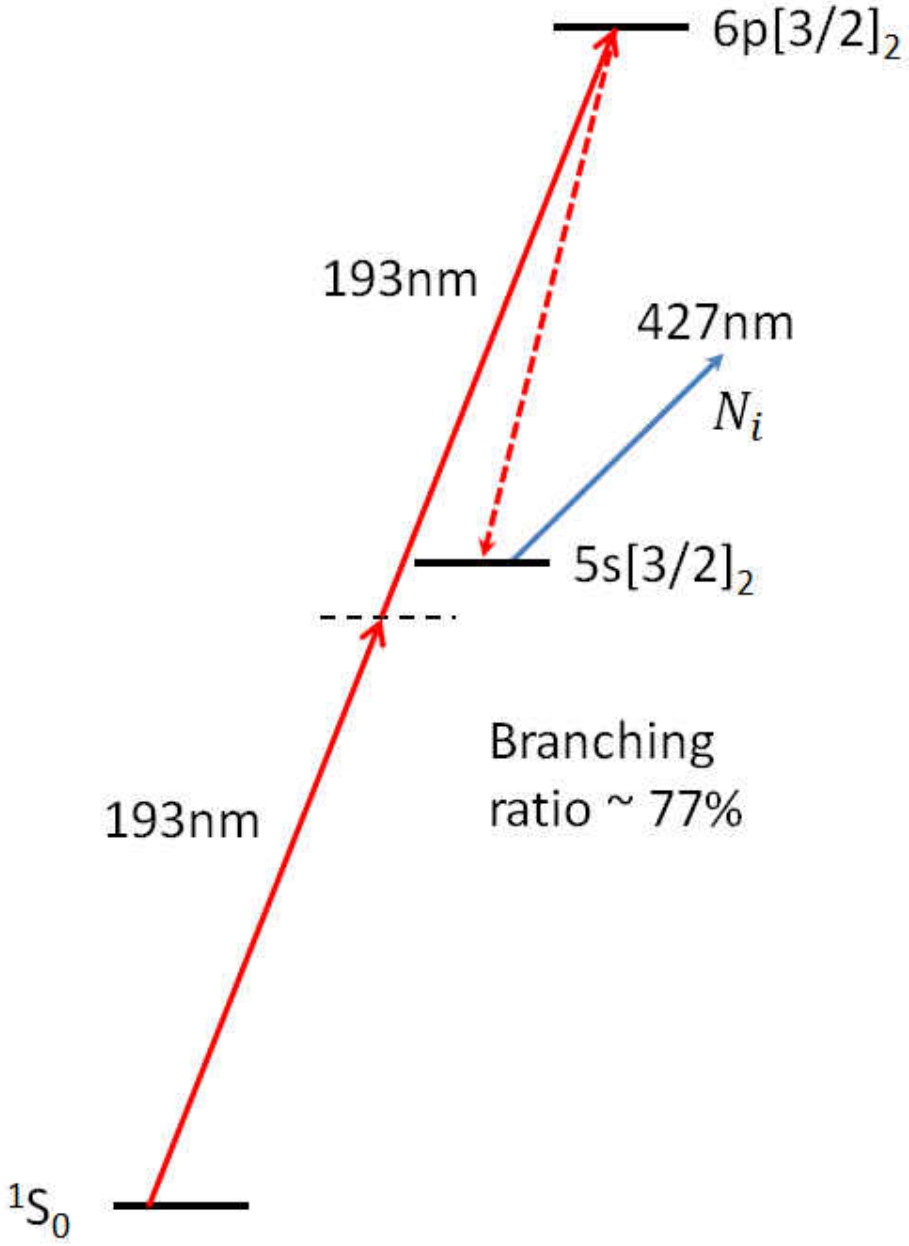

FIG. 17: A diagram of the relevant states associated with 193 nm excimer laser excitation scheme.

FIG. 18: A photograph of a gasket that was specially created to block scattered light.

equations:

$$\frac{dN_g}{dt} = -W_{ge}N_g \tag{36}$$

$$\frac{dN_e}{dt} = W_{ge}N_g - \Gamma_{rad}N_e - \Gamma_{e*}N_e \tag{37}$$

$$\frac{dN^*}{dt} = \Gamma_{e*}N_e - R_iN^* \tag{38}$$

$$\frac{dN_i}{dt} = R_iN^* \tag{39}$$

where W_{ge} is the two-photon excitation rate out of the ground state and into the excited state

$$W_{ge} = \sigma_o^{(2)} g(\omega_L) G (I/\hbar\omega)^2 = 9.4 \times 10^{10} (1/s) \tag{40}$$

Here, $\sigma_o^{(2)}$ is the two-photon absorption cross section, and has been experimentally measured to be $5.4{\times}10^{-37}$ cm^4 [39]. G is the two-photon statistical correlation factor and is assumed to be equal to 2 [38]. $g(\omega_L)$ is a measure of the spectral overlap of the transition and laser pulse and is given by

$$g(\omega_L) = \frac{2\sqrt{ln(2)/\pi}}{((\Delta\omega_\tau)^2 + (3\Delta\omega_L)^2)^{1/2}} = 7 \times 10^{-12} \tag{41}$$

where $\Delta\omega_L$ is the spectral width of the laser, and $\Delta\omega_\tau$ is the spectral width of the atomic transition. The laser intensity, I, in a Gaussian pulsed beam is given by

$$I = \frac{2E_{pulse}/t_{pulse}}{\pi w^2} = 2.5 \times 10^{14} W/m^2 \tag{42}$$

where the pulse energy is 100 mJ, the pulse length is 10 ns, and the laser waist, w, is 0.5 mm. Finally, we calculate R_i, the ionization rate out of the metastable state, which is given by

$$R_i = \sigma_i(I/\hbar\omega) = 4.2 \times 10^{10}(1/s) \tag{43}$$

where the ionization cross section, σ_i, has been measured experimentally to be 4.39×10^{-19} cm^2.

W_{ge} and R_i may be substituted in the rate equations shown in Eqns. 36-39. Jack Mills wrote a MATLAB code to numerically model the evolution of the above system over the length of a 10 ns pulse. His calculations estimate a 1.7×10^{-3} per pulse efficiency. This number should be taken as an order of magnitude calculation.

3.3.3 427 nm DECAY DETECTION

We had initially intended to use the same fluorescence detection as described in Section 3.4.7. We quickly discovered that we would be unable to do so. The excimer laser relies on a flash lamp to initiate the population inversion required for lasing. Light from the flash lamp is extremely broad and has a high intensity spanning the infrared spectrum. A portion of the flash lamp emission continually worked its way into the detector. Attempts were made to install light tubes and beam blocks, but we finally decided that it was too difficult to isolate the detector.

Instead of using a separate detection laser to purposefully scatter photons, we decided to look for the 427 nm decay photon emitted when the excited atoms decay into the metastable state. Unfortunately, this method gives us a hit to our signal size. Whereas previously each Kr* atom scattered around 500 photons, now only one single photon will be emitted per atom. This is only slightly offset by the detector having a higher efficiency detecting more energetic photons, which has increased from 2% to 20%.

While compared to the other transitions we work with, the decay down into the metastable state has a relatively long lifetime of 502 ns; however, it is still so short

that detection and excitation must occur in the same place. A window was installed directly over the excitation region and a collection lens was put in place. With a solid angle of 9.4×10^{-4} sr, light from the metastable production was collected, sent through an interference filter into a Hamamatsu R928 PMT. Even with shielding, the PMT picked up noise every time the Q-switch was triggered, which can be seen in the graph presented in the next section. The Q-switch noise is consistent enough that it did not interfere with data analysis.

3.3.4 EXCIMER LASER RESULTS

Using the methods above, we successfully detected evidence of metastable Kr production. Figure 19 is a graph depicting the output of the PMT as it observes the excitation region. The red line shows a noise from the Q-switch when no Kr was present in the vacuum chamber. The blue line shows the signal size once Kr is flowing. The difference between the two is attributed to 427 nm decay photons.

The PMT is a current source that we terminated into a 1 MΩ resistor. An oscilloscope measures the voltage across the terminating resistor as a function of time. We begin our analysis with Ohm's Law

$$V = IR \tag{44}$$

and note that at any given time, the current through the resistor is equal to the potential across it divided by 1 MΩ. Along with the definition of current, $I = (dQ/dt)$, we may relate the area under the curve of $V(t)$ to the total charge released from the PMT,

$$\frac{1}{R}\int V(t)dt = \int \frac{dQ(t)}{dt}dt = Q_{total} \tag{45}$$

We now turn our attention to the PMT itself. Light is collected by a 1-inch lens with a solid angle of $\Omega = 9.4\times10^{-4}$ sr. A 427 nm photon entering the photocathode has a 20% chance to eject an electron. With our control voltage set to 0.7 V, the single electron will experience a gain, G, around 7.2×10^{-5}. The means the total charge leaving the PMT when N_p 427 nm photons are emitted in the excitation region is given by

$$Q_{total} = N_p \times \frac{\Omega}{4\pi} \times Q.E. \times G \times e \tag{46}$$

We may set Eqns. 45 and 46 equal to each other to solve for the total number of 427 nm photons released:

$$N_p = \frac{4\pi}{R \times \Omega \times Q.E. \times G \times e} \int V(t)dt \tag{47}$$

The area under the curve associated with 427 nm photons is equal to 2.69×10^{-5} Vs. Substituting these values into Eqn. 47, we find each pulse excited an average of 3×10^{8} metastable Kr atoms. The 193 nm light comes to a focus with a 1 mm diameter centered directly where the atomic beam emerges from the capillary plate. Using the methods described in the previous sections, we estimated that there were 7.5×10^{9} atoms in the interaction region. Together, with the calculated number of excited Kr* atoms, we found an efficiency of 4×10^{-4}.

Our experimental efficiency of 4×10^{-4} per pulse comes relatively close to our theoretically predicted efficiency of 1.7×10^{-3}. To improve agreement further, we would need to have a better understanding of the excimer laser's spectral output, which is not a small undertaking. While we were able to achieve our goal of optically exciting metastable Kr, in the end we determined that an ArF exicmer laser was not a realistic solution for ATTA. The excimer laser itself is a large complex machine that requires a steady, expensive supply of fluorine gas. While newer models are both more powerful and have a higher repetition rate, we came to the conclusion that excimer laser metastable excitation would likely lead to a small increase in ATTA's up-time, but only at great expense. However, we were pleased to have demonstrated all-optical production and to have our experimental results come close to our predictions.

3.4 FREE ELECTRON LASER EXCITATION

The second light source we tested was the free-electron laser (FEL) at the Thomas Jefferson National Accelerator Facility (JLab). An FEL is a powerful coherent light source that uses relativistic electrons as a gain medium. After being accelerated to speeds approaching c, the electrons pass through an undulator, which is a spatially dependent magnetic field that causes them to oscillate in a direction perpendicular to their average velocity. These rapid accelerations cause an electron bunch to spontaneously emit resonant synchrotron radiation. Standing waves may be formed by placing mirrors at either end of the undulator and creating an optical cavity. Like any lasing cavity, many harmonics will form and may be separated from the fundamental beam with an optical grating. It is one of the harmonic modes that is of interest to

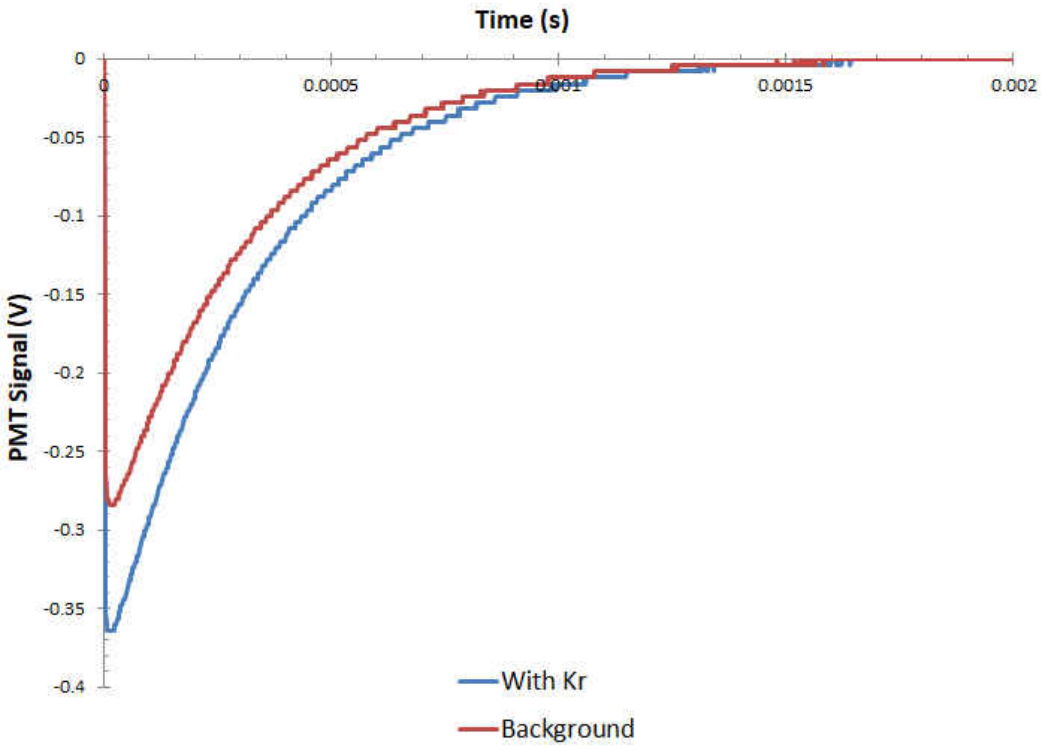

FIG. 19: A plot showing the signal from the PMT observing the excitation region both with and without Kr gas flowing. Most of the background comes from the PMT picking up noise from the laser Q-switch, and thus cannot be filtered out.

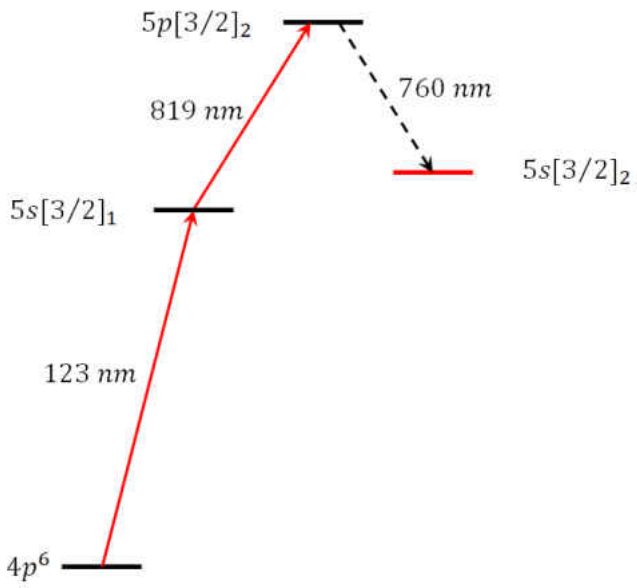

FIG. 20: Krypton 123 nm excitation path from the ground state to the J=2 metastable state.

us.

The JLab FEL had a third harmonic tunable to 123 nm, which matches the energy requirement to excite from the ground state to the $5s[3/2]_1$ state. In this experiment, we investigated using the JLab FEL 3rd harmonic in combination with our own 819 nm diode laser to excite krypton from the ground state to the J=2 metastable state. At the JLab FEL, the accelerator and optical cavity are in the basement, and the laboratories are on the first floor. The 3rd harmonic beam may be reflected up into the laboratories with a periscope. 10 eV photons are absorbed by the atmosphere, so our beam machine was attached directly to the FEL output with a CF flange. Our vacuum and the FEL vacuum were separated by a MgF_2 window, which was chosen because MgF_2 is transparent to UV.

3.4.1 FEL ATOMIC BEAM MODIFICATIONS

We again used the same atomic beam apparatus described in Section 3.1 with a few modifications. 10 eV photons are highly absorbed when passing through the atmosphere, so as mentioned in the previous section, the FEL vacuum chamber was connected to our vacuum chamber with a CF flange as shown in Fig. 21. The two

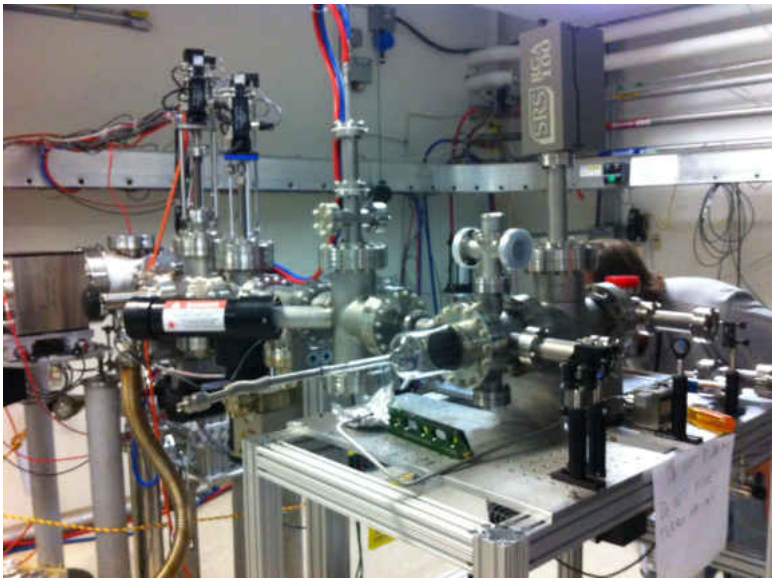

FIG. 21: A photograph of our beam machine being connected to the FEL vacuum.

chambers were separated with a MgF_2 window. The window was held in place with a window clamp on a double-sided CF flange, shown in Fig. 22. As mentioned earlier, during this experiment we were photon-starved, so we were concerned that background Kr atoms would scatter the few resonant photons before they made it into the atomic beam. To counter this, the tube length was calculated so that the MgF_2 window was about 4.5 mm away from the edge of the atomic beam. A postdoc in our research group, Will Williams, calculated the intensity of the 123 nm beam as it propagated through the chamber, and determined that at this distance and at the pressures that we ran, less than 10 percent of the resonant photons would be absorbed by background Kr. Opposite the MgF_2 window was an uncoated window that let the FEL beam out of the chamber and into a beam dump. The detection chamber of the vacuum system was modified to allow for fluorescence detection of Kr^*, and is described in detail in Subsection 3.4.7.

3.4.2 FEL PREPARATION EXPERIMENTS

Going into the experiment, we had several concerns about the FEL. First, we worried that if the light from the 3rd harmonic was not sufficiently separated from the rest of the FEL light, it would heat up and damage the MgF_2 window separating the two vacuum systems. A thermistor was installed on the side of the window, and

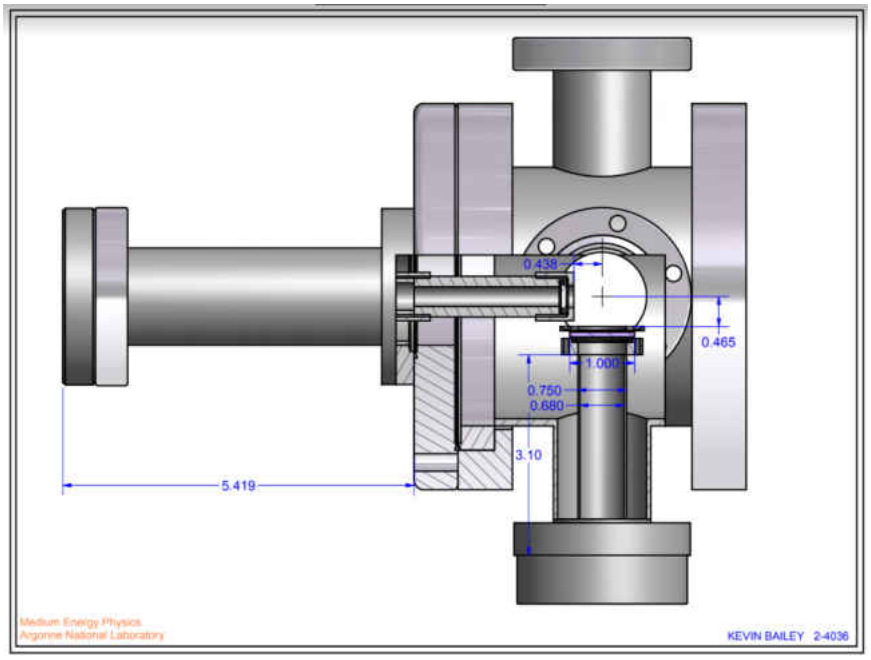

FIG. 22: A CAD drawing showing how the MgF_2 window is mounted within our beam machine. In this diagram, the Kr beam enters from the left. The FEL beam enters from the bottom. This image was made by Kevin Bailey at ANL, in preparation for the FEL experiment.

we monitored its voltage, while the FEL was run. We determined that there was no change in temperature and we did not have to worry about the window breaking.

Our second concern was that the FEL would ionize the already highly excited metastable atoms before they could exit the excitation region. Out of the metastable state, there exists a highly energetic transition with unknown line width and centered at 369.8 nm. At 370.5 nm, the spectral tail of the fundamental FEL beam could result in a resonance enhanced multiphoton ionization process. To test this, we installed a large glass tube to the front of the vacuum chamber (see Fig. 24). RF coils were placed around the tube and were used to create a discharge and produce metastable Kr. Further downstream, the metastable Kr atoms were detected by scattering an 811 nm laser off them. We observed and characterized the 811 nm florescence with a photodiode. We initially did not detect any metastable loss when the FEL light was allowed to overlap the atomic beam. After employing phase-sensitive detection, we observed a very small decrease.

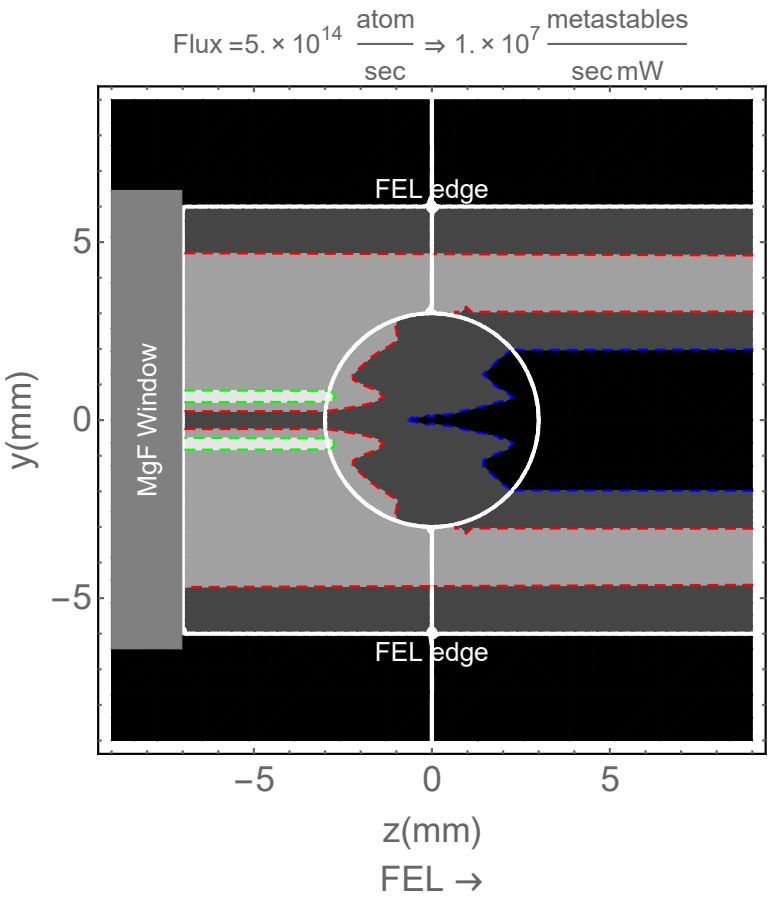

FIG. 23: A 2D cross section of the propagation of resonant photons through our atomic beam. In this figure, the atomic beam is propagating into the page. The FEL enters the chamber through the MgF_2 window shown on the left, and travels to the right. The dashed green lines mark the regions where the FEL resonant photons are at 0.9 of their max intensity; the dashed red lines mark where they are at 0.5 of their max intensity; the dashed blue lines mark where they are at 0.1 of their max intensity. Image courtesy of Dr. W. Williams.

FIG. 24: A photograph taken at the FEL, during the ionization test. It shows the glass tube that was mounted to the front of the beam machine. You can clearly see the glow from the RF discharge. The dark section in the middle is the shielding around the RF coils. In this photo, krypton gas is propagating from left to right. Metastable krypton atoms excited in the RF plasma continue into the chamber and the detection region, not shown in the picture.

3.4.3 FEL 3rd HARMONIC 123 nm PHOTONS

At 123 nm, the spectral output of the FEL is roughly Gaussian with a FWHM of 3 nm and no gaps in its profile. It is worth noting that the spectral width varies from shot to shot and 3 nm is likely best case. During the experiment our power ranged from 1 mW to 1.5 mW, which corresponded to a photon flux of about 1×10^{15} photons/s. Powers were not measured directly, but instead estimated from the fundamental power by facility staff. The laser has a repetition rate of 5 MHz and pulse length of 300×10^{-12} s. Unfortunately the FEL beam is larger than the capillary plate, and around 2/3 of the light never came into the excitation region. Fortunately we were able to overlap the most intense parts of the beam.

3.4.4 811 nm LASERS

To provide 811 nm photons for fluorescence detection, a diode was placed into a Littrow ECDL, illustrated in Fig. 25. The cavity consists of a collimation lens directly in front of the diode, and a 1800 grooves/mm optical grating for frequency selection. The grating is mounted onto a Thorlabs mirror mount, and has a piezo installed to adjust the horizontal displacement and scan the laser frequency. The typical operating current was 60 mA, provided by a Lightwave LDX-3525, while the temperature was stabilized by a thermoelectric cooler (TEC), with feedback provided by a 50 kΩ thermistor. A Lightwave LDT-5525 measured the resistance through

the thermistor, and provided the current to the TEC to complete the temperature stabilizing feedback loop. The entire cavity was housed inside a plastic box and mounted onto a large aluminum heat sink for further temperature stabilization.

The laser output was sent directly into an optical isolator to protect the laser from feedback. From there, a polarizing beamsplitter cube was used to separate the beam into two parts. The first part continued onwards to two guiding mirrors and was launched into a Thorlabs fiber optic cable. It was then available to be sent to the experimental apparatus. The second part was sent to a sub-Doppler spectroscopy module, consisting of two polarizing beamsplitter cubes and $\lambda/2$ waveplate, two mirrors, a photodetector, and a Kr vapor cell. The cell used an RF coil to create a plasma discharge in it, as described in section 3.2.3. The net result is a single mode fiber coupled output, with 15 mW of power and a bandwidth of less than 1 MHz.

3.4.5 819 nm LASERS

We use a commercial Sacher TEC120 Littrow-configured ECDL as a master laser source, illustrated in Fig. 26. Under typical operating conditions, the TEC120 has a current around 100 mA, and a power output of 40 mW. A polarizing beamsplitter sends a portion of the light sent to an SAS setup, and the rest continues on. For highest metastable excitation efficiency we require as much power as possible, so the portion of the master laser that is not sent to the SAS is coupled into a Sacher TEC400 tapered amplifier. A typical power output is 100 mW, of which most is coupled into a light pipe and sent to the experiment. The light pipe does not provide the single mode output that a fiber provides, however this is not a problem over the 50 cm that the light propagates. In exchange for a multimode output, the light pipe has a coupling efficiency of 90% to 95%, as opposed to 50% to 60% in a single mode fiber.

We had difficultly creating a SAS peak large enough to lock to. We tried many vapor cell pressures and intensities, but overall did not obtain the same reliable locking signal that we had for all of our other transitions. We suspect that it has something to do with exciting out of a “leaky” ground state, and the problem was investigated further by ODU student Alexander Maddock in his senior thesis. Because of this, we generally did not try to lock the 819 nm laser, and instead scanned through resonance.

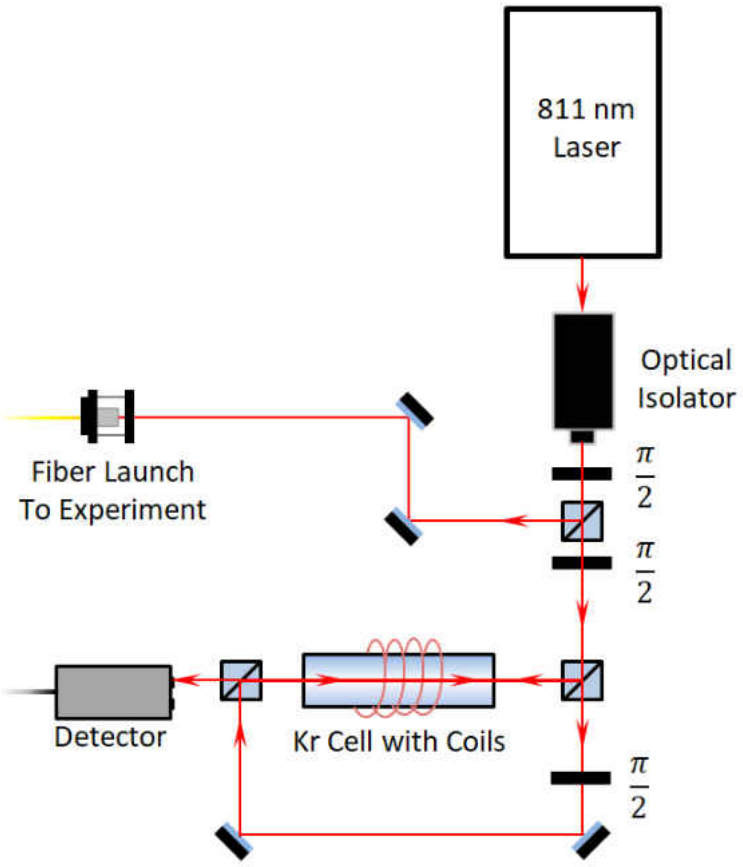

FIG. 25: A diagram representing the optical train for the 811 nm Kr laser. The power is split between the SAS module and a fiber that launches into the experiment. A polarizing beamsplitter and half waveplate are used to control how much is sent to each branch.

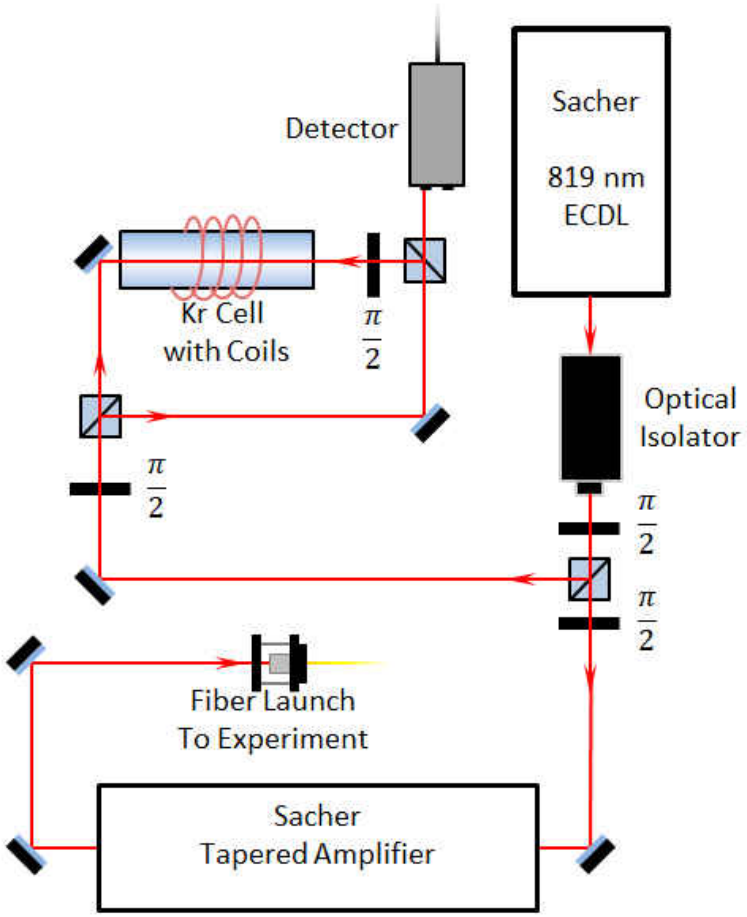

FIG. 26: A diagram representing the optical train for the 819 nm Kr lasers. The power from the master laser is split between the SAS module and tapered amplifier. A polarizing beamsplitter and half waveplate are used to control how much is sent to each branch. The output of the tapered amplifier is launched into a fiber and sent to the experiment. An optical isolator protects the tapered amplifier from back reflections.

3.4.6 FEL EXCITATION EXPECTED EFFICIENCY

We use a system of equations very similar to the one described in Section 2.1 to model the efficiency of this excitation method. The system previously described is for CW lasers, however the FEL is a pulsed laser. We have replaced R_1 with $R_1(t)$ to account for this difference. Where R_1 would be the excitation rate if the FEL were to run continuously, $R_1(t)$ takes the form:

$$R_1(t) = \begin{cases} R_1, & \text{Laser On} \\ 0, & \text{Laser Off} \end{cases}$$

And thus our system of equations becomes:

$$\frac{dN_g}{dt} = -R_1(t)N_g + N_1\Gamma_{1g} \tag{48}$$

$$\frac{dN_1}{dt} = R_1(t)N_g + N_2\Gamma_{21} - (R_2 + \Gamma_{1g})N_1 \tag{49}$$

$$\frac{dN_2}{dt} = R_2N_g - (\Gamma_{21} + \Gamma_{2*})N_1 \tag{50}$$

$$\frac{dN*}{dt} = \Gamma_{2*}N_{2*} \tag{51}$$

The FEL is pulsed at 5 MHz, however its power is measured over several seconds. We use the following expression to extract the "on time" power, P_{pulse}, from the average power, $P_{average}$:

$$P_{pulse} = \frac{P_{average}}{f_{FEL} \times t_{pulse}} \tag{52}$$

where f_{FEL} is the repetition rate of the FEL, and t_{pulse} is the FEL pulse duration.

The FEL has a very broad output, and only a small fraction of its photons are resonant. It has a Gaussian spectral profile several nanometers wide, centered around 123.5 nm. Our atoms are propagating within an atomic beam, so Doppler broadening is not an issue and the line shape of the first transition approaches a Lorentzian. Only the part of the FEL spectral profile that overlaps the Lorentzian will drive the transition. This overlap g_{FEL} can be approximated as the ratio between the FWHM of each line shape.

$$g_{FEL} = \frac{\Delta\omega_{123}}{\Delta\omega_{FEL}} \tag{53}$$

We find the following saturation parameter

$$s_{123} = \frac{g_{FEL} \times I_{123}}{I_{sat,123}} \tag{54}$$

where I_{123} is the full intensity of the FEL beam, and $g_{FEL} \times I_{123}$ corresponds to the fraction of the intensity that is the correct frequency to drive the transition. We may now calculate the excitation rate out of the ground state

$$R_1 = \frac{\Gamma}{2}\frac{s_{123}}{1 + s_{123}} \tag{55}$$

Our 819 nm laser has 75 mW of power coming out of the fiber, and is retroreflected back onto itself. It has a waist of 11 mm, chosen to match the FEL waist. Unlike the FEL, the 819 nm laser is CW, and so R_2 is not a function of time. Together, this yields the following saturation parameter and R_2:

$$s_{819} = \frac{I_{819}}{I_{sat,819}} = 560 \tag{56}$$

$$R_2 = \frac{\Gamma_2}{2}\frac{s_{819}}{1 + s_{819}} = 5.4 \times 10^6 \frac{1}{s} \tag{57}$$

The system continues to evolve for as long as an atom remains in the excitation region. This time may be calculated using the definition of velocity, $v = d/t$. In this situation, d is equal to the length of the excitation region, which we define as twice the laser waist of the FEL. The distribution of speeds within an atomic beam is not well described by a Maxwell-Boltzmann distribution [43]. Instead, we use Eqns. 58 and 59 to calculate the most probable speed, v_p. At room temperature, the most probable speed of a Kr atom within a well-collimated atomic beam is 283 m/s, and is given by

$$v_p = \sqrt{3/2}\alpha \tag{58}$$

where α is the most probable speed within a Maxwellian distribution, and is described as

$$\alpha = \sqrt{2kT/m} \tag{59}$$

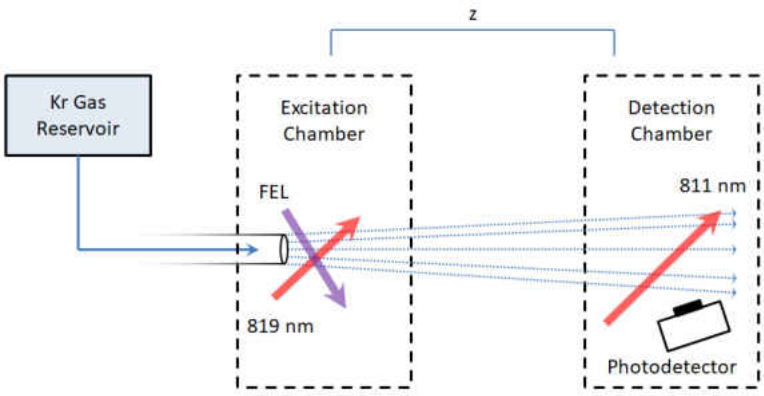

FIG. 27: A schematic showing the experimental apparatus during the FEL experiment.

In collaboration with Will Williams, a Mathematica script was written to numerically calculate the progression of the system over the 39 μs that an average atom spends in the excitation region. We did not include experimental numbers for the FEL powers or line width. In the preliminary work at Argonne National Laboratory, our collaborators were anticipating an output of 100 mW with a 0.25 nm FWHM line width. In our subsequent meetings with the FEL staff in months leading up to our run, it became apparent that these expectations would not be realized. During the actual run, the FEL provided us with 1.5 mW average power with a FWHM of 3 nm. Expected efficiency ranged from near 1 percent with the initial numbers, to as low as 10^{-7} with the final numbers.

3.4.7 FLUORESCENCE DETECTION

In our previous experiment, we successfully used the emission of a 427 nm decay photon to detect metastable excitation. Instead of a 427 nm photon, our new 123 nm + 819 nm excitation scheme emits a 760 nm decay photon. In and of itself, this is not a problem. However, the MgF_2 window fluoresces when the FEL light passes through, and a portion of the radiation given off is at 760 nm. Instead of relying on a decay photon, we use a detection laser to scatter many photons off each Kr^* atom, and search for those.

Atoms within the atomic beam propagate from the excitation chamber to the detection chamber as shown in Fig. 27. Once within the detection chamber, they pass through a 811 nm laser beam that drives the $5s[3/2]_2 \rightarrow 5p[5/2]_3$ transition. The

beam is retroreflected back onto itself to increase the scattering rate. Its diameter is 5 mm, its power is 15 mW, and a single atom scatters an average of 496 photons as it passes through. A collection lens directs a portion of the fluorescent photons through a 810 nm interference filter and into a photodetector. After accounting for spherical aberrations and distance, the lens has a collection solid angle of 9.4×10^{-4} sr. This means that on average, 1 out of every 1080 scattered photons reaches the detector, and on average each atom scatters 0.46 photons into the detector.

3.4.8 FEL RESULTS AND CONCLUSIONS

We were unable to detect production of metastable Kr while using the FEL. While disappointed, we were not surprised by this result. As our understanding of the FEL beam characteristics continued to improve in the weeks leading up to our beam time, we refined our predictions and saw that detection looked less and less likely. By our first day at the facility, we understood that even if we achieved our best case efficiency, we would still be pushing up against our detection limit. If the FEL staff had been able to upgrade their frequency tuning with a second optical grating, it is possible that the beam would have been narrowed enough to be of more practical use to us.

In correspondences with FEL staff after the experiment, a further problem came to light. There was uncertainty around the 3 nm FWHM figure that they provided us with, which as it turns out, was a time-averaged width. It is unclear whether each pulse has a FWHM of 3 nm centered around resonance, or if the pulses are much narrower but bounce around from shot to shot. If it is the latter, then it is possible that only a few shots out of a million are capable of driving the transition we need, and the FEL becomes an even less realistic option.

Despite the obvious drawbacks of a user experiment, we were initially hopeful that the FEL might be useful for ATTA. At the conclusion of the experiment, we were able to rule it out as a possible method to replace the RF discharge. Even though this method proved not to be viable, we found the effort fruitful. Our understanding of our apparatus improved, and the experience provided us with the impetus to further enhance our detection capability. We decided that we would no longer rely on photon detection via scattering by an external laser, and instead would rely on the photons emitted when the metastable Kr decays back down to the ground state.

3.5 UV LAMP EXCITATION

A particularly exciting source of UV photons is a commercially available lamp made by Resonance Ltd., which we learned of while carrying out the NASA and JLab experiments. The lamp consists of a small Kr cell, in which a RF discharge creates a plasma. Within the plasma, atoms are collisionally excited across a wide range of states, and radiatively decay back to the ground state. During this process, 123 nm photons are emitted. The lamp plasma is separated from our vacuum chamber with a MgF_2 window, allowing the UV light to pass through and excite ground state Kr atoms within our atomic beam. Compared to the FEL, the lamp provides the obvious benefits of being usable on a tabletop, as opposed to being a user experiment at a remote facility. Compared to the ArF excimer laser, the lamp is, smaller, cheaper, and more practical. This lamp is similar to the one described in Ref. [17], except this commercially available model has an anticipated functional lifetime almost 10,000 times longer. While the accompanying documentation claimed that at 123 nm, the lamp had to have an absolute intensity of 1.65×10^{15} photons per second per steradian, it was initially unclear how much of that was pressure and Doppler broadened out of the natural linewidth of the first transition. Characterization of the Resonance Ltd. lamp is described in Section 3.5.3.

3.5.1 Ti:SAPPHIRE

Throughout the entirety of the lamp and FEL experiments, availability of 123 nm photons limited our metastable efficiency. We cannot allow a Kr atom to decay back to the ground state after absorbing a 10 eV photon, and so we need as much 819 nm light as we can produce to drive the $5s[3/2]_1$ to $5p[3/2]_2$ transition as hard and efficiently as possible. At the FEL, we used a Sacher ECDL and tapered amplifier because they were mobile and could be used outside of our laboratory with relative ease. The lamp excitation experiments occurred within our own laboratory, so we instead chose to use a Ti:Sapphire laser. Compared to the 80 mW achieved with the Sacher lasers, we had a resonant power of 180 mW with our Ti:Sapphire.

Our Ti:Sapphire laser is pumped with 10 W from a Coherent Verdi laser. Its wavelength is tunable over to 819 nm, and we achieve an output power of 180 mW. While below spec, it is still an improvement of the Sacher tapered amplifier. We sent a small portion of the light into an SAS module to serve as an absolute frequency

measurement and coupled the rest into a fiber optic cable. The light was launched into the atomic beam machine, and retroreflected back onto itself for an even higher intensity.

3.5.2 UV LAMP EXCITATION VACUUM CHAMBER MODIFICATIONS

The UV lamp was installed in the excitation chamber. It connects to the vacuum system with a quick-disconnect CF flange that allows us to adjust how far into the chamber the bulb extends. We installed it in such a way that it is directly over the atomic beam as the beam enters the chamber. To minimize the scattering of high energy photons from the lamp into our detection, we installed a bronze tube orthogonal to both the atomic beam and the lamp. The tube was mounted in the same windows that the 819 nm light entered through. A hole was drilled into it so that the lamp could be mounted flush and prevent light leakage. Two separate holes were drilled to allow the atomic beam to pass through.

3.5.3 UV LAMP CHARACTERIZATION

We characterized the output of the Resonance Ltd. lamp before we used it in an excitation experiment. A Channeltron detector was installed in the detection chamber in such a way that the atomic beam propagated directly into the cone. Channeltrons are discussed later in this dissertation, but for right now it is important to understand that Channeltrons detect high energy photons or ions. When the lamp was turned on, the Channeltron detected a steady background of UV photons incident on its cone. After allowing the lamp to warm up, we flowed Kr gas into the chamber with a total flux of 4×10^{13} atoms/s. Channeltron counts immediately increased by 50,000 counts/s. Further investigation established the new counts were proportional to Kr gas flow. We concluded that the counts were either from 123 nm photons resonantly scattering off the Kr into the Channeltron, or from ions produced by resonance-enhanced multiphoton ionization.

To determine if the counts were from ions, we designed and installed a pair of stainless steel parallel plates directly in front of the Channeltron cone as shown in Fig. 30. We spot-welded wires to them, and one of the plates was grounded while the other plate had a voltage applied to it. The resulting electric field was several orders of magnitude larger than necessary to deflect any ions that attempted to pass

FIG. 28: A photograph of the UV lamp, as seen mounted into the vacuum chamber. The plasma forms near the center of the chamber.

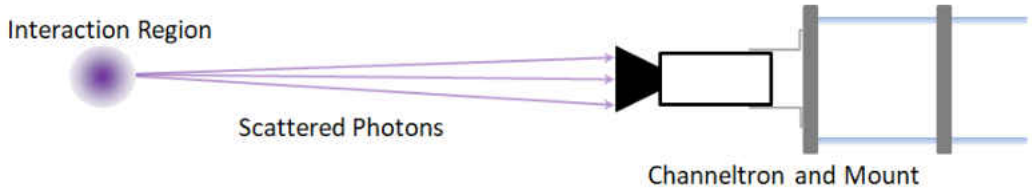

FIG. 29: A diagram showing resonant UV photons scattering out of the interaction region and into the Channeltron.

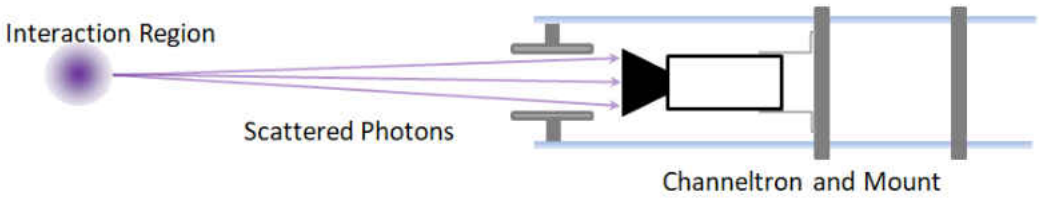

FIG. 30: The Channeltron continued to detect counts after ion deflecting parallel plates were installed in front.

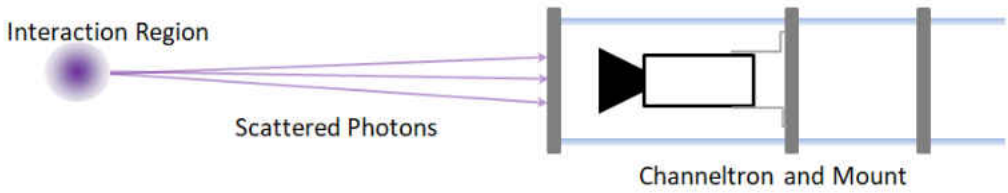

FIG. 31: When the optical path between the interaction area and Channeltron was blocked, no more counts were detected.

between them.

With the plates installed, we saw no change in the count number. At this point we considered the idea that a convoluted electric field could potentially guide ions around the parallel plates into the Channeltron cone. To test further, we installed an optical block through the hole that photons would be scattering through, as shown in Fig. 31. The block kept the Channeltron cone out of line of sight with the Kr gas, but would not prevent ions from following stray electric field lines around and into the detector. No further counts were detectable. This confirmed that the counts did in fact come from photons that were scattered by the Kr gas.

Finally, out of concern that the counts came from Rayleigh scattering instead of resonant scattering, we replaced the Kr gas with Ar. No counts could be detected from scattering off the Ar gas. Upon switching back to Kr, we again observed scattering, confirming that the counts are atom-specific. After this series of tests, we were confident that the counts came from exciting the Kr gas. Using the counts, we backed out the excitation rate provided by the lamp, R_{lamp}, with the relationship

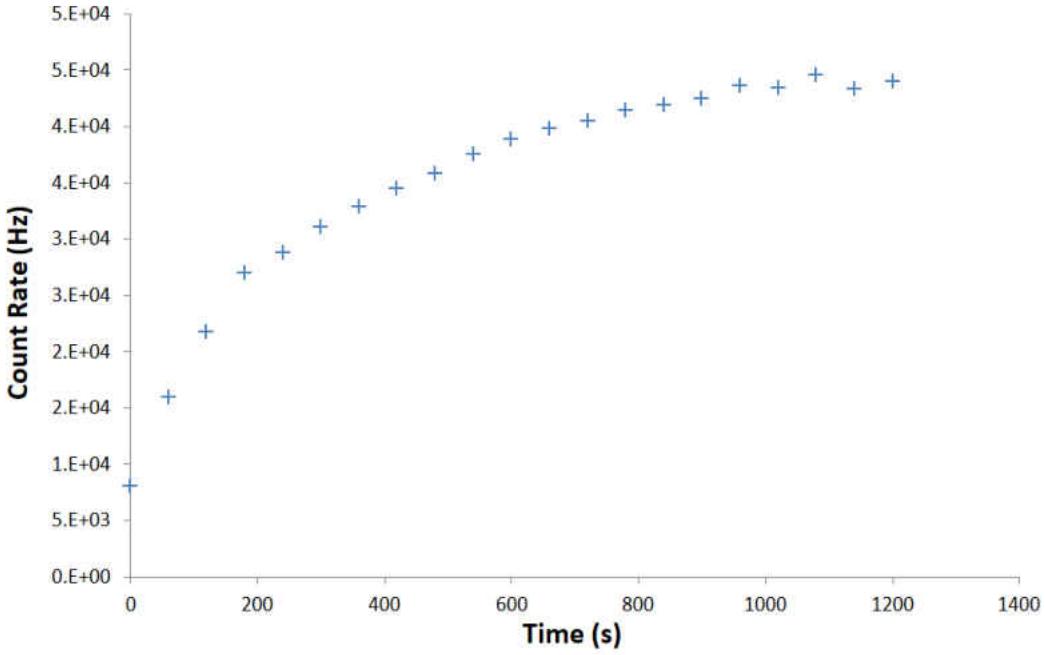

FIG. 32: A plot showing results from the UV lamp warm-up test. The lamp takes about 1000 s to reach equilibrium.

$$R_{lamp} = \frac{4\pi f_{counts}}{Q.E. \times N_{atom} \times \Omega \times C.E. \times A} = 5Hz \tag{60}$$

where f_{counts} is the measured count rate, $Q.E.$ is the quantum efficiency of the detector, Ω is the Channeltron solid angle, $C.E.$ is the collection efficiency of the photon counter as determined by the discriminator level, N_{atom} is the number of atoms within the excitation region, and A is the attenuation of the resonant photons as they propagate through the Kr-filled chamber.

In addition to resonant photon flux, we were also interested in the lamp's warm-up time. The literature from Resonance Ltd. stated that a warm-up time existed, but did not provide specifics. After letting the lamp relax overnight, we turned it on an measured Channeltron counts. Measurements were taken in 10 second windows, once a minute. Figure 32 shows the resulting data, and we see that UV photon flux seems to reach steady state at around 1000 seconds. In all of our further work, we delivered about allowing at least 20 min warm-up time before we began taking data.

3.5.4 UV LAMP EXCITATION EXPECTED EFFICIENCY

Similar to the other two excitation methods, we will again use rate equations to model the evolution of the system over time. The system is described by Eqns. 61 through 64. In this subsection, we describe how we determined the experimental coefficients used within.

$$\frac{dN_g}{dt} = -R_1 N_g + N_1 \Gamma_{1g} \tag{61}$$

$$\frac{dN_1}{dt} = R_1 N_g + N_2 \Gamma_{21} - (R_2 + \Gamma_{1g}) N_1 \tag{62}$$

$$\frac{dN_2}{dt} = R_2 N_g - (\Gamma_{21} + \Gamma_{2*}) N_1 \tag{63}$$

$$\frac{dN*}{dt} = \Gamma_{2*} N_{2*} \tag{64}$$

Coupling between the ground state and the first excited state is provided by 123.6 nm photons emitted from the UV lamp. In Section 3.5.3, we determined that atoms exposed to the lamp scatter 5 photons/s.

$$R_1 = 5Hz \tag{65}$$

As mentioned above, instead of the Sacher ECDL and tapered amplifier used during the FEL experiment, we now used a Ti:Sapphire laser to provide the 819 nm light. The laser had 160 mW retroreflected power and a 12.7 mm waist. It provided the following saturation parameter and scattering rate:

$$s_{819} = \frac{I_{819}}{I_{sat819}} = 1,200 \tag{66}$$

$$R_2 = \frac{\Gamma_{21}}{2} \frac{s_{819}}{1 + s_{819}} = 5.5 \times 10^6 \frac{1}{s} \tag{67}$$

Equation 59 showed us that the v_p of a room temperature Kr atom is 283 m/s, and so on average each atom be will spend 45 μs within the excitation region. A Mathematica script numerically calculates how this system evolves with all the atoms starting in the ground state, over the time frame t=0 to t=45 μs. Depending on the input parameters, the script shows each atom having a probabilty of being excited

into the metastable state ranging from 10^{-5} to 10^{-6} by the time it leaves the excitation region. The wide range stems from uncertainty in the Channeltron quantum efficiency used to back out R_1, and from uncertainty about the exact geometry of the lamp output. However, either of these numbers should be high enough to detect metastable production.

3.5.5 CHANNELTRON COLLISIONAL QUENCHING DETECTION

A Channeltron is a type of electron multiplier. The collection end of the device is shaped like a cone and is kept at a high voltage. The voltage may be either positive for collecting negative ions and electrons, or negative for collecting positive ions. Electrons are emitted when a charged particle impacts the cone. Through a process called secondary emission, each time emitted electrons collide with the interior walls of the detector, more electrons are released. As the electron pulse works its way through the detector, the process is repeated many times and a single electron may be amplified by 10^5 to 10^7. Our Channeltron was a Sjuts model KBL 20RS, which has a maximum gain around 2×10^8 and a collection cone diameter of 25 mm.

Electrons may thermally emit from anywhere within the detector. When this happens, a pulse moves through the detector gaining further electrons, just like a real count. Most of the time, the thermal emission will not have originated at the cone, so the final pulse height will be smaller because it was not able to travel as far within the detector. To filter out thermal pulses, our electronics were set to reject any pulse with a height below 6 mV. A more detailed description of Channeltron characterization is found in Section 5.3.1.

In addition to electrons, ions, and high energy photons, Channeltrons also detect collisions whose total energy exceeds detection threshold. Metastable atoms typically have very large internal energies that may be released during a collision. Channeltrons have regularly been used to detect highly energetic metastable He atoms, and have also been used to detect metastable Ar atoms, which have internal energies close to that of Kr.

The mount for the Channeltron was designed to allow us to control its distance from the excitation chamber. If it was mounted too close, it would be flooded with 10 eV photons from the lamp, but every millimeter we moved the Channeltron decreased the collection efficiency. See Figs. 33 and 34. The Channeltron cone had a radius of 12.5 mm. Using the calculations described above in Section 3.1, we mapped

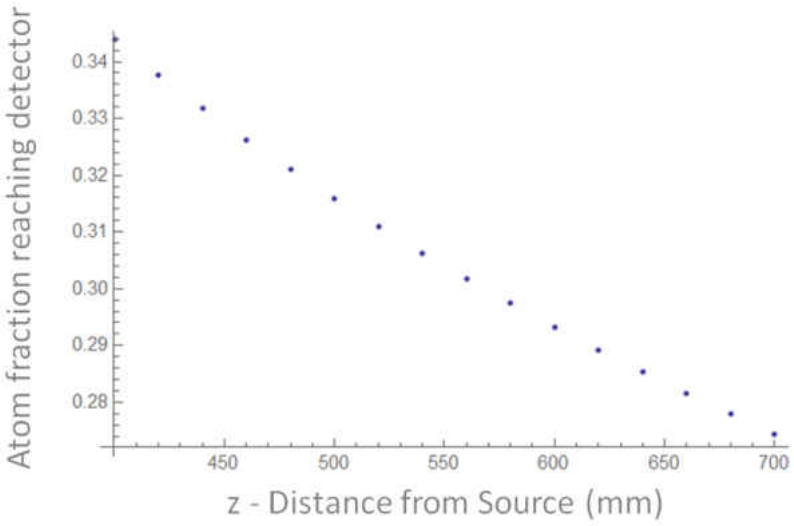

FIG. 33: A plot showing the calculated fraction of the atomic beam hitting the Channeltron cone at various distances from the capillary plate, z.

out atomic beam flux vs. position. We chose to mount the Channeltron 200 mm from from the capillary plate, at which point 43% of the atom beam will make it into the cone. Its output was sent into a SR445A preamplifier, and the pulses were counted in a SR400 photon counter.

As described in Section 3.5.3, we successfully used the Channeltron to characterize the plasma lamp. However, when we attempted to use this detection method to count Kr^* atoms, we were unable to find any. An updated detection method using the Channeltron is described in the next subsection.

3.5.6 CHANNELTRON OPTICAL QUENCHING DETECTION

While a literature search revealed several instances where collisionlly quenching into a CEM was used to detect He^* [44][45], we were unable to find similar cases with Kr^*. We suspect this is the case because significantly more work has been done with He^* than Kr^*. At the time of writing, we still strongly suspect the previous detection technique will work with Kr^* as well. Nevertheless, we noted that at 20 eV, He^* is more energetic than Kr^*, and thought that perhaps this was the source of our missing Kr^* counts.

When we characterized the lamp, we confirmed that the Channeltron could detect 10 eV photons. We developed a new scheme based around this. We mounted the

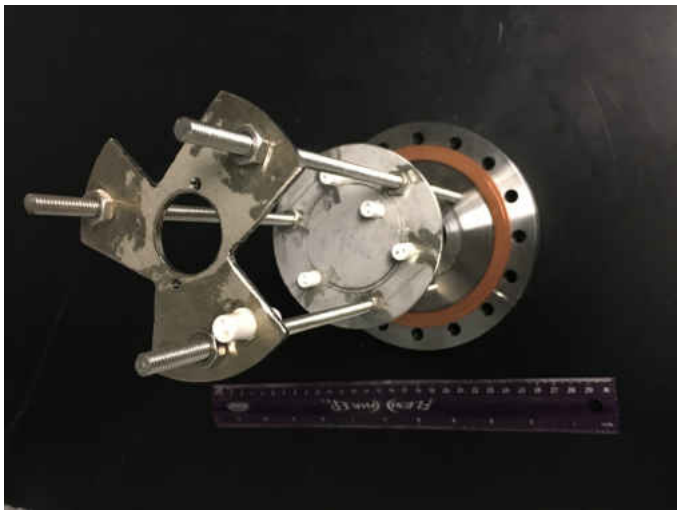

FIG. 34: A photograph of the mount built to install the Channeltron. It can be slid higher or lower to place the Channeltron cone at the desired distance, z.

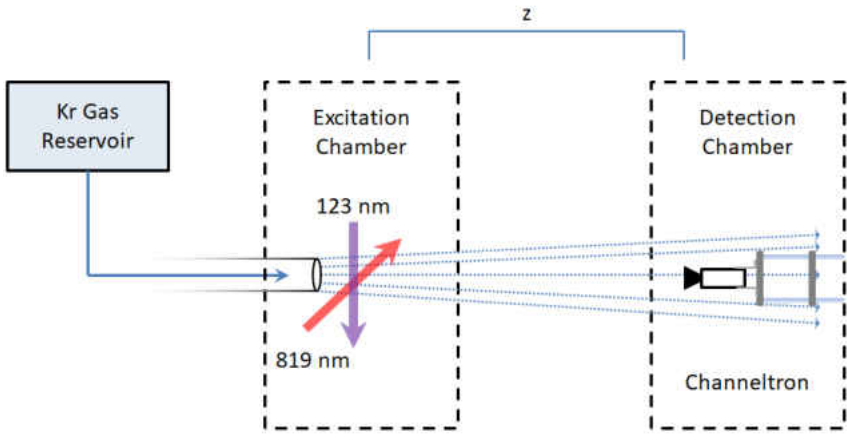

FIG. 35: A schematic of the experimental apparatus while using the Channeltron collisional quenching detection method.

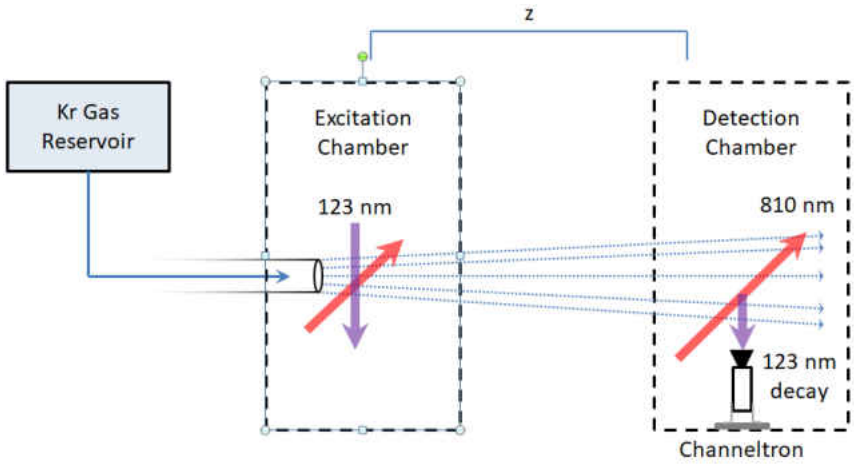

FIG. 36: A schematic of the experimental apparatus while using the Channeltron optical quenching detection method.

Channeltron perpendicular to the atomic beam and within the detection chamber, as shown in Fig. 36. The top of the cone and the beam were separated by only 10 mm. A laser was locked to the $5s[3/2]_2 \rightarrow 5p[5/2]_2$ quench transition. Atoms excited to the $5p[5/2]_2$ state may spontaneously decay to the $5s[3/2]_1$ state, and then back to the ground state. In the process, they release a 10 eV photon. The Channeltron then collects these UV photons.

A near-light-tight box was built around the detection area. It was critical to ensure that no 810 nm quench photons leak upstream. The quench laser was sent into the chamber in a similar method to the 811 nm detection laser in Section 3.4.7, in which a series of baffles were used to attenuate scattering off the windows. The Channeltron was mounted inside an aluminum box. Using the beam size calculations in Section 3.1.2, we drilled a 3 mm entrance hole and 4 mm exit hole. The entrance hole had a cross section that would allow 31% of the beam to pass through, and the exit hole had a cross section that would allow 36% of the beam to pass through. The exit hole was higher to ensure that we did not accidentally create a quasi-reservoir within the box, where atoms end up working their way back out the entrance hole. Two more holes were mounted to allow the 810 nm quench light into the box. Copper pipes were installed to connect the window baffle system to the box, allowing no point at which 810 nm light might scatter into the upstream atomic beam. However, again with this this method we still did not detect any metastable Kr.

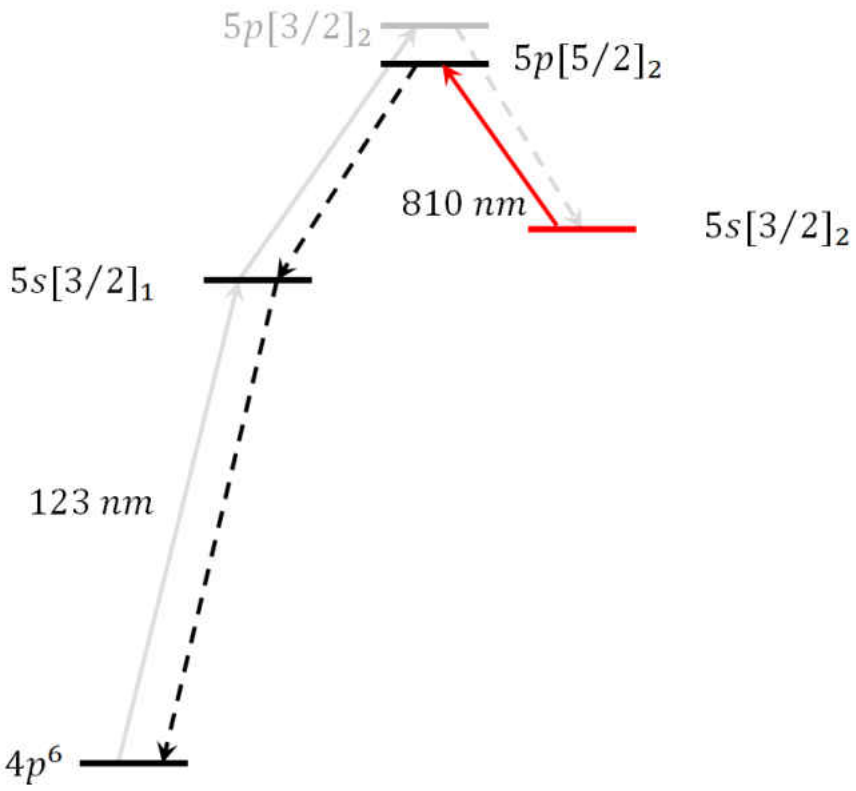

FIG. 37: A diagram of the atomic levels accessed during the optical quench.

3.5.7 RETURN TO FLUORESCENCE DETECTION

At this point, we were surprised to have not detected any metastable Kr using the lamp. The problem had to be one of the two options: 1) We were not exciting Kr*, or 2) we were not detecting the Kr* that we produced. After characterizing the lamp, we were confident that we had a reliable source of 10 eV photons. Saturated absorption spectroscopy also showed us that we had correctly accessed the 819 nm transition. We also know that when 123 nm and 819 nm is incident on Kr vapor, it excites to the J=2 metastable state [16]. With this in mind, we returned to fluorescence detection as described in Section 3.4.7. In a disconcerting pattern, we once again found no detectable trace of Kr*.

3.5.8 A MYSTERY SOLVED

New information came to light after we had switched our focus to the photoassociation project. While designing our experiments, we considered the attenuation of the metastable beam due to collisions with background atoms. In our original calculations, we determined that at 5×10^{-5} Torr background pressure, 93% of the excited Kr* atoms would safely make it into the detection chamber. In discussions with our collaborators, after we had already switched focus to photoassociation, we learned that a new measurement of the Kr* collisional cross section had been made, and that it was an order of magnitude larger than the 4.2×10^{-10} m^2 that we had used. With the new cross section, we calculate that around 1% of the metastable Kr will successfully propagate into the detection chamber.

Upon further analysis, we realized that our chosen atomic beam flux likely led to a second problem. We were operating in a photon-limited regime and were strongly motivated to not waste a single 123 nm photon. In Fig. 23 we demonstrated how we had chosen an atomic flux to ensure full absorption of the FEL 3rd harmonic. However upon further consideration, we noted that the atoms at the center of the atomic beam are the atoms most likely to propagate to the detection chamber, while atoms along the edge of the atomic beam are less likely to make it to the detection region. In our effort not to waste any 123 nm photons, we had inadvertently set up a situation where the atomic beam was so dense that most of the 10 eV excitation happened along the outer edge.

We find it highly likely that metastable Kr* was produced during the entirety

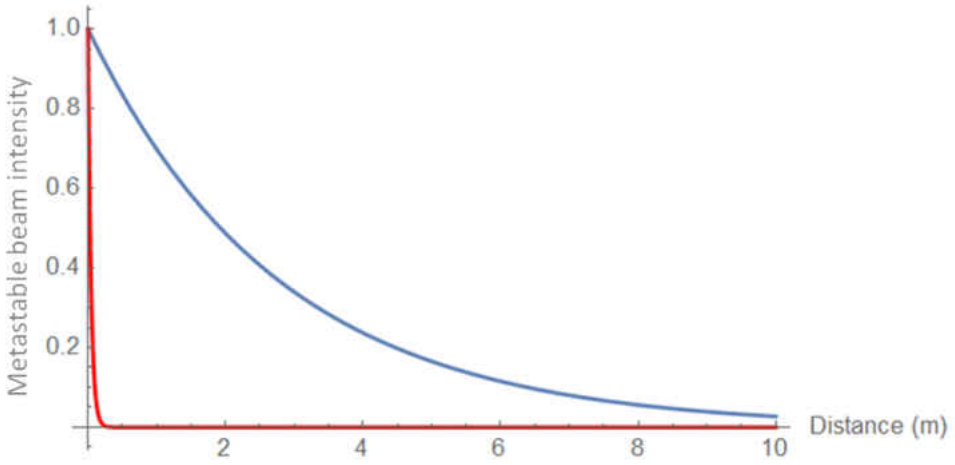

FIG. 38: Both plots show the intensity of an atomic beam as it propagates through background gas. The blue plot uses the original collisional cross section that we used when designing the apparatus. The red plot shows beam attenuation with the updated cross section.

of the lamp experiment. We suspect that most of the excited Kr^* atoms collided with background gas before they were able to make it into the detection region. We believe that the Kr^* signal was even further attenuated by the higher probability of atoms along the outer edge of the atomic beam to absorb some of the limited 10 eV photons, and then fail to enter the detection region.

3.6 Kr METASTABLE EXCITATION - RESULTS AND CONCLUSIONS

In conclusion, we found that neither the ArF excimer laser nor FEL were suitable for ATTA. Our calculations suggest that the UV plasma lamp is a viable excitation method. While our lamp's predicted efficiencies in the 10^{-5} to 10^{-6} range are lower than the 10^{-4} achieved within an RF discharge, newer models are becoming available that increase photon flux by more than an order of magnitude. Additionally multiple lamps may be used in concert to further increase the efficiency. At Argonne National Laboratory, where the first ATTA was built, work continues on using UV lamps to replace an RF discharge, and in Germany, a group used a similar system to produce 123 nm photons for the first stage of metastable excitation [18]. Within our group, the project was revived by Lindsay Thornton, who built a resonant build-up cavity for the 819 nm light as part of her master's thesis. At the time of writing, a new

graduate student, Josh Frechem, is in the process of setting up a cell experiment using the lamp.

In retrospect, we suggest that this work should have initially been done within a cell, not an atomic beam. Both the FEL and the plasma lamp were sources of broad 123 nm photons. In all of this work, availability of 123 nm photons continued to be the limiting factor. Atoms within an atomic beam have a small distribution of translational velocities. Had the experiment been conducted within a cell, the atoms would have had a larger distribution of velocities and would have interacted with a larger portion of the 123 nm light. Atoms with high velocities would have experienced Doppler broadening of the natural linewidth to overlap with more of our 123 nm light source. The net effect would have been an increase in Kr^* production and a larger signal size with which we could optimize our excitation schemes, although ATTA uses a beam. In addition, we would have avoided the collisional quenching problem that plagued us throughout much of the work.

At the time, the reasons we chose to work within an atomic beam seemed compelling. This experiment was originally conceived of as a FEL experiment, and both ArF excimer and UV lamp experiments were identified as potential light sources only after preparations for the FEL had already begun. At the FEL, a cell experiment would have been limiting. The fluorecing MgF_2 window that separates our vacuum from the FEL vacuum would have overpowered any signal from 760 nm decay photons. An experiment within an atomic beam allowed the Kr^* to move to a separate location away from the complications caused by the 123 nm, 819 nm, and fluorescent photons, and search in a relatively noise-free environment. An atomic beam also had another large draw. ATTA is an atomic beam, and so any results we produced would be more easily transferable to ATTA.

3.7 TRANSITION TO PHOTOASSOCIATION SPECTROSCOPY

Unfortunately, midway through testing the lamp, funding considerations necessitated a change of focus. I had originally been planning on traveling to Argonne National Laboratory to carry out the remainder of my research. However, at the time Argonne was only able to guarantee a single year of support. Therefore I decided to remain at Old Dominion University and work on a different project without fear of a future interruption. It is at this point that we bring the discussion of metastable Kr excitation to a close. In the next chapter, we start our discussion of photoassociation

spectroscopy.

CHAPTER 4

PHOTOASSOCIATION THEORY

The goal of this work is to build upon previous studies conducted within our group and perform photoassociation spectroscopy on a dense system of Rb + Ar* atoms. As mentioned in Chapter 1, the thermal spread in collision energies at room temperature is on the order of 10 THz, and so to have any hope of resolving individual vibrational features, our samples must first be cooled to temperatures below 1 mK. In this chapter, we cover two broad topics. First, we explain the theory behind laser cooling and trapping of atoms, and describe how we may reach the temperatures required to resolve excited molecular features. In the second half of this chapter, we use a semiclassical approach to gain insight into diatomic molecular structure. We then describe the shape of long range potentials for homonuclear and heteronuclear systems. Moving on, we discuss photoassociation to excited molecular states, and describe the channels through which the system may decay.

4.1 LASER COOLING

Resolution of photoassociation spectra may be drastically improved by conducting the experiment at temperatures below 1 mK. These ultracold temperatures may be achieved through laser cooling. In this section, we describe how these processes work. We start with a cooling technique called optical molasses. Then we describe how in addition to cooling, including a magnetic field allows us to confine atoms within a magneto-optical trap (MOT). We end the section by discussing some of the obstacles we face, and how a Zeeman slower and "repumper" laser allow us to overcome them.

While we will describe a variety of laser cooling and trapping techniques, at their core most revolve around scattering photons to apply an optical force on an atom in opposition to its velocity. In Section 2.1 we described how the scattering rate of a near resonant laser is highly dependent on detuning, as shown by:

$$R = \frac{\Gamma}{2}\frac{s}{1+s+(2\delta/\Gamma)^2} \tag{68}$$

where δ is the laser detuning from resonance, and s is the saturation parameter, which was previously defined in Eqn. 13 and is again shown here.

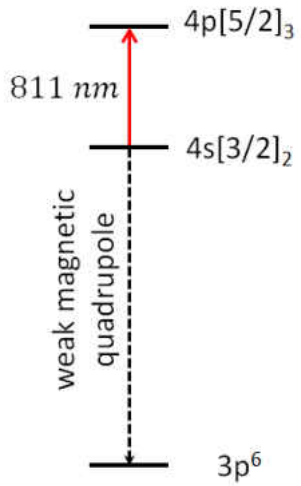

FIG. 39: A diagram of the Ar atomic states that we accessed during the course of this work. The metastable 4s[3/2] J=2 state was excited via electron collisions within an RF discharge, and not excited optically.

$$s = \frac{I}{I_{sat}} \tag{69}$$

With the understanding that photons have momentum $\hbar\vec{k}$, we find an atom will experience the detuning dependent scattering force

$$\vec{F} = \frac{\hbar\vec{k}\Gamma}{2}\frac{s}{1+s+(2\delta/\Gamma)^2} \tag{70}$$

Similar to the behavior of a Maxwell-Boltzmann distribution of velocities in a gas, a Gaussian distribution is often found within laser cooled vapors. This is the case within a MOT. An equivalent temperature may be assigned to the width of this distribution [35]. By selectively applying an opposing scattering force to atoms with higher relative velocities, we may lessen the width of the distribution and cool the sample. We may rely on the Doppler effect for our selectivity.

4.1.1 OPTICAL MOLASSES

Let us consider an on-resonance laser whose photons have angular frequency ω_o. We may detune it by some amount, δ. If we place an atom with an arbitrary velocity into the laser field, the atom will see a Doppler shifted laser frequency ω'

$$\omega' = \omega_o + \delta - \vec{k} \cdot \vec{v} \tag{71}$$

where $\vec{k}$ is the photonic wavevector. Equation 71 shows us that the probability of the atom interacting with the laser field is highest when the condition $\delta = \vec{k} \cdot \vec{v}$ is met. To form an optical molasses, we red-detune the laser, meaning we set δ to be negative. We then separate the laser into three orthogonal pairs of counterpropagating beams, two along the x-axis, two along the y-axis, and two along the z-axis, as shown in Fig. 40.

An atom with a zero velocity is equally likely to interact with all six laser beams, and over time will experience a net force of zero. However, the atom we are discussing has an arbitrary velocity. As it moves towards one of the lasers it will see a blueshift from the Dopper effect, which counters the redshift from the laser detuning and increases the probability of interaction. Conversely, as it moves away from the laser, it will see an even greater redshift, further reducing the chance of interaction. The outcome is a system where an atom is more likely to scatter photons whose momentum opposes their motion. When applied to a gas, the spread of velocities is dramatically decreased and the temperature is cooled.

4.1.2 MAGNETO-OPTICAL TRAP

Atoms in an optical molasses are not confined. In fact they can and will random-walk out of the interaction region. If we selectively apply force not just based on velocity, but based on position as well, we may confine the atoms in addition to cooling them. When we do this by taking advantage of the Zeeman effect, the system becomes a MOT. Our starting point is the red-detuned laser system described in previous subsection, 4.1.1.

Let us consider a two-level atom where the ground state is J=0, and the excited state is J=1. The excited state has the following magnetic sub-levels: M=-1, M=0, M=1. In the presence of a low energy magnetic field, the degenerate sub-levels will shift their energies proportionally to the magnitude of the B-field. The Zeeman energy level shift is:

$$\Delta E = g\mu_B MB \tag{72}$$

where g is the Lande g-factor, M is the projection of the angular momentum along

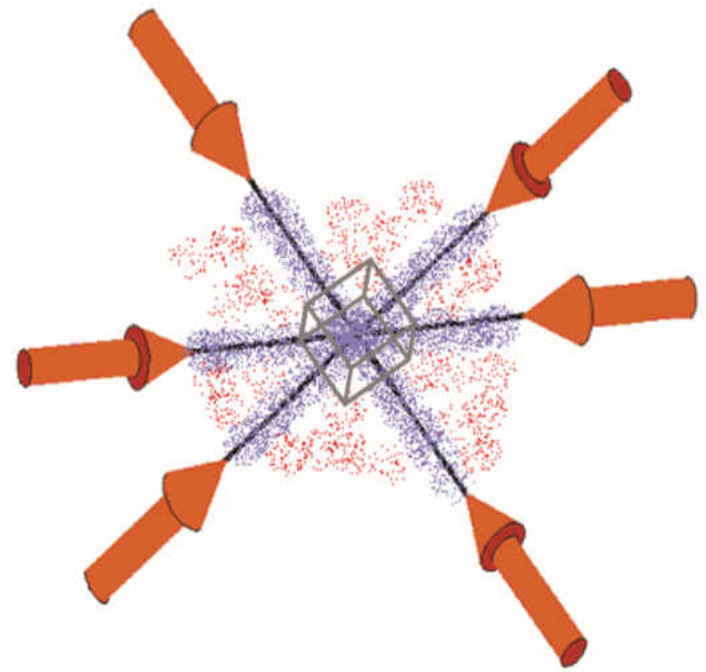

FIG. 40: A diagram showing the laser configuration required to form an optical molasses. Three pairs of orthogonal laser beams are shown. Atoms that interact with at least one beam are shown in blue, and atoms that do not interact with any beams are shown in red. The optical molasses forms in the center box, where all six beams are present. Figure credit: M. Shaffer [1].

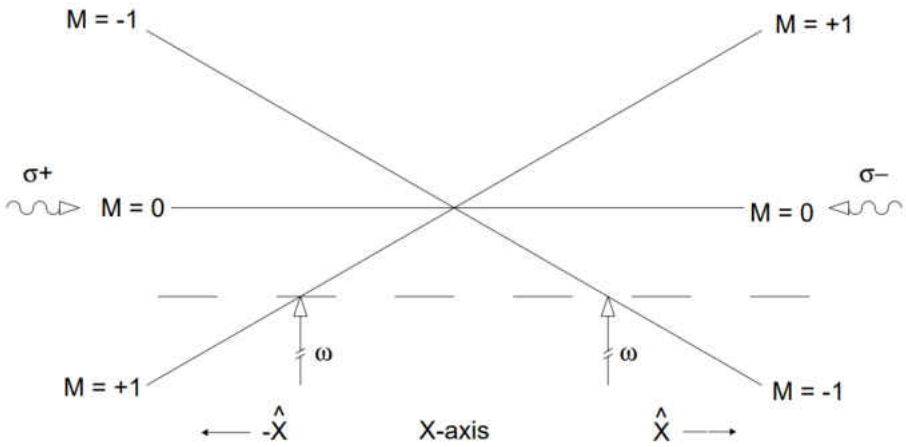

FIG. 41: The diagram shows the Zeeman energy shift as a function of displacement from center. There are two counterpropagating circularly polarized laser fields: σ^+ from the left, and σ^- from the right. We see that the σ^+ laser field is more likely to interact with the atom when the atom is displaced to the left of center. Similarly, the σ^- laser field is more likely to interact with the atom when it is displaced to the right of center.

B, and μ_B is the Bohr magneton and is given as $\mu_B = e\hbar/2m_e c$. With a quadrupole magnetic field we may generate a Zeeman shift in our atoms that is proportional to their displacement from center [34]. The magnetic fields cancel out at the center of the trap, but as an atom moves away it will experience an increasingly large B-field. The direction of the B-field is spatially dependent, and if the atom had moved in the opposite direction, it would have experienced a B-field with the same magnitude in the opposite direction. By correctly circularly polarizing the optical molasses trapping beams such that along each axis, one beam has σ^+ polarization and its opposing beam has σ^- polarization, we may confine the atoms.

Consider an atom moving along the x-axis shown in Fig. 41. If it initially has a velocity in the $+\hat{x}$-direction, it needs a momentum kick in the -$\hat{x}$-direction to stay confined. Fortunately, its M=-1 magnetic sub-level continues to shift closer to the laser energy as it moves, thereby increasing the chance that it will absorb a σ^- photon with momentum in the -$\hat{x}$-direction. At the same time, as the atom moves to the right, the M=+1 magnetic sub-level continues to shift away from the laser energy, further reducing the chance of interaction with a σ^+ photon propagating the

wrong way. Symmetrically, if the atom had been moving with an initial velocity in the -$\hat{x}$-direction, it would have experienced a greatly increased chance of interaction with σ^+ photons with momentum in the +$\hat{x}$-direction. The atom will experience the highest probability of interaction when the following condition is met:

$$\delta_{Total} = \delta_{laser} \mp \vec{k} \cdot \vec{v} \pm \mu' B(z)/\hbar = 0 \tag{73}$$

Each time an atom absorbs a photon, it experiences a momentum kick equal to $\hbar\vec{k}$ towards the center of confinement, and exciting it to a higher atomic orbital. When the atom spontaneously decays back into the ground state, it emits a photon in a random direction and experiences a recoil kick. Over the course of many cycles, the momentum kicks from the absorbed photons continue to add together, while the recoil kicks average out to zero. The net result is atoms that feel a force directing them back to the center of the magnetic field. However, these recoil kicks result in heating within the sample and limit the minimum temperature achievable simply with Doppler techniques. The Doppler cooling limit, T_D, is given as [46]

$$T_D = \frac{\hbar\Gamma}{2k_B} \tag{74}$$

The above technique may easily be scaled into three dimensions. The required magnetic field may be provided with a pair of coils in an anti-Helmholtz configuration. At their center, $B(x, y, z) = 0$, and at small displacements the B-field magnitude increases linearly. However, we should note that the gradient of the B-field in the z-direction is twice that in the x-and y-directions.

4.1.3 SUB-DOPPLER COOLING VIA THE SISYPHUS EFFECT

Temperatures lower than the Doppler cooling limit may be achieved within MOTs through polarization gradient cooling, also known as Sisyphus cooling. The concept was first described by Claude Cohen-Tannoudji in 1989 [46]. At the time, researchers were perplexed that they were achieving temperatures below the Doppler limit described in Eqn. 74. Cohen-Tannoudji realized that the simple J_g=0, J_e=1 model we used above was insufficient to fully describe what was occurring. We may achieve much better understanding if we consider an atom with a ground state J_g=1/2 and excited state J_e=3/2, shown in Fig. 42.

In addition to using more realistic atomic structure, we must consider some effects

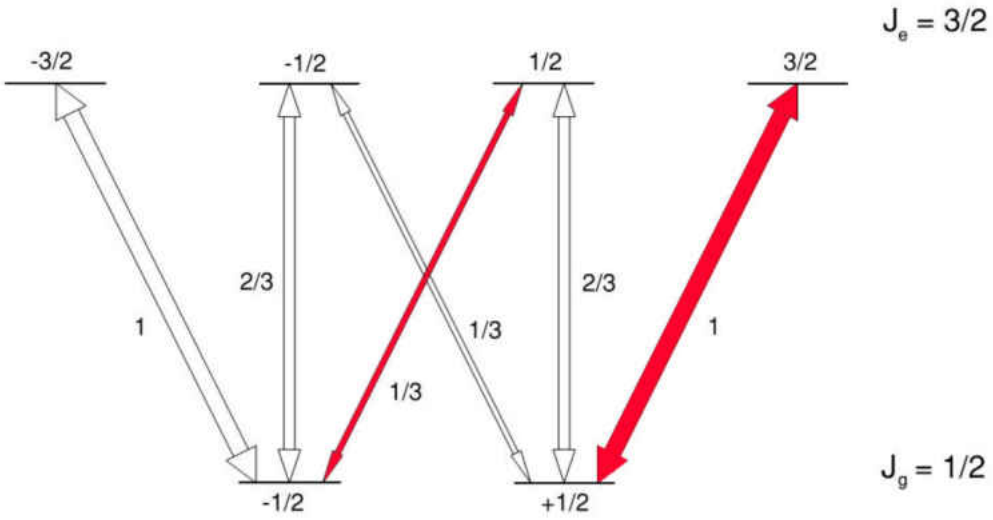

FIG. 42: A diagram showing the J_g=1/2 to J_e=3/2 system that we now use to understand Sisyphus cooling. Here the Clebsch-Gordan coefficients have been normalized in such a way that the strongest transitions have coefficients of 1. As an atom moves through the laser field, it will enter regions with different polarizations, therefore changing which transitions may be accessed. For example, when an atom is in a region where the polarization is σ^+, only the transitions shown in red will be accessible by the laser field.

that were ignored in our discussion of Doppler cooling. First, the trapping beams that form an optical molasses will create a polarization gradient within the region they overlap. They exist in three dimensions, and all six beams cannot possibly have parallel polarization. As a result, an atom propagating through this region will enter areas with net σ^+, σ^-, and linear polarization. Second, we consider the light shift due to the trapping beams. These shifts are proportional to the Rabi frequency squared.

$$\Delta E_e \propto \Omega^2 \tag{75}$$

$$\Delta E_g \propto -\Omega^2 \tag{76}$$

A key point here is that the stronger the transition strength, the larger the shift will be. As the atom propagates through the gradient polarization field, the polarization will change, as will the allowed transitions. The result is a spatially dependent light shift. Seen in Fig. 43, when the atom is located where the polarization is σ^+, the M_g=+1/2 sub-level is shifted further; however when the atom is located where the polarization is σ^-, the M_g=-1/2 sub-level is shifted further; and when the atom is located where the light is linearly polarized, the two sub-levels are shifted by the same amount. We may gain an understanding of the mechanism that drives Sisyphus cooling by considering these shifts only on the ground state, and ignoring the shifts in the excited states.

Finally we consider optical pumping. As the atom moves through the laser field, it will continuously be optically pumped back and forth between the two ground states. This occurs because when the atom is located where the laser field is σ^+ polarized, the only electronically allowed transitions are the two shown in red in Fig. 42. The M_g=-1/2 sub-level may excite to the J_e=1/2 excited state, which is likely to decay to the M_g=+1/2 ground state, but the M_g=+1/2 ground state may only be excited to the J_e=3/2 excited state, effectively trapping it there. We see a similar effect when the atom is in a σ^- portion of the laser field, resulting in pumping to the M_g=-1/2 ground state.

The net result is atoms that are optically pumped into one ground state with its own light shift, from where they are likely to be excited and may spontaneously decay back down the other ground state, which has an even larger light shift. As the atoms move from one polarization to the next, this process is repeated. The

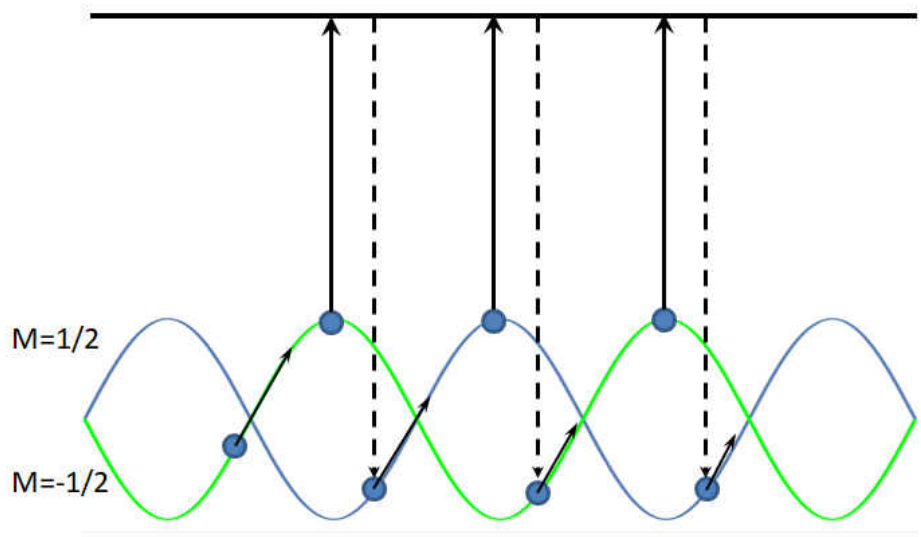

FIG. 43: The two sine waves show the energy level of the two ground states. As the atom moves through different polarizations, the light shift oscillates.

net result is, on average, atoms in the ensemble emit photons with slightly higher energies than the photons they absorb, converting a small portion of their kinetic energy into radiation with each cycle.

4.1.4 ATOM NUMBER WITHIN A MOT

A MOT does not form instantaneously. Under typical conditions, one might expect a MOT to fully load over several seconds. When a MOT is loading or at equilibrium, it is simultaneously trapping new atoms from the background vapor or beam and losing already trapped atoms due to collisions. The rate of change in atom number is described by

$$\frac{dN}{dt} = L - \alpha N(t) - \beta \int n(r,t)^2 \, d^3r \tag{77}$$

where L is the loading rate, α describes collisions with background gas, and β describes loss to inter-atom collisions within the MOT. As a large portion of these collisions are light-assisted, β itself is dependent on both laser detuning and intensity. The final atom number may be calculated by solving for the steady state solution to Eqn. 77.

Within a dual species MOT, another factor is added to Eqn. 77 representing the

trap loss due to interspecies collisions. Trap loss within a MOT made of "species A" while it is well overlapped with a MOT made of "species B" is taken into account in the last term of

$$\frac{dN_A}{dt} = L_A - \alpha_A N_A(t) - \beta_A \int n_A(r,t)^2 \, d^3r - \beta_{A,B} \int n_A(r,t)\, n_B(r,t)\, d^3r. \qquad (78)$$

4.1.5 ZEEMAN SLOWER THEORY

Atoms moving above a certain velocity, $\vec{v}_{max}$, will not be caught by a magneto-optical trap. A very good approximation of $\vec{v}_{max}$ can be made by treating the atoms ballistically. An atom crossing a resonant laser field will experience the following maximum opposing force:

$$\vec{F}_{max} = \hbar \vec{k} \frac{\Gamma}{2} \qquad (79)$$

If the atom crosses the laser beam without having come to a stop, it will not be caught. Assuming a constant force and therefore a constant acceleration, using Eqn. 79, Newton's Second Law, and kinematic equations of motion, we may arrive at the following maximum capture velocity:

$$v_{max} = \sqrt{(4\hbar w k \Gamma)/2m} \qquad (80)$$

where w is the laser waist and m is the atomic mass.

In reality, the scattering force is not constant. It changes both with location as the atom moves from one intensity to another, and with time as the atom slows down and experiences a Doppler shift. In addition, Eqn. 80 is valid only in the limit where $s/(s+1) \to 1$. However, it does serve as an excellent upper bound for $\vec{v}_{max}$. Table 2 shows us maximum possible capture velocities for rubidium, argon, and krypton for the commonly used 1-inch diameter beam. While these numbers may initially seem high, if we compare them to the distribution of atomic speeds at room temperature, we find an added complication.

$$f(v) = \left(\frac{2}{\pi}\right)^{1/2} \left(\frac{m}{k_B T}\right)^{3/2} e^{-(mv^2)/(2kT)} \qquad (81)$$

The distribution of speeds in three-dimensional gas is well described by a Maxwell-Boltzmann distribution, shown in Eqn. 81. In this expression k_B is the Boltzmann

Transition	Capture Velocity ($\frac{m}{s}$)	Most Probable $v(\frac{m}{s})$	Capture Efficiency
Rb	107	231	6.7%
Ar	143	336	5.2%
Kr	104	233	5.9%

TABLE 2: Table contains the maximum capture velocities, most probable velocities, and capture efficiencies for each of the three species used in this study.

constant, not to be confused with the wavenumber used above in Eqn. 79. In Fig. 44 we graph Eqn. 81 for each of the three elements used in this work. We clearly see that at room temperature, the majority of the atoms possess speeds well in excess of their respective $\vec{v}_{max}$. Integrating from 0 to $\vec{v}_{max}$ for each of our species yields capture rates that only range from 5% to 6%. The second and third columns of Table 2 provide the most probable speed, and the percentage of the distribution that falls within catchable limits, for rubidium, argon, and krypton. Even with these low limits, it is common to form a rubidium MOT without any 1D cooling, as all of the background vapor is available for trapping. This is not the case with noble gases. Our RF discharge only has a metastable efficiency of around 10^{-4}. This low production rate is further exasperated by the fact that once a metastable Ar or Kr atom collides with the chamber wall, it will quench back down to the ground state and is no longer available for trapping. With this limitation, we must slow down noble gas atoms entering the chamber if we wish to trap more than a handful at a time.

We rely on an apparatus called a Zeeman slower, which uses the scattering force and Zeeman effect to one-dimensionally cool our atoms. Initially, we have a collimated beam of atoms close to room temperature. We oppose it with a counter-propagating laser that has circular polarization and negative detuning. As a high velocity atom enters the slower, it encounters a magnetic field, which, in combination with the Doppler shift it observes, shifts the sub-level so that it is resonant with the laser. After absorbing a few photons, the atom's velocity will have decreased to the point where it is no longer resonant with the Zeeman slower laser. However, in that same time frame the atom's velocity will have carried it to a new location with a slightly lower magnetic field. The magnetic field may be tuned in such a way that as the atoms slow down they are continuously resonant with the slowing laser. Such

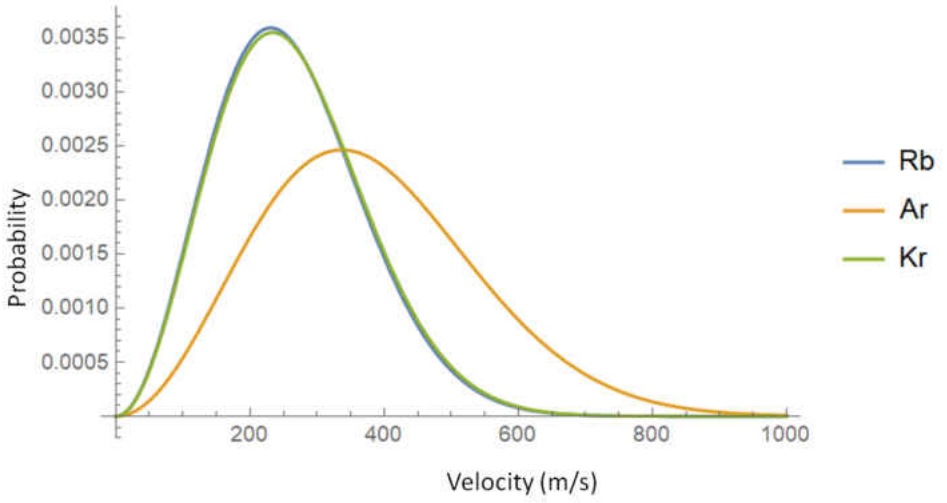

FIG. 44: A graph showing the velocity distributions of Rb, Ar, and Kr gas at room temperature. On average Ar has higher velocities due to its lower mass. Note that Rb and Kr are almost completely overlapped due to their similar masses.

a magnetic field will take the following form [35]:

$$B(z) = \frac{hv_o}{\lambda\mu_o}(1 - \frac{z}{L_o})^{1/2} + B_{bias} \tag{82}$$

4.1.6 REPUMPER TRANSITION

Due to its hyperfine structure, there is an added complication when trapping ^{85}Rb that does not occur in ^{40}Ar. The cycling transition between $5^2S_{1/2}$ F=3 ground state and $5^2P_{1/2}$ F′=4 excited state is driven on the order of a million times per second. However, due to the detuning required by Doppler cooling, with each cycle there exists a nonzero probability that we will inadvertently excite to the F′=3 excited state. From there, the system may decay down to the F=2 ground state and become inaccessible to our trapping laser. This occurs in 1 per 10^4 cycles, which while seemingly small, will quickly optically pump the entire population to F=2 and prevent further confinement. A second laser may be employed to excite the F=2 to F′=3 transition, and repopulate the F=3 ground state. This laser is often referred to as either a “hyperfine” or “repumper” laser.

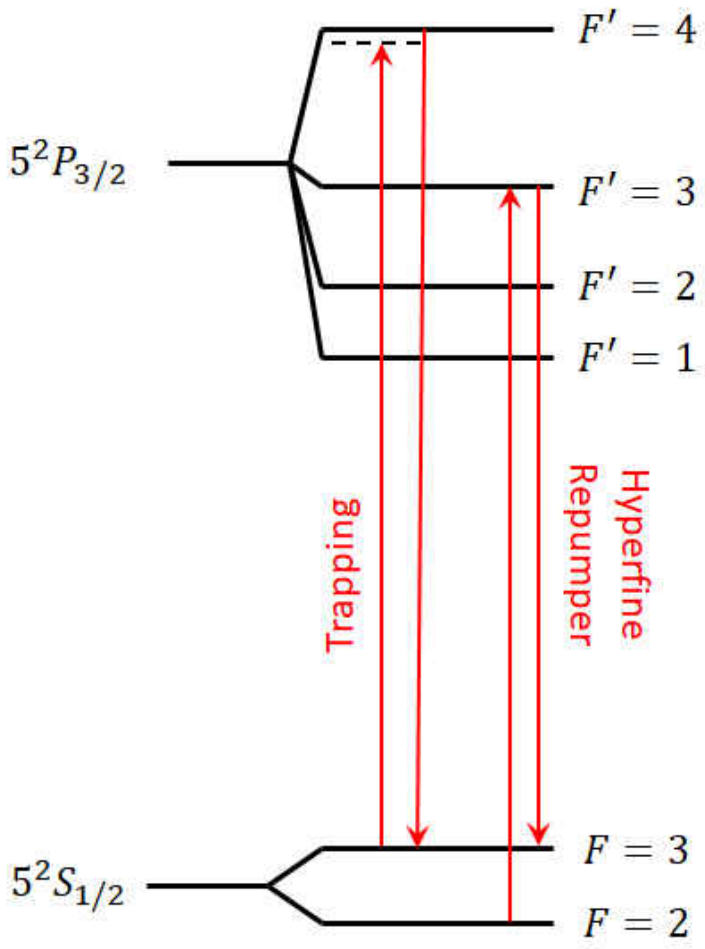

FIG. 45: A diagram showing the relevant atomic structure within ^{85}Rb.

4.2 MOLECULAR STRUCTURE AND INTERACTIONS

A diatomic molecule is formed when two atoms are bound together in an attractive or repulsive potential. Our study focuses on the long-range behavior of RbAr molecules, where van der Waals and dipole interactions provide these potentials. The atoms themselves spend most of their time at very large internuclear separations, where they cause only small perturbations in each other's electron clouds.

In the following discussions we will find that a semiclassical approach provides us with a great deal of insight into the structure that may be encountered when performing spectroscopy. We will start with the Schrodinger equation for a generic diatomic molecule. Using separation of variables, we will see that the electronic component may be isolated and solved repeatedly to yield the shape of molecular potentials. We will use a rigid rotor model to describe the separation in energy levels from rotational energy eigenvalues and the parabolic harmonic oscillator as an approximation with which to shed more light on the vibrational energy levels. These discussions will closely follow ones by Hooker and Webb in Ref. [42] and W. Demtroder found in Ref. [47].

4.2.1 BORN OPPENHEIMER APPROXIMATION

The Schrodinger equation for a generic diatomic molecule is

$$(T_e + T_N + V(\mathbf{R}, \mathbf{r}))\Psi = E\Psi \tag{83}$$

where T_N is the sum of the nuclear kinetic energy operators, T_e is the sum of the electronic kinetic energy operators, and V($\mathbf{R}, \mathbf{r}$) is the sum of the Coloumb potential energies. Here we write $\mathbf{r}$ in bold to symbolize the location of all of the electrons, $\mathbf{r} \equiv r_1, r_2, ..., r_i$, and $\mathbf{R}$ in bold to symbolize the location of both nuclei, $\mathbf{R} \equiv R_1, R_2$, while we use R to represent the internuclear separation.

$$T_e = -\frac{\hbar^2}{2m}\sum_i \bigtriangledown_n^2 \tag{84}$$

$$T_N = -\hbar^2(\frac{\bigtriangledown_A^2}{2M_A} + \frac{\bigtriangledown_B^2}{2M_B}) \tag{85}$$

$$V(\mathbf{R}, \mathbf{r}) = -\sum_{n=A,B}\sum_i \frac{Z_n e^2}{4\pi\epsilon_o \mid r_i - r_n \mid} + \sum_{i>j}\frac{e^2}{4\pi\epsilon_o \mid r_i - r_j \mid} + \frac{Z_A Z_B e^2}{4\pi\epsilon_o R} \tag{86}$$

In this expression of $V(\mathbf{R}, \mathbf{r})$, the first term is an attractive potential caused by the interaction of the electrons with the two nuclei, the second term is the repulsive potential caused from repulsion between the individual electrons, and the final term is a repulsive potential caused by the interaction between the two nuclei.

Using the Born-Oppenheimer approximation, we note that due to mass differences between the electrons and nuclei, change in the internuclear separation is negligible over the timescales associated with electronic transitions. We may separate the electronic wavefunction from the nuclear.

$$\Psi(\mathbf{R}, \mathbf{r}) = \Psi_e(\mathbf{R}, \mathbf{r})\Psi_N(\mathbf{R}) \tag{87}$$

which yields separate Schrodinger equations for the electrons, shown in Eqn. 88, and for the nuclei, shown in Eqn. 89.

$$(T_e + V(\mathbf{R}, \mathbf{r}))\Psi_e(\mathbf{R,r}) = U(\mathbf{R})\Psi_e(\mathbf{R}) \tag{88}$$

Repeatedly solving Eqn. 88 for many different fixed values of R allows us to map out the effective potential through which the nuclei move, $U(\mathbf{R})$, which we then use in the nuclear Schrodinger equation:

$$(T_N + U(\mathbf{R}))\Psi_N(\mathbf{R}) = E\Psi_N(\mathbf{R}) \tag{89}$$

where E is the total molecular energy. When solving the Schrodinger equation for the nuclear wavefunction, it is helpful to view the system with a reduced mass, treating it as if it were a single particle moving within a central potential $U(R)$. In spherical coordinates, we may separate the rotational motion from the radial motion, as shown:

$$\Psi_N = \frac{1}{R}\Psi_v(R)\Psi r(\theta, \phi) \tag{90}$$

where $\Psi_v(R)$ is a vibrational wavefunction and depends on the internuclear separation, while $\Psi_r(\theta, \phi)$ is a rotational wavefunction and depends on the rotation of the internuclear axis. We may independently solve for the vibrational and the rotational eigenvalues.

4.2.2 MOLECULAR ROTATIONAL AND VIBRATIONAL ENERGIES

As mentioned above, the allowed rotational energies are quantized. Picture both atoms rotating around an axis through their center of mass. Classically, their moment

of inertia is MR^2, where M is the reduced mass, $M = (M_A M_B)/(M_A + M_B)$, and R is the internuclear separation, which for the moment we will assume is fixed. The system's rotational kinetic energy may be described by the very familiar $E_{rot} = \frac{1}{2}I\omega^2$, which may also be expressed in terms of angular momentum, $E_{rot} = (J^2)/(2I)$, where J is the total angular momentum. Since $J^2 = J(J+1)\hbar^2$, merging these relationships we find

$$E_{rot} = \frac{1}{2}I\omega^2 = \frac{J^2}{2I} = \frac{J(J+1)\hbar^2}{2MR^2} \tag{91}$$

Examining the energy spacing between adjacent different rotational levels, we see that the spacing increases linearly with J:

$$\Delta E_{rot} = E_{rot}(J+1) - E_{rot}(J) = \frac{(J+1)\hbar^2}{2MR^2} \tag{92}$$

However, real molecules do not have their internuclear distance rigidly fixed. As atoms rotate about their center of mass at higher values of J, their separation widens and they experience a stronger restoring force. The effects result in a small distortion of energy levels that we neglect here.

We have just considered a rigid rotating molecule that has its internuclear separation fixed. Now, we shall consider the opposite. Let us assume that the previously spinning molecule is now non-rotating, and that its atoms are allowed to freely vibrate along its internuclear axis. The bound molecular potentials that our atoms move through are anharmonic; however, at small internuclear separations they may be closely approximated via a parabolic harmonic oscillator. This assumption breaks down as the molecules move further from their minimum potential energy, but it still serves to illustrate a few points. The energy levels of the harmonic oscillator are given by

$$E_v(v) = (v + \frac{1}{2})h\omega \tag{93}$$

where v is the integer vibrational quantum number, and $\omega = \sqrt{k_r/M}$. Of note is that at the lowest vibrational energy level, where $v = 0$, the energy is *not* zero but is instead equal to $\frac{1}{2}h\omega$. We should point out that while in the case of the parabolic harmonic oscillator, the energy levels are separated evenly by $h\omega$, in a more realistic system, we would expect the energy spacing between the vibrational states to decrease as v increases.

4.2.3 FRANCK-CONDON FACTORS

Three separate factors determine the intensities of vibrational bands: 1) the strength of the electronic transition, 2) the populations of the vibrational levels, and 3) the Franck-Condon overlap factor. James Franck argued that similar to the Born-Oppenheimer approximation, the time interval associated with an electronic transition is short when compared to the vibrational period of a molecule allowing us to separate electronic and vibrational motion. He also noted that transition is most likely to occur along the outer edges of the potential well, which if thought of in a classical frame, is where we would have expected the particles to spend the most time. Two years later a quantum mechanical explanation was provided by Edward Condon, who showed that the intensity of a vibronic transition is proportional to the dipole moment squared, and the overlap of vibrational states.

$$I \propto |R_e|^2 f_{v'v''} \tag{94}$$

where I is the intensiy, R_e is the dipole moment, and $f_{v'v''}$ is called the Franck-Condon factor and measures the overlap of the ground state and excited state vibrational wavefunctions [48].

$$f_{v'v''} = \int \Psi^*_{v'} \Psi_{v''} dR \tag{95}$$

4.2.4 LONG-RANGE INTERACTIONS

In the long range states that we are investigating, interactions between heteronuclear atoms, or ground state homonuclear atoms, are governed by the van der Waals interaction, in which two atoms induce dipoles in one another:

$$V(R) = -\frac{C_6}{R^6} - \frac{C_8}{R^8} - \frac{C_{10}}{R^{10}} - ... \tag{96}$$

where C_n are dispersion coefficients that must be calcuated for each molecular state [49]. The C_6 term is the dominant term in the case of heteronuclear potentials. For a simple nondegenerate system, C_6 may be represented in the form:

$$C_6 = \sum_{n_a n_b} \frac{2|\langle \Psi_{o_a} || \sum_i r_i C^1(\hat{r}_i) || \Psi_{n_a} \rangle|^2}{3} \times \frac{|\langle \Psi_{o_b} || \sum_j r_j C^1(\hat{r}_j) || \Psi_{n_b} \rangle|^2}{E_{n_a} + E_{n_b} - E_{o_a} - E_{o_b}} \tag{97}$$

where $C^1(\hat{r})$ is the spherical tensor of rank 1, Ψ_{o_a} and Ψ_{n_a} are the wave function of the initial state and the n_ath intermediate eigenfunction for atom A, E_{o_a} and E_{n_a} are their corresponding energies, the sum i runs over all the electrons in atom A, and the terms Ψ_{o_b}, Ψ_{n_b}, E_{o_b}, E_{n_b}, and j are to atom B what their counterpart symbols are to atom A [50]. For a more complex degenerate system, degenerate perturbation theory must be used. In practice, these involve summing over many states, and are not trivial.

Dispersion coefficients have been calculated for a large number of heteronuclear and homonuclear alkali-metal systems. In systems more closely related to our own, they have been found for helium and alkali-metal atoms [50], and in S + P potentials for heavy noble gases [51]. However, to the best of our knowledge, dispersion coefficients have not been calculated for a heteronuclear system consisting of an alkali metal and a heavy rare gas in the metastable state. It is important to note that in the case of KRb molecules, the C_6 was considerably larger for excited collisions than for ground state collisions [52]. This is due to the fact that the first excited states in K and Rb are very close energetically. This is also that case in our system. We will come back to this point later.

A more general version of Eqn. 96 may be written by including the dissociation limit, and allowing for n to be smaller than 6. Typically, the leading nonzero term is a good approximation of the interaction. We now approximate the long-range molecular potentials as:

$$V(R) = D_e - \sum_n \frac{C_n}{R^n} \tag{98}$$

where D_e is the dissociation limit, and n is related to the nature of the two atoms forming the molecule. Each of the following conditions has a different n value:

- $n = 1$ is for a Coulomb potential interaction between two charged atoms
- $n = 2$ is for an interaction between one charged atom and a permanent electric dipole in another
- $n = 3$ is for a dipole interaction between two atoms with permanent dipole moments
- $n = 4$ is for an interaction between a neutral atom and an ion

- $n = 5$ is for quadrupole-quadrupole interactions between neutral atoms with nonzero angular momentum
- $n = 6$ is for van der Waals interactions between two induced dipoles.

In addition to determining the shape of the overall potentials, once C_6 coefficients have been calculated, we may estimate the vibrational energies E_v, that correspond to specific vibrational quantum numbers v, with the LeRoy-Bernstein formula:

$$E_v = D_e - \left[(v_D - v) \times \left(\sqrt{\frac{\pi}{2\mu}} \frac{\Gamma(1+1/n)}{\Gamma(1/2+1/n)} \frac{\hbar(n-2)}{(-C_n)^{1/n}}\right)\right]^{2n/n-2} \tag{99}$$

where v_D is the value of v at the dissociation energy D_e, μ is the reduced mass, and Γ a Gamma function [53]. This is a useful tool to identify the individual peaks encountered in photoassociative spectra.

4.3 PHOTOASSOCIATION

Photoassociation (PA) is the process by which two colliding atoms are excited into a bound molecular state by a resonant photon. For the excitation to take place, the sum of the initial atomic kinetic energies plus the energy of the absorbed photon must equal the energy of the bound molecular state.

$$A + B + \gamma \rightarrow (AB)^* \tag{100}$$

4.4 IONIZATION PATHWAYS

When a metastable atom with excitation energy E* collides with another atom whose ionization energy is lower than E*, a process known as Penning ionization may occur [54]. During the collision, part of the excitation energy may be transferred and ionize one of the atoms. The system may nonradiatively decay onto a repulsive molecular curve, resulting in a ground state atom, an ion, and a free electron. This process only occurs at small internuclear separations, where the molecular potential is deeper and quantum chemistry is required to describe the system.

$$Ar^* + Rb \rightarrow Ar + Rb^+ + e^- \tag{101}$$

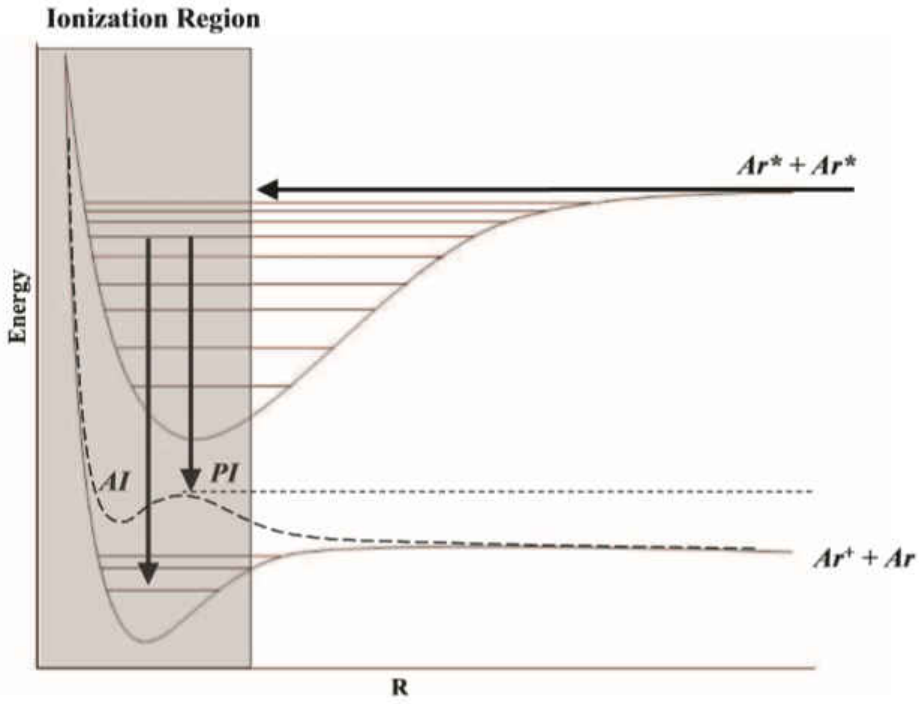

FIG. 46: A figure showing both PI and AI decay channels within a homonuclear Ar^* system. Figure credit: M. Shaffer.

In a process very similar to Penning ionization, the two colliding atoms may eject an electron and decay into a bound molecular state with a net positive charge. This is referred to as associative ionization.

$$Ar^* + Rb \rightarrow (ArRb)^+ + e^- \tag{102}$$

Both of these processes, shown in Fig. 46 may also occur with two metastable atoms, so long as the combined excitation energy is high enough to ionize one of them. Previous work by H. Busch [2] used a mass spectrometer to differentiate between the two ionization pathways shown in Eqns. 101 and 102, and determined that within an Ar^* MOT, Penning ionization was dominant by about a factor of 6.

4.4.1 DETECTION OF PA

Several methods to detect photoassociative excitation of molecules have been developed, including trap loss measurements [55], relying on Penning and associative ionization (PI and AI) [56], and using an additional laser to ionize excited state

molecules [57]. In our work, we rely on the first two methods mentioned, trap loss measurements and detection of PI and AI. We start this conversation by discussing how these mechanisms allow us to detect PA within a metastable Ar MOT. We then discuss what we expect to change in the heteronuclear system of Rb + Ar*.

At long ranges, two Ar* experience a van der Waals potential that varies with internuclear separation in the form C_6/R^6. Within a MOT, there will be atom pairs with a distribution of internuclear separations. At very large separations, the C_6/R^6 shaped potential is effectively flat [34]. But at shorter separations, the potential will accelerate the two atoms towards each other. During collisions, the quasi-molecule may decay nonradiatively via PI or AI, as described in Eqns. 101 and 102. Even with no laser field present, a small but steady stream of ions may be detected from an Ar* MOT. This increases when the trapping beams are turned on, exciting a portion of the atoms to a P-orbital.

When a resonant photoassociation laser is scanned across the system, atom pairs are elevated into an excited molecular state. At long range, two homonuclear atoms experience a dipole potential with the shape C_3/R^3. The attractive range of this curve is much larger than that of the ground state C_6/R^6 curve, and atom pairs will be accelerated towards each other at larger separations. As a result, when the PA laser is tuned such that it is resonantly producing excited molecular states, more atom pairs will collide and an increase in ion production may be detected.

Excited state molecules are not limited to PI and AI as decay mechanisms. They may spontaneously radiatively decay into a ground state, resulting in either a bound ground state molecule, or two hot atoms with enough kinetic energy to escape the MOT. When this occurs, it is referred to as "radiative escape." Unlike PI and AI, radiative escape may also transpire at large internuclear separations, as long as the Franck-Condon factor is favorable. Radiative escape may be detected as a decrease in fluorescence from the MOT.

Our discussion now moves onto our current experiment, photoassociation spectroscopy of RbAr molecules. Like the homonuclear Ar* system we just discussed, at long ranges, a Rb + Ar* system has a molecular potential with the form C_6'/R^6. Here the prime denotes the fact that the dispersion coefficient is different than it was for the Ar* + Ar* system. In previous work, H. Busch et al. detected PI and AI due to collisions between Rb and Ar*, suggesting that we may rely on PI and AI again in this experiment.

The excited state potential for a heteronuclear system has the form C_6''/R^6, where the double prime denotes that the excited state dispersion coefficient is different from that of the ground state. With different coefficients, the potential curve must have a different shape from the ground state, and should result in a change in the rate of collisions. Again, from previous work we already know that PI and AI are happening within the system, and so we expect Rb + Ar^* to register as a change in the rate of ion production when the PA laser is tuned correctly. Additionally, as mentioned in Section 4.2.4, the small energy difference between the lowest excited states of our atoms suggests that C_6'' is likely to be much larger than C_6', making any change in ion production easier to detect. Finally, trap loss is still available as a detection mechanism. As a second detection method, we may monitor the MOT's fluorescence, looking for dips as the PA laser scans. In this way, we hope to map out the excited molecular structure.

In summary, our experiment will look for the two following signatures of photoassociation: 1) a change in ion production, and 2) trap loss witnessed in fluorescence measurements.

CHAPTER 5

PHOTOASSOCIATION EXPERIMENTAL APPARATUS AND TECHNIQUES

The ultimate goal of this study is to slowly scan the PA laser through well overlapped dual species Ar* and Rb MOTs, and look for signatures of PA and molecular structure as a function of PA laser tuning. We have chosen to focus our search below the Ar* $4p[5/2]_3$ + Rb $5^2S_{1/2}$ asymptote. From previous work [1], we know that homonuclear Ar* PA features exist within our search range, so we must also perform a second scan of only Ar* PA. After careful analysis, features that appear in the difference between the two scans may be attributed to excited state RbAr molecular production.

In order to conduct these experiments, we have very specific demands of our laboratory equipment. PA requires colliding atoms in the presence of a laser field. We have chosen to perform this study using magneto-optical trapping as a way to increase density and improve the collision rate, thus increasing the PA production rate. To form a MOT, we require a vacuum chamber maintained at very low pressures and a separate system of laser beams for each species. To deliver meaningful spectroscopic data, we need a narrow, tunable PA laser to scan. Lastly, we need equipment to search for signs of photoassociation.

This chapter discusses all of the equipment we use. We start by describing the laser systems. We then discuss the vacuum systems and magnetic fields together. In the last section we discuss the detection methods we use and the calibrations associated with them.

5.1 LASER SYSTEMS

We have the same high precision, low bandwidth needs in this study as we had in our krypton work. We find many of the same tools to be invaluable. Again, we make extensive use of external cavity diode lasers (ECDLs), saturated absorption spectroscopy (SAS), and phase-sensitive detection. These techniques are described

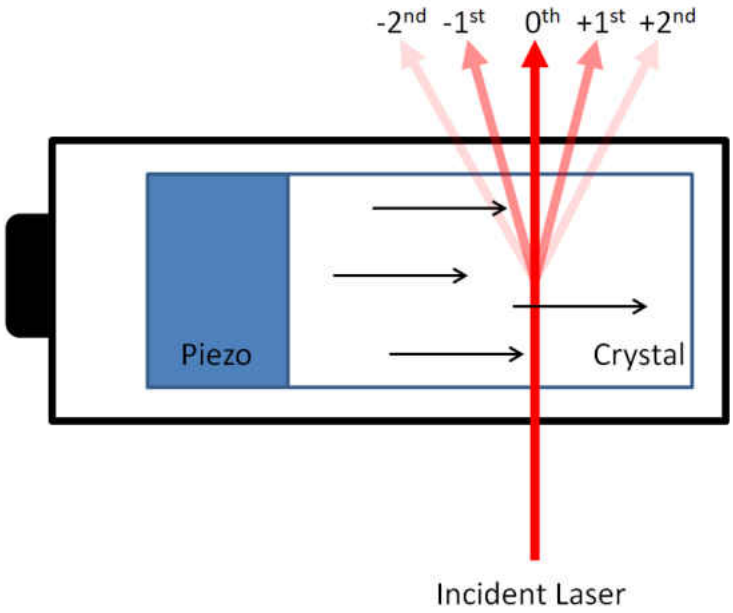

FIG. 47: A cartoon of how an AOM works. The piezo, on the left vibrates and sends phonons (in black) to the right. The higher orders become fainter because they require more photon/phonon collisions.

in Subsections 3.2.1, 3.2.2, and 3.2.4, respectively. In this section we will describe acousto-optic modulators, as well as describe our laser systems in depth.

5.1.1 ACOUSTO-OPTIC MODULATOR

An acousto-optic modulator (AOM) is a device used to shift both the frequency and angle of an incident laser beam. AOMs are made up of a crystal with a piezoelectric transducer attached to one end, as shown in Fig. 47. An RF voltage is applied to the piezo, causing phonons to propagate through the crystal perpendicular to the incident laser beam. The phonons may collide with the photons, transferring momentum in discrete amounts and resulting in multiple beam orders coming out of the crystal. The RF signal is supplied by a voltage-controlled oscillator (VCO). The laser shift frequency and output angle may be tuned by adjusting the VCO. Using AOMs in our system delivers two key capabilities. First, they allow us to tune lasers with a high precision within 100's of kHz. Second, they allow us to switch on and off a laser beam in a few μs or less, which is far quicker than a mechanical shutter.

We may lock our lasers to an atomic transition using SAS and phase-sensitive

detection. However, Doppler cooling demands that our lasers be detuned slightly beneath the transition frequency. We use AOMs to provide these small shifts. Our VCOs (Mini-Circuits ZOS-100) have a frequency range of 50 MHz to 100 MHz, and by themselves are unable to provide the small detunings we need to trap atoms. However we may circumvent this limitation by using pairs of AOMs. Using one to shift a master laser in the negative direction, and a second AOM to shift an injection locked slave laser back in the positive direction, we may detune by as little as 100 kHz if we so desire. For example, if we wanted an offset of -10 MHz:

$$\delta = \Delta f_1 - \Delta f_2 = -70\,\mathrm{MHz} + 60\,\mathrm{MHz} = -10\,\mathrm{MHz} \tag{103}$$

To use an AOM as a fast shutter, we insert a (Mini-Circuits ZYSWA-2-50DR) switch as shown in the first part of Fig. 48. A TTL signal from a pulse generator allows us to switch the 1^{st} order output on and off as necessary. When cycling at frequencies in the range of 100's of Hz or higher, we find the AOM achieves thermal equilibrium and we may expect rise and fall times of a few μs. However, occasionally we require much longer duty cycles. During the second PA experiment, Section 6.2.1, we required a very slow duty cycle around 0.05 Hz. The 10-second gaps without RF power being delivered to the AOM were long enough for thermal shifts in the AOM crystal, which in turn may cause beam displacement and lower our overall efficiency. Thermal lag lengthened our rise times from a few μs to an unacceptable 4 seconds.

To counter the thermal swings, we employed a technique similar to that described in Ref. [58]. The root of the problem is that extended periods of time with no RF power gives the AOM crystal time to cool. We employ a second VCO, and use a switch to send its output to the AOM during "off-time," as shown in Fig. 48. The secondary VCO may be tuned to a different frequency than the primary VCO, so the 1^{st} order output will no longer be correctly phase matched when the secondary VCO is driving the AOM. While detuning the secondary VCO, we found if we moved it more than 10 MHz from the primary VCO tuning that the thermal lag would start to reappear. Conversely, if it was too close to the primary VCO's tuning, the AOM output would not be fully attenuated. Figure 49 shows the results from our calibrations, where we examined ideal secondary VCO tunings. We settled at +6 MHz.

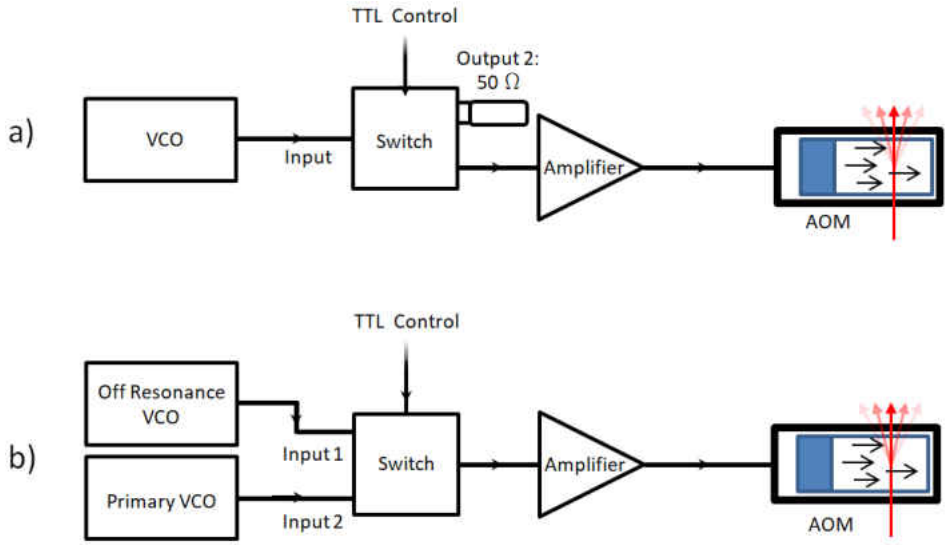

FIG. 48: A diagram of the electronics used in our AOM circuits. Part a) is our standard design, and Part b) is the design used for long duty cycles with a second VCO to maintain power going to the AOM.

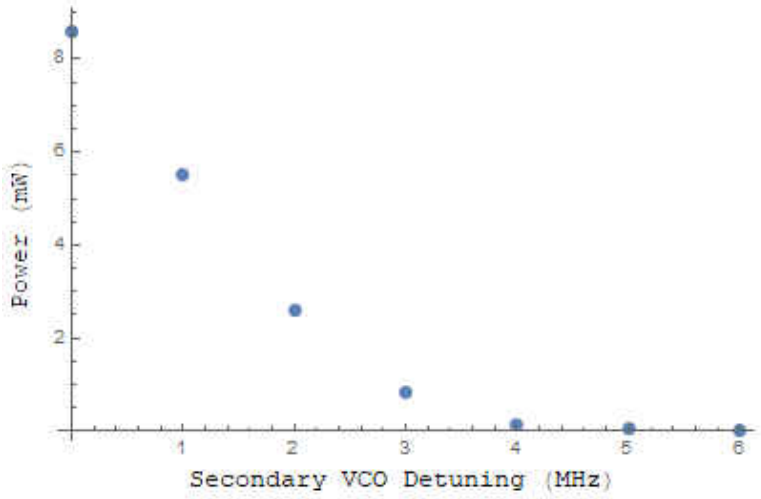

FIG. 49: A graph showing laser power out vs. frequency of the second VCO in place to counter thermal lag. When the two VCOs have the same tuning, there is no difference in the AOM output as the switch flips between the two. As the secondary VCO is tuned away, the light making it to the experiment decreases. We found that we needed to tune the secondary VCO at least 6 MHz away for the trap light to be extinguished.

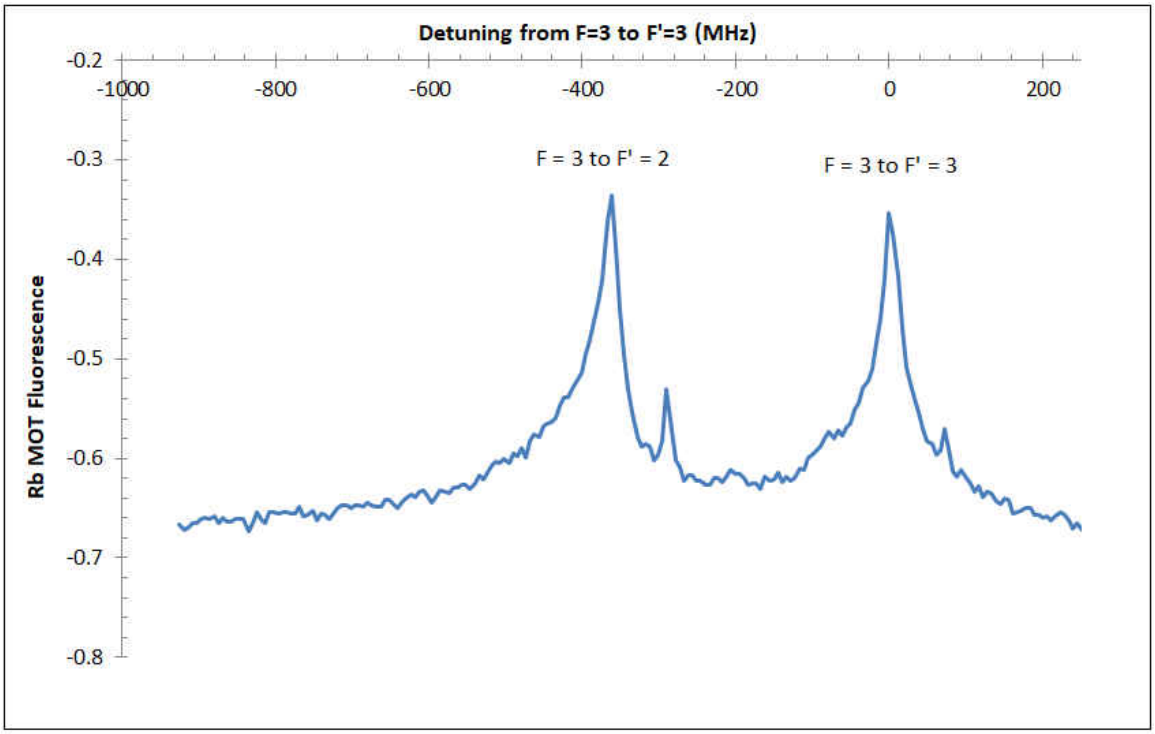

FIG. 50: A plot showing fluorescence measurements from the Rb MOT as the PA laser scans across two transitions. The two smaller peaks are the result of light leakage from the AOM 0^{th} order on top of the AOM 1^{st} order.

5.1.2 ACOUSTO-OPTIC MODULATOR 0TH ORDER

As described in Section 5.1.1, we use an AOM to quickly shutter the PA laser beam. While performing diagnostics on our PMT, we discovered that a very small portion of the AOM's 0th order had been leaking into its 1st order. While scanning across both of the $5^2S_{1/2}$ F=3 to $5^2P_{1/2}$ F′=2, and $5^2S_{1/2}$ F=3 to $5^2P_{1/2}$ F′=3 transitions, we found a second set of small duplicate peaks that should not have been there. Each peak appeared at a detuning of +72 MHz from its corresponding hyperfine peak. This matches perfectly with the PA AOM, where we shift the 1st order by +72 MHz.

Initially it was not clear whether some of the 0th order photons were reflecting into the 1st order internally in the AOM crystal, or if a small portion of the 0th beam was scattering into the fiber launcher further downstream. To test this, we completely blocked the 0th order while it was close to the AOM. However, in the subsequent scans the secondary peaks continued to appear leading us to believe the

photons were scattering internally. To measure the size, we picked off a portion of the PA beam from after the AOM and sent it into a spectrum analyzer, but were unable to detect any sign of the 0th order bleed-through. It is so small that we were unable to detect it anywhere except for its effect on the Rb MOT. We suspect that 0th order bleed-through also occurred while taking the 811 nm scans. If present, bleed-through would manifest itself as an additional smaller duplicate feature +72 MHz away from any real features found.

5.1.3 Rb LASERS

To form a Rb MOT, we require 5 mW to 10 mW of 780.027 nm laser light locked to the $5^2S_{1/2}$ F=3 $\rightarrow$ $5^2P_{3/2}$ F′=4 transition, and a few μW tuned to the F=2 $\rightarrow$ F′=3 repump transition. We use a homemade Littman-Metcalf configured ECDL cavity with a Sanyo DL-7140-201S diode and a 1200 groove/mm optical diffraction grating for tuning. The laser is housed in an aluminum enclosure, and temperature stabilized with a thermal electric cooler mounted to a large heat sink. The laser has a bandwidth of less than 1 MHz, and an output power of 25 mW. Of this, 2 mW is sent through a Rb vapor cell for saturated absorption spectroscopy. A further 2 mW is coupled into a fiber optical cable, and is available for input into a wavemeter. 750 μW is used to injection lock a slave laser to the correct frequency. The remainder is lost to inefficiencies in optical isolators and other optics. The slave laser is also supplied by a Sanyo DL-7140-201S diode, and like the master laser, it is housed in an aluminum case and temperature controlled. It has an output power of around 50 mW. The slave laser light is sent through an AOM for shuttering and to provide a small frequency shift. The master laser is locked to the F=3/F=4 crossover peak, -92 MHz from the F′=4 peak, and the AOM shifts the 1st order by +85 MHz for a total detuning of about 1.5 Γ. The beam continues on to a single mode fiber, where it is coupled and sent across the room to the experimental apparatus. A more detailed description of the 780 nm optical system can be seen in Fig. 51.

At the science chamber, the coupled light is launched out of the other end of the fiber and collimated with a f=15.29 mm lens. A $\lambda/4$-waveplate cleans up birefringence from the fiber and a $\lambda/2$-waveplate gives the laser the correct polarization to pass through the polarizing beamsplitter that combines the 780 nm Rb MOT light with the 811 nm for the Ar* MOT. From here, both beams are expanded to a 17.9 mm diameter, circularly polarized, and broken into six orthogonal beams to form a MOT

at the chamber center.

Over time the MOT trapping beams will optically pump the Rb atoms from the F=3 ground state to the F=2 ground state. Typically a second laser pumps out of the F=2 dark state. To avoid the added complication of a repump laser, we use a (HP VTO-8240) varactor-tuned oscillator to modulate the diode current and place sidebands on the slave laser. By tuning to 2.92 GHz, the sidebands effectively act as a repumper laser.

5.1.4 Ar LASERS

To form the Ar* MOT, we require a minimum of 20 mW of power in the trapping beams, and another 20 mW of power in the Zeeman slower. A repumper is not necessary because there is no hyperfine structure for even isotopes. Similar to the rubidium lasers, we use a system with a homemade Littman-Metcalf ECDL master laser and injection locked slave lasers to increase power. The master laser has a TEC temperature stabilized Sanyo DL-8031-031A diode. The external cavity has a 1200 grooves/mm grating mounted onto a Thorlabs mirror mount. A piezo is inserted into the mount, so that the angle of the mirror can be changed for frequency tuning. The master laser has a power output of around 60 mW after the optical isolators. Approximately 20 mW of its power used to injection lock each of the two separate slave lasers. We control the amount of power with two half-waveplates and two polarizing beamsplitter cubes. The remainder of the light is sent through an NEC C8217A AOM, from where the first order is coupled into an optical fiber. The output of the fiber is about 300 μW, is launched through the RF discharge described in section 5.2.1, and is used for saturated absorption spectroscopy.

Two slave lasers are injection locked to the master laser. Both are temperature stabilized with a TEC, but contrary to lasers previously described, there is no selection grating. The slave lasers have outputs of about 100 mW, and are each sent through another NEC C8217A AOM to tune and shutter. The trapping laser AOM is tuned to +64 MHz and the Zeeman slower AOM is tuned -81 MHz. The 0th orders from each AOM are fiber coupled to a Fabry-Perot cavity to monitor the quality of the injection lock. The +1st order of the trapping AOM is coupled into a fiber, and sent to the science chamber. The -1st order of the Zeeman slower AOM is sent to the apparatus through free space instead of a fiber in order to get the maximum power.

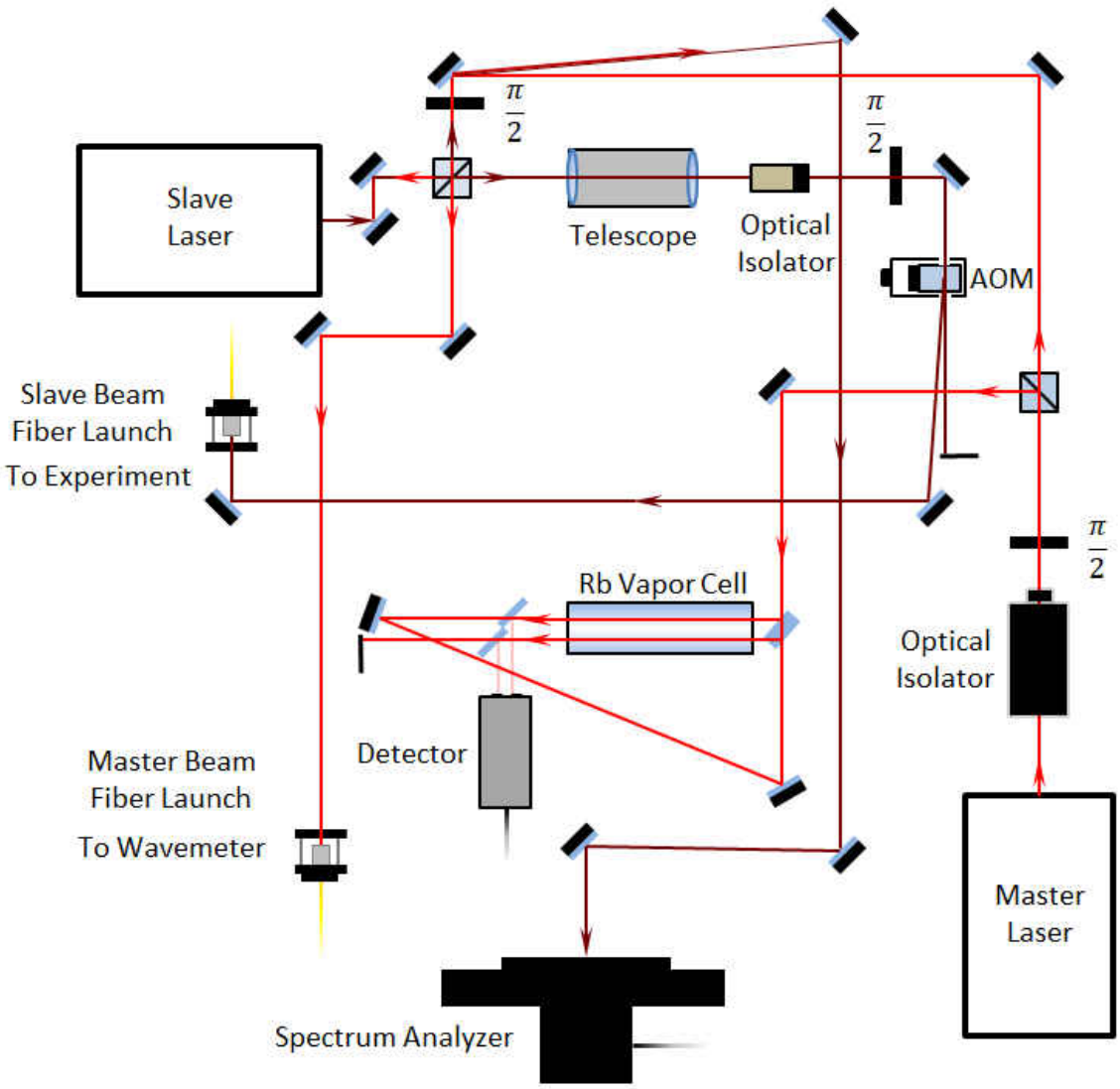

FIG. 51: A diagram representing the optical train for the rubidium lasers. The master laser is shown in bright red, and the slave laser is shown in dark red.

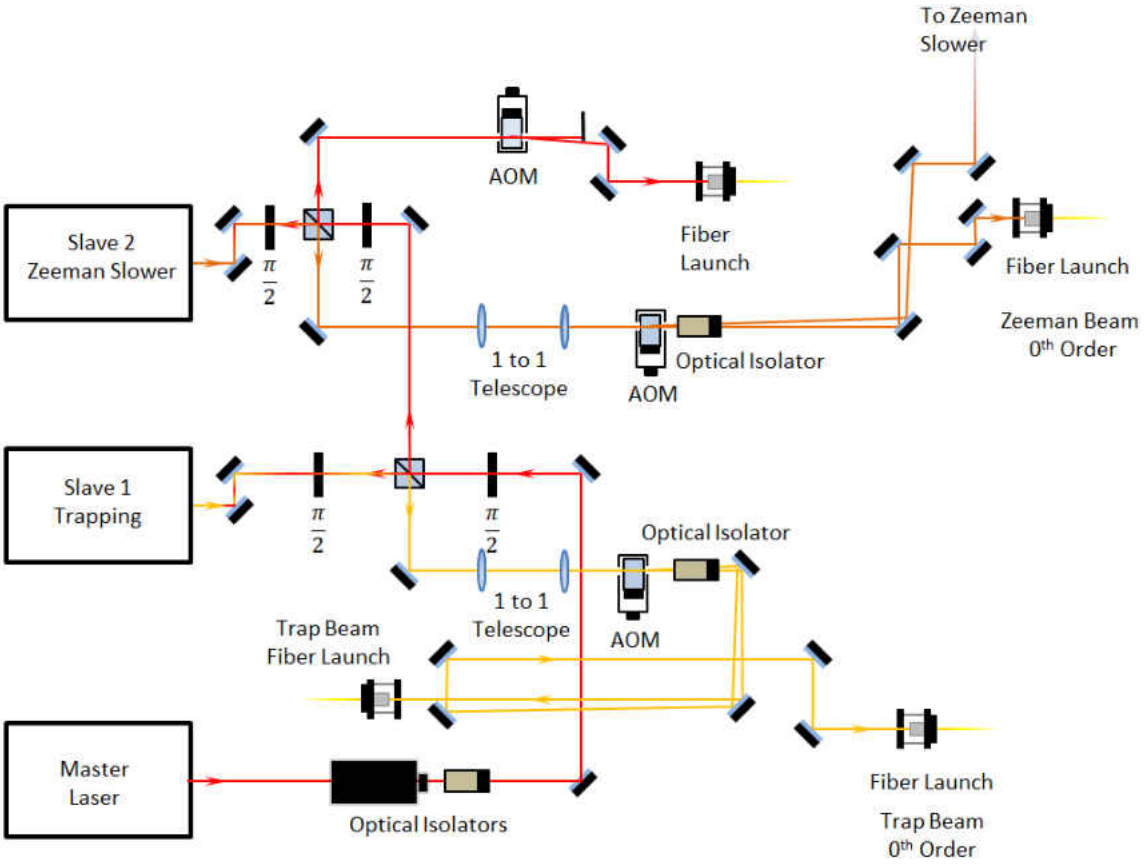

FIG. 52: A diagram representing the optical train for the argon lasers. The master laser is shown in bright red, the trapping slave laser is shown in yellow, and the Zeeman slave laser is shown in orange.

5.1.5 PHOTOASSOCIATION LASER

The PA light is provided by a commercially available Toptica DL Pro whose light is amplified by a Toptica BoosTA tapered amplifier. When the DL Pro's feed-forward is optimized, it has a mode hop free tuning range of around 20 GHz. Like the other ECDL's, this one is again tuned with a piezo. The tuning voltage is supplied by a high precision external SRS DS345 function generator, which is capable of producing waveforms with periods of several hours. A typical operating current and power output are 250 mA and 40 mA, respectively. The light is fiber coupled into the BoosTA tapered amplifier

A small fraction of the BoosTA output is picked off by a glass slide, and fiber launched into a Burleigh WA-1000 wavemeter for frequency monitoring. The wavemeter analog output is sent to the LabView program to be collected alongside the rest of the data. The main portion of the beam then continues through the glass slide and onto an AOM, which is there to enable switching. The -1st order is fiber launched and sent to the science chamber. The AOM is tuned to 62 MHz, which is where we found its highest efficiency to be. The frequency data from the wavemeter is subsequently shifted by +62 MHz during the data processing. A variable attenuation wheel is placed in the beam to allow for easy power control.

At the science chamber, we launch the PA laser out of the fiber with a a 15.29 mm focal length lens, collimating the light into a beam with a waist of about 350 μm. A second 400 mm lens is in place to focus the beam down to a tight waist and achieve the intensities we require for PA spectroscopy. The focusing lens is mounted on a xyz translation stage for alignment and focuses the light to a waist 400 mm away, directly on top of the MOTs. 400 mm on the other side of the MOTs, another f=400 mm lens recollimates the PA laser beam before a retroreflection mirror reflects the light back onto itself. After the second pass through the lens, the light is again focused down to a waist on top of the MOTs, this time from the opposite direction. This serves both to increase the intensity of the PA beam at the MOT, balances the forces applied to the MOT when the PA laser is tuned near resonance. The alignment procedure is discussed in detail in the PA Experimental Technique section 5.5.

5.2 VACUUM SYSTEM AND MAGNETIC FIELDS

Magneto-optical traps require vacuum pressures of 10^{-7} Torr or less to form.

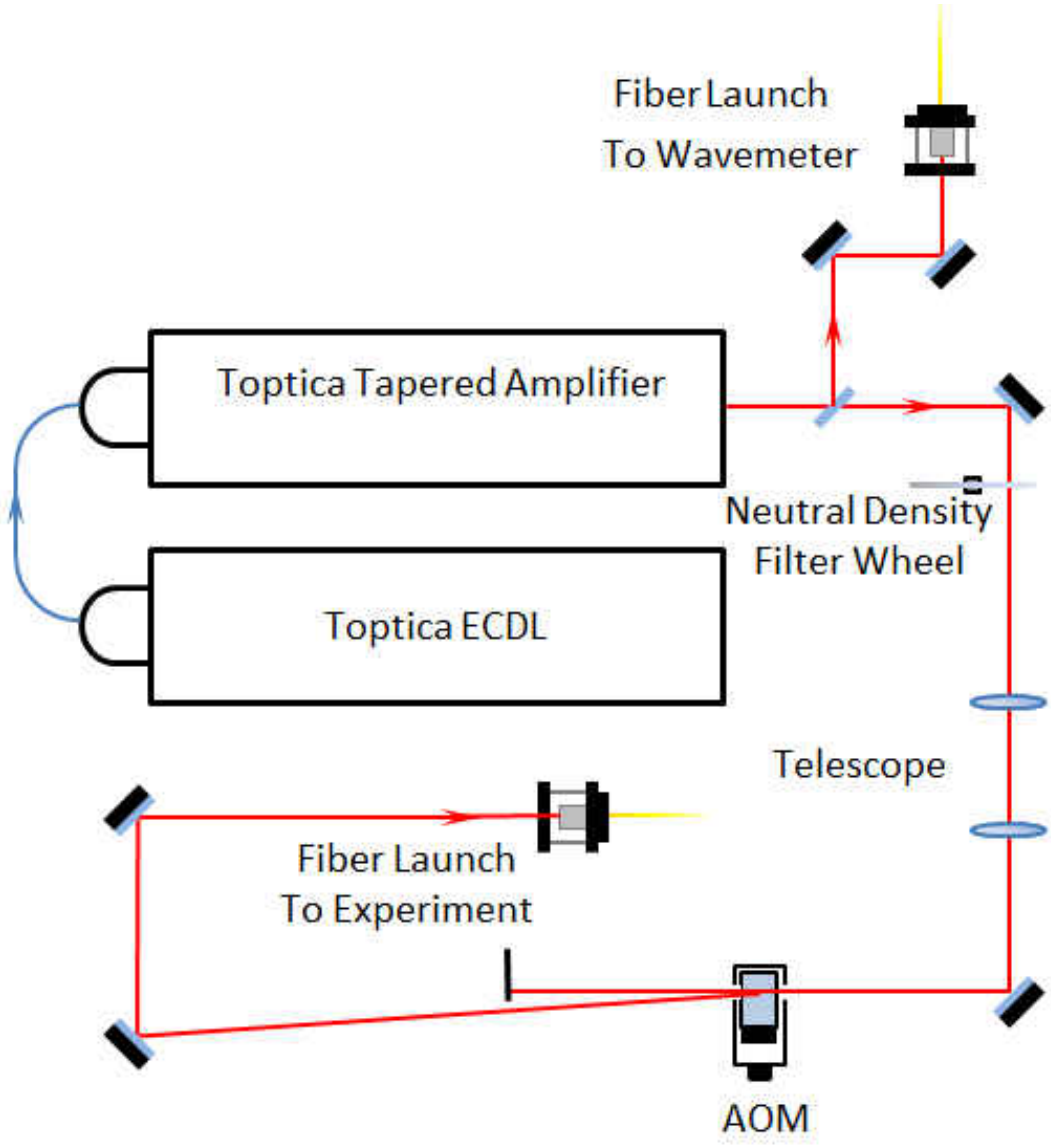

FIG. 53: A diagram of the PA laser and tapered amplifier, as described in Section 5.1.5.

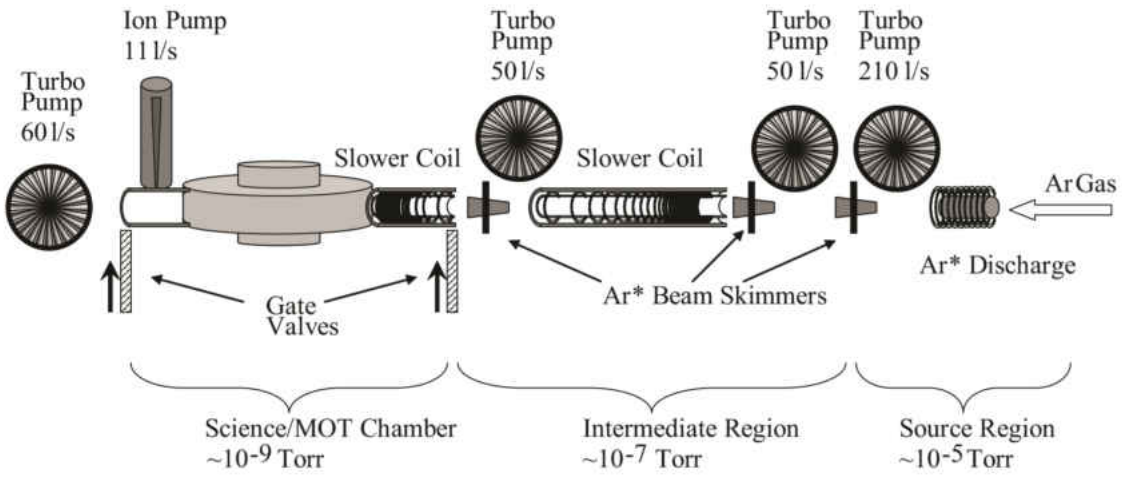

FIG. 54: A picture of the overall chamber design. The Ar gas enters from the right, and passes through two stages of differential pumping, the Zeeman slower, a third stage of differential pumping, and finally enters the science chamber on the left. Figure credit: M. Shaffer [1].

At high pressures, collisions from nitrogen, helium, water molecules, argon, and rubidium significantly reduce MOT density. To counter this, the Science Chamber is at low pressure of around 10^{-8} Torr. On the other end of our apparatus, the plasma discharge used to excite Ar into a metastable state works best with a pressure around a few mTorr. In this section, we follow the path of a Ar atom through the apparatus. We start by discussing the RF discharge. We then move on through the Zeeman slower, and finally, into the Science Chamber.

5.2.1 Ar rf DISCHARGE

Before any thought can be given to cooling and trapping our Ar, we must first excite it to the $5s[3/2]_2$ metastable state. Similar to what was discussed in Subsection 3.2.3, we will again use an RF discharge. Where previously our discharges were formed in cells, now we form the plasma near the source of an atomic beam. Gas flow from a cylinder is controlled with a leak valve. The gas enters a quartz tube with copper magnet wire coils forming an antenna around it. 2.5 W of power, tuned with a MFK-921 antenna, is sent to the coils to start and maintain the plasma. From previous work we expect that the discharge has a metastable efficiency on order of 10^{-4} [1]. The neutral atoms in the plasma leave the tube with a $cos(\theta)$ distribution.

We use differential pumping to achieve lower pressures in the science chamber when the atomic beam is running. The beam passes through two chambers: each separated by a narrow tube, and each with its own turbo pump. Atoms that have incorrect trajectories and fail to make it through the narrow tubes are pumped out of the chamber with a turbo pump. Through each stage, the pressure decreases and atomic beam collimation increases.

The second differential pumping chamber had a nude ion gauge installed, which was used to monitor the beam flow. When no Ar is flowing, typical pressures are in the low 10^{-9} Torr region. To ignite a plasma, we typically have to increase the gas flow until the ion gauge reads over 5×10^{-6} Torr.

The glass tube provides a second benefit. We send light from our master laser over to the discharge via a fiber optic cable, where we perform saturated absorption spectroscopy within the atomic beam plasma. In this way the discharge simultaneously provides a source of metastable Ar atoms for both locking our lasers and filling a MOT.

A downside to this method is the plasma produces large numbers of ions. As described later, ion detection is our primary way to detect PA. Considerable effort went into minimizing ion production and keeping ions from reaching the science chamber. In the first differential pumping chamber, a previous graduate student had installed parallel plates on either side of the atomic beam and connected them to an electric feed-through. Naively we might compare the kinetic energy of an ion to the electric potential of a low voltage across these plates, and expect that we may easily remove any unwanted ions. In reality these ions are promulgating through a grounded stainless steel vacuum chamber with other field lines introduced from the ions themselves, an ion gauge, the plasma, and static charge. We found that the parallel plates acted as an ion optic, often cleaning a large number of ions out of the beam, but sometimes focusing them in such a way as to massively increase the ion counts detected in the science chamber.

To add a further complication, many different plasma modes may exist in the tube. Changing either pressure or the antenna tuning causes the plasma to switch between these modes. Mode hops can be clearly seen with the naked eye as well as in ion production. The pressure/SWR phase space was systematically mapped out to find combinations that offer low ion production and high stability Ar^* production. Our standard plasma settings are a power of 2.5 W and a pressure of 9×10^{-7} Torr.

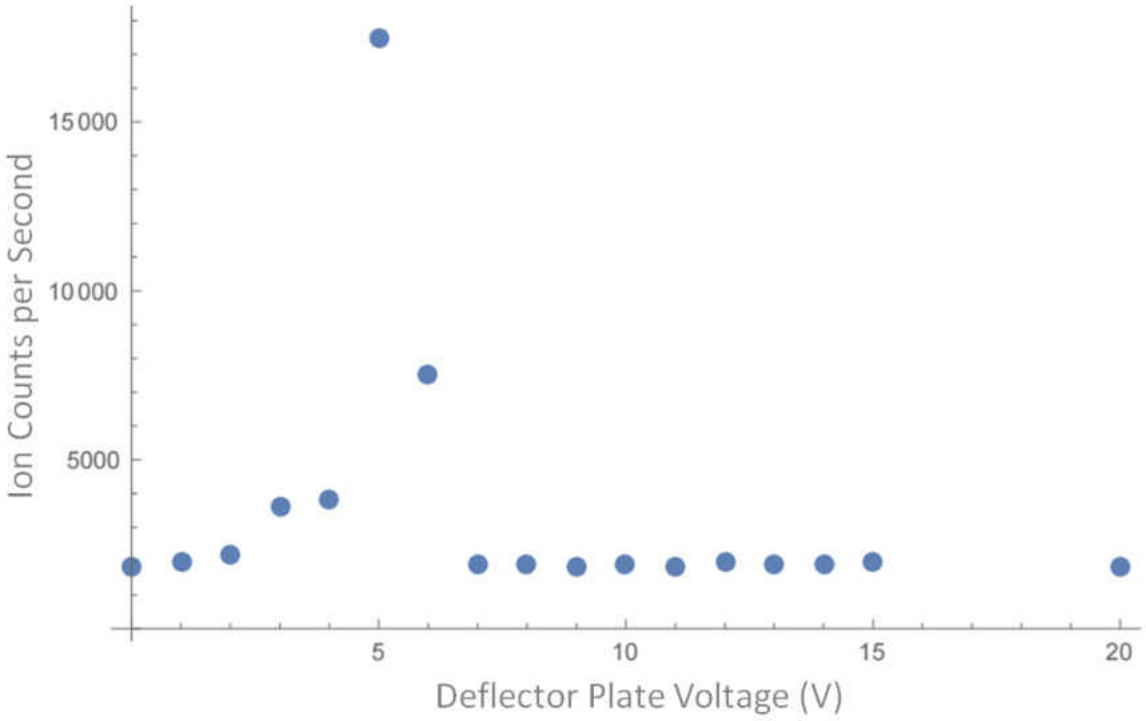

FIG. 55: A graph that shows ion counts as a function of deflector plate voltage.

Under these conditions one might expect to measure about 2000 ion counts per second with our ion detection in the science chamber.

This is far from an ideal solution. We have found that our leak valve does not regulate flow as well as one would hope. Over time, small pressure changes can cause the plasma to change from one mode to another. These changes typically take several minutes, and during the transition we can measure a steady and overwhelming increase in ions. Figure 56 shows an example of this. Plasma mode changes were a serious challenge when attempting to take long duration scans.

While previous work done in this chamber used the same discharge source, we are especially susceptible to fluctuations within it. Earlier students were investigating PA in heteronuclear $Ar^* + Ar^*$ interactions. We are investigating $Rb + Ar^*$, and our signal is likely to be smaller due to the C_6/R^6 homonuclear potential. In addition, since we need to subtract out PA excitation signals due solely to the $Ar^* + Ar^*$ interactions, we now are looking for differences between two sets of scans, allowing two opportunities for plasma fluctuations to be mistaken as real features. Without careful consideration and monitoring of the plasma, small amplitude changes due to

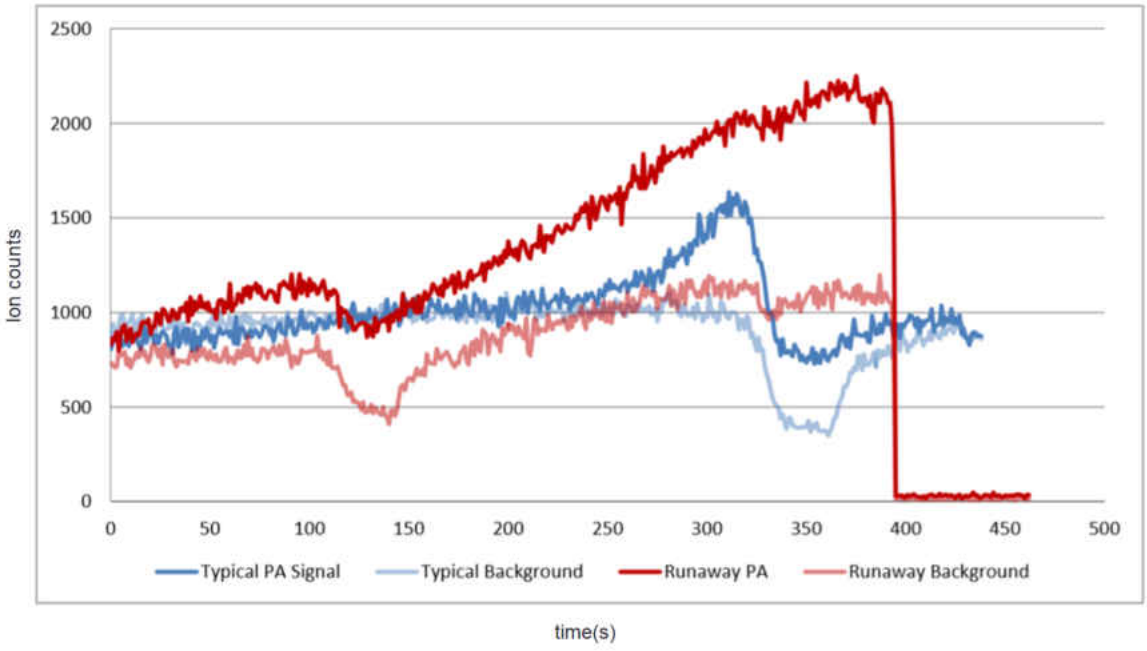

FIG. 56: A graph showing a scan where the plasma began to switch modes. The blue plots show a typical run, and the red plots show a run where the plasma switched modes. One can see how the shape of the "PA data" in the red run is largely determined by changes to the background, shown in light red. Ion production continued to increase throughout the run, and around data point 400, the plasma extinguished. Both runs were taken within an hour of each other.

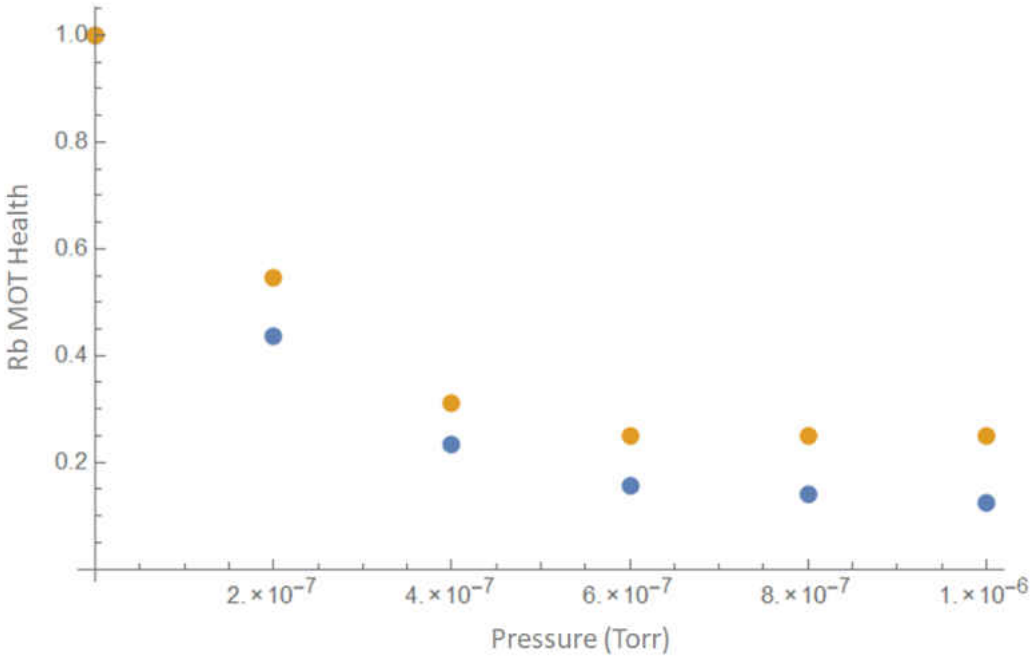

FIG. 57: A graph showing Rb fluorescence v.s atomic beam flow as measured by the nude ion gauge in the second chamber. We see that even at low atomic flux, the beam can dramatically harm the Rb MOT. At higher pressures the Rb MOT is completely destroyed.

plasma fluctuation have the potential to be misconstrued as RbAr PA.

Finally, we must consider the fact that the beam is mostly full of neutral ground state Ar atoms. A large portion of these atoms will make their way into the science chamber at full velocity and have a probability of colliding with the either of the MOTs. The detrimental effect can readily be seen in the health of the Rb MOT in real time looking at the Rb MOT as the Ar atomic beam is turned on. To study its effect, we took fluorescent measurements from the Rb MOT while we varied the pressure, as measured by the nude ion gauge in the second differential pumping chamber. In the ideal range for the Ar* MOT, the Rb MOT is collisionally attenuated down to 12.5% of its normal atom number. We were able to increase this to 25% by running the turbo pumps at higher speeds. While far from ideal, we are forced to run in this range by the Ar* MOT, which will not form in the low-flow ranges where the Rb MOT is fully healthy. We are able to somewhat compensate for the Rb atom loss by increasing the Rb getter current, and loading what would be a huge Rb MOT under normal circumstances.

5.2.2 ZEEMAN SLOWER

As discussed in Section 4.1.5, the overwhelming majority of Ar* atoms in the beam are traveling at speeds too high to be caught in the MOT. We employ a Zeeman slower that is able to slow about half the Ar* atoms down to catchable speeds. To apply this one dimensional cooling force, we use 50 mW of 811 nm laser light detuned by -160 MHz. The magnetic field gradient is produced by two sets of coils, each created by wrapping 14 gauge magnet wire around the vacuum system. The first coil set requires 28 A of current, and the second requires 18 A, supplied by two Hewlett-Packard 6259B DC power supplies. A gate valve and turbo pump were placed in the region between the two coils and give us the ability to seal off the science chamber.

An atom entering the first coil set initially experiences a magnetic field of +250 Gauss. As the atom propagates through the slower, the magnetic field decreases to zero following the relationship described in Eqn. 82. Upon entering the second coil set, the magnetic field will continue to decrease, ending just under -100 Gauss. The two-coil method allows us to produce the same ΔB as a single coil would, but requires a lower current. Even reduced, the Zeeman current is likely to overheat the coils, so a VWR recirculator pump provides a supply of chilled water. Our Zeeman slower was originally designed and built by a previous graduate student, Hauke Busch. It is described in great detail in his dissertation [2].

5.2.3 SCIENCE CHAMBER

The heart of our experimental apparatus is our "science chamber." It is a stainless steel vacuum chamber with fourteen CF viewports built into it. The Zeeman slower empties into the chamber through one of the viewports, and both the Rb and the Ar* MOTs form at the chamber's center. Two of the viewports are dedicated to the PA laser, which comes to a focus overlapping the MOTs in the center. For use in ion detection, the chamber houses a Channeltron with collection mesh mounted to a feedthrough, and allows fluorescence detection through an allotted viewport. Attached to the chamber are Rb getters, an ion pump, and a turbo pump. The remaining viewports are used to allow the MOT trapping beams into the chamber.

To form the trapping magnetic field for the MOT, we used a pair of coils in an anti-Helmholtz configuration. They are situated directly above and directly below

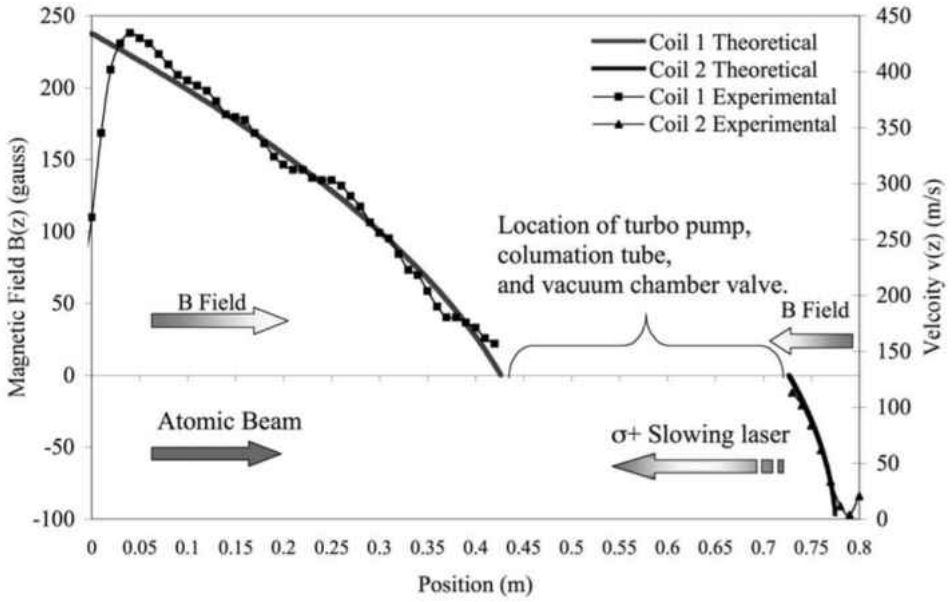

FIG. 58: A diagram showing the B-field of arrangement within our Zeeman slower. Figure credit: H. Busch. [2]

the chamber, and are made from 14-gauge magnet wire. For finer control, each coil is powered by its own power supply. The top coil typically has 6.13 A of current supplied by a Topward 3306D DC power supply, and the lower coil typically has 6.5 A of current supplied by a Tenma 72-6153 DC power supply.

By themselves, the two anti-Helmholtz coils do not guarantee that we will have $B = 0$ at the center of the science chamber. A variety of sources ranging from electrical wires in the building, to Earth's magnetic field, to objects on the optical table, cause stray magnetic fields. We negate them with a system of three orthogonal shim coils. Currents to the coils are supplied by MPJA HY1802D DC power supplies, and are constantly changing from week to week, as small adjustments are needed to maintain high quality MOTs. However, shim currents tend to have values of less than 1 A.

5.3 DETECTION METHODS

We use two separate methods to search for signs of photoassociation: ion detection and fluorescence detection. This provides a richer, more complete view of what is happening during the experiment than any single method could give on its

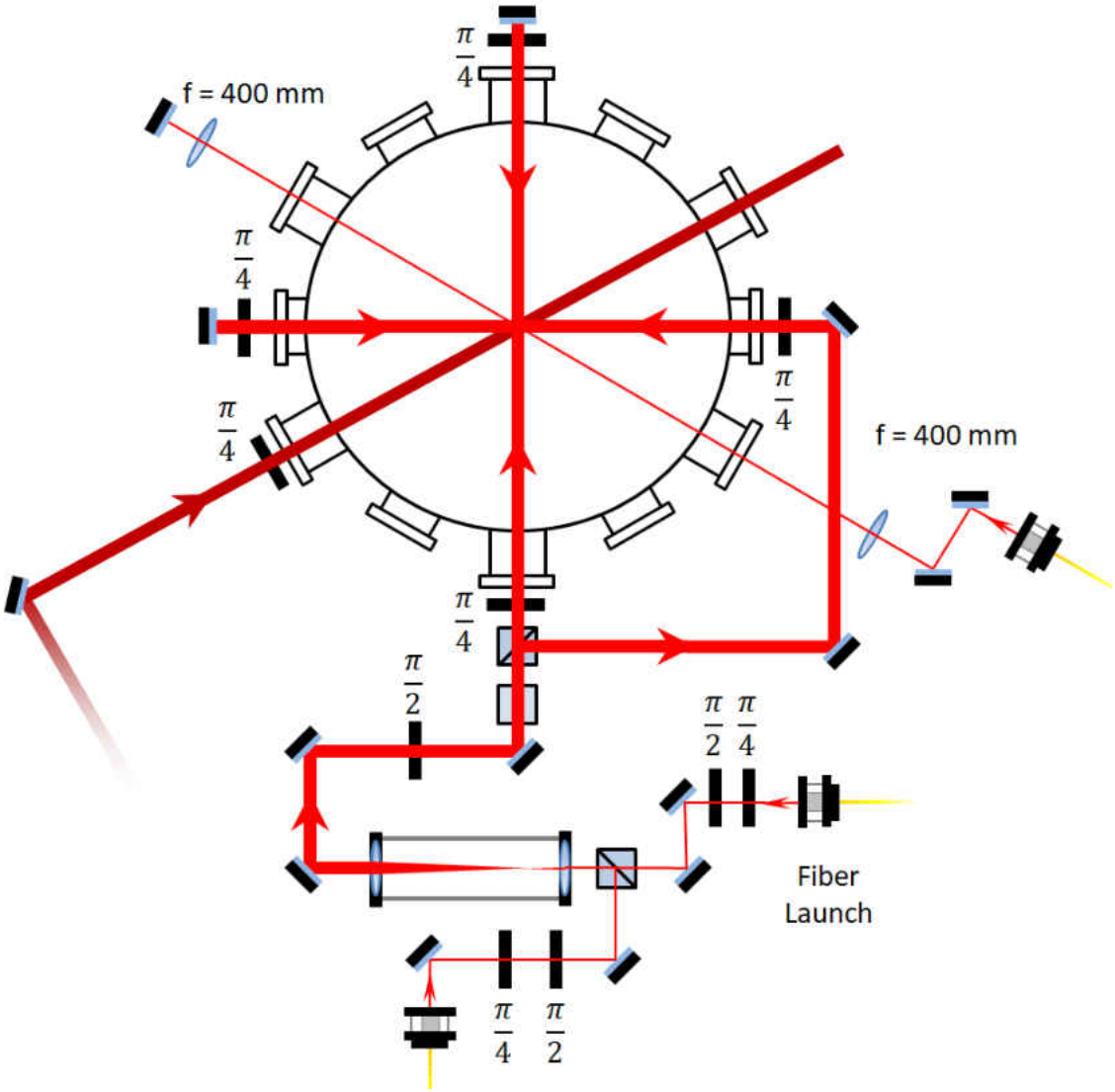

FIG. 59: A diagram of the science chamber and all of the lasers entering it. Both MOTs form at the center, where the lasers overlap. The dark red beam is the Zeeman slower.

own. In this section we discuss the equipment employed for each method, as well as calibrations of this equipment.

5.3.1 ION COUNT DETECTION

There is no ion production within the Rb MOT by itself. However, within the Ar^* MOT, the trapping beams excite Ar^* atoms out of an S-orbital into a P-orbital, from where dipole interactions lead to collisions. The resulting Penning ionization, and to a lesser extent, associative ionization, produce a steady stream of ions. Under typical conditions, we might expect to count between 5000 to 8000 counts per second when the trapping laser is on. Even with this constant background coming from the Ar^* MOT, we find ion detection to be a valuable tool in our search for photoassociative spectra.

Previously, ion counts have been used as a way to monitor collisions between Rb and Ar^* atoms within a well-overlapped dual species MOT [2]. As described in Section 4.4.1, we anticipate detecting these collisions and monitoring a change in ion production when the PA laser is tuned to a resonance. Due to relatively small differences in excitation energies of the first excited states in both of our atoms, we anticipate a large C_6'' excited molecular state dispersion coefficient. We expect this to lead to a moderate change in ion production.

We detect ion production with a Galileo brand Channeltron. Its collection efficiency is greatly enhanced with a collection mesh installed 2 mm in front of the Channeltron cone, and 40 mm from the MOTs. Both the mesh and the Channeltron are mounted inside the science chamber with screw holes tapped in a CF feedthrough. Typically the cone is kept at -2650 V and the mesh at -2625 V. The resulting potential difference between the cone and the mesh creates a small electric field that collects ions from the MOT and accelerates them into the Channeltron. Counts from the Channeltron are registered as a negative current pulse about 8 mV to 10 mV high and only a few ns wide, before they are sent through one channel on an SR445 pre-amp. The pulse triggers an SR400 gated photon counter and is registered as a single ion detected, which is controlled by a LabView code. It and the timings used will be discussed later.

While preparing the main experiment, we examined ideal mesh and Channeltron voltages. Having experienced ion optic effects while adjusting the deflector voltages upstream (see Fig. 55), we expected there might be similar effects here. We were

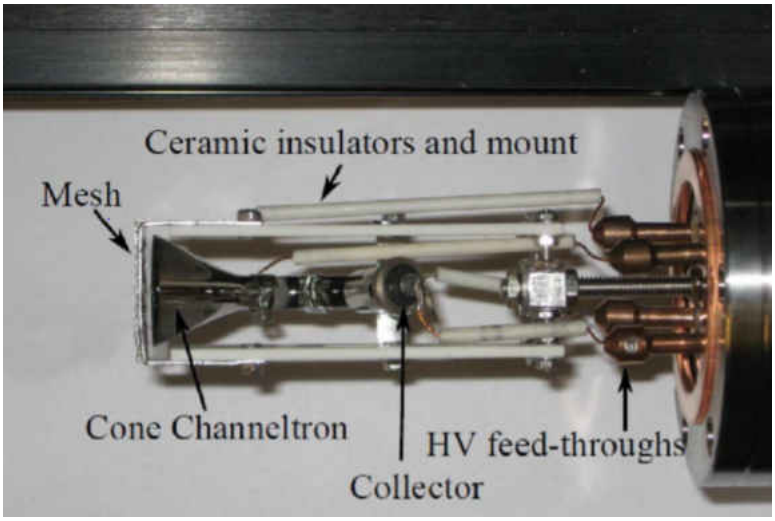

FIG. 60: A photograph of the Channeltron before it was mounted.

hopeful that there existed combinations of the mesh and Channeltron voltages that would improve detection of MOT ions, and lower detection of ions from the atomic beam and RF discharge. After thoroughly mapping out this interaction, we concluded that the ratio between MOT ions and Zeeman slower ions remained constant.

We found that the mesh was absolutely essential, and no counts were detected below V_{mesh}=2000 V. Ion counts increased exponentially by increasing either the mesh or Channeltron voltages. We ran our Channeltron at the highest voltage that we felt posed no risk of damage. It has a maximum rated voltage above 3 kV, however because of experience with another damaged Channeltron and the fact that ours is quite old, we decided to max it at 2650 V. Our data shows that we want to have as high of a mesh voltage as possible, but the mesh must obviously be at a lower voltage than the Channeltron. As such, we ran the V_{mesh} at 2625 V.

Not all counts that come from the Channeltron are due to ions. Much like a photomultiplier tube, Channeltrons may produce dark counts from thermally emitted electrons. Thermal electrons may emit from anywhere along the Channeltron, but only those that happen to emit at the top of the cone will be amplified by the maximum gain. As such, dark counts tend to have lower peak height than signal counts, which all start at the top of the cone. A correctly set discriminator level allows one to filter out the majority of the dark counts, and still catch the majority of the real counts. Using ions from the RF discharge, we mapped out both real

count and dark count peak height distributions. We determined that dark counts were negligible with a discriminator setting as low as 10 mV. We chose to run with a discriminator level of -12 mV, where we found the ratio of real MOT counts to dark counts to be 540 to 1.

5.3.2 PMT Rb FLUORESCENCE DETECTION

We perform trap loss spectroscopy simultaneously to the ion detection described in the previous subsection. After Rb and Ar* atoms are photoassociatively elevated into an excited molecular state, they may radiatively decay into a repulsive state, resulting in two heated atoms with enough kinetic energy to escape the trap. This leads to a decrease in MOT fluorescence as the PA laser beam crosses photoassociative features.

We observe MOT fluorescence through a viewport on the science chamber. Light is collected with a two-inch 50.8 mm focal length lens immediately outside the window, 180 mm away from the MOT. A second lens, this time with a 35 mm focal length, is located 140 mm from the first lens, forming a relay image. The light then passes through a 780 nm narrow band interference filter before being detected by a Hamamatsu R928 PMT, which has a quantum efficiency of about 5% at 780 nm. To cut down on background scattering, an iris is placed at the focal point between the two lenses. Each day, the PMT is temporarily removed, and a Sanyo VCB-3384 CCD video camera is placed in the correct location to image the MOT. The iris positioning is then optimized to let MOT light through while ensuring that the overwhelming majority of the background light is blocked.

Experimental timings are described in Section 6.1.2. It is worth mentioning here that during data collection all of the MOT trapping beams are turned off. Without laser fields to drive their respective atomic transitions, there is no fluorescence for the PMT to detect. Measuring immediately after the trap beams are turned back on yields information on how much trap loss occurred during the cycle. We trigger a SR250 gated boxcar averager off of the pulse generator that runs the entire experiment. The boxcar averager gate opens for 15 μs immediately as the trapping light comes back on. The output is a DC voltage proportional to the running average over the previous 300 open gates. The voltage is fed into an analog input on a National Instruments BNC-2120 data acquisition board and then sampled. The board's analog input adds a small detection noise of a few mV. By increasing the PMT gain, we

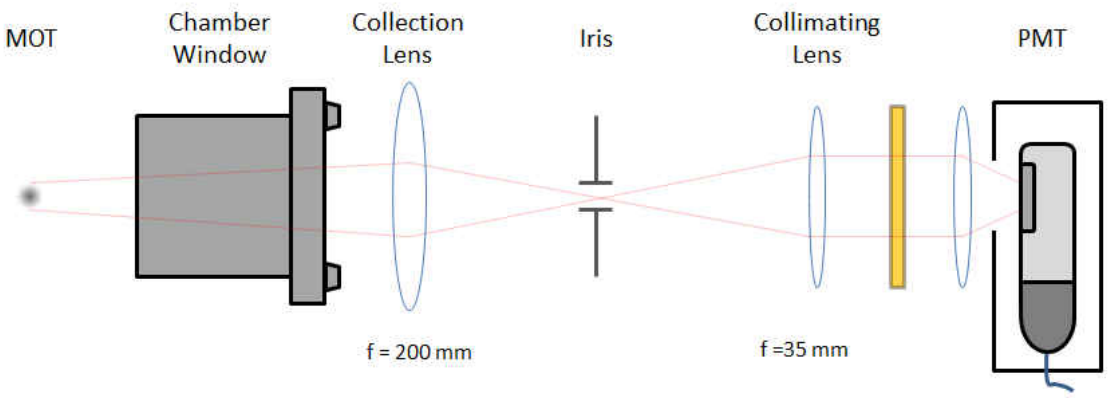

FIG. 61: A diagram of the imaging system used to measure Rb MOT fluorescence.

may minimize the effect of detection noise on our data's signal to noise ratio. The PMT's gain control voltage was selected to be 0.680 V in order maximize the signal size without railing the boxcar averager input.

We are only able to use this technique to observe the Rb MOT. We replaced the 780 nm interference filter with an 810 nm one and attempted to measure Ar* MOT fluorescence. Unfortunately, light from the Zeeman slower scatters into the PMT and swamps the signal. In future experiments, the vacuum chamber may be redesigned to allow for fluorescence measurements of both MOTs to be taken.

5.4 OVERLAPPING BOTH MOTS

Photoassociative excitation of two atoms into a molecule requires them to be close enough to each other to collide. Having more atoms within a smaller volume greatly increases the number of atom pairs with the correct internuclear separations. Other researchers have increased atom density by performing their search within a dark-spot MOT, or within a far-off-resonance trap. Unlike alkali-metals, higher steady state densities within a metastable noble gas MOT are limited by Penning ionization.

Magneto-optical traps typically have a Gaussian density distribution. To maximize dual species collisions, we must ensure that the densest part of the Rb MOT overlays the densest part of the Ar* MOT. A loose overlap simply will not suffice. As this is a matter of great importance to the success of this experiment, we have have developed three separate methods to detect how well the MOTs are overlapped.

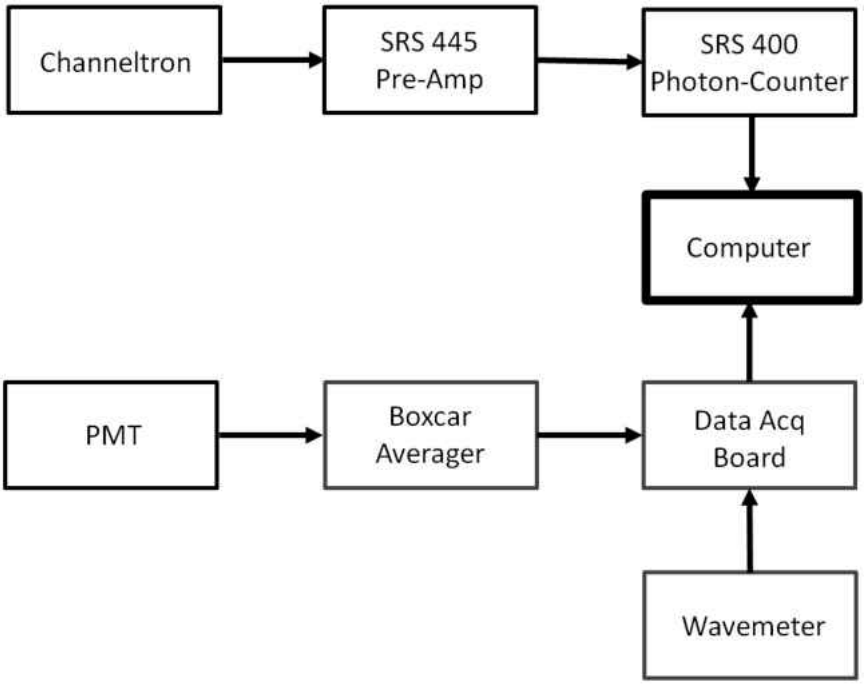

FIG. 62: A schematic of the data acquisition system.

5.4.1 CAMERAS

The most obvious method to judge MOT overlap is to simply look at them with high precision cameras. Two Apogee Alta TEC-cooled cameras are positioned to give us orthogonal views of both MOTs. The cameras typically had exposure times of 2.0 seconds. The first camera images the MOTs with a 100 mm focal length lens mounted in a lens tube 290 mm from the science chamber center. The camera shares a chamber porthole with the PA laser and only has access to the MOTs when a flip mounted mirror is in the upright position. The second camera can be interchanged with the PMT and uses the same set of imaging optics described in section 5.3.2.

When both MOTs are viewed at the same time it becomes impossible to distinguish the densest parts of each. Instead, we individually photograph the MOTs. In a series of four images, we view the lone Ar^* MOT and the lone Rb MOT from the left camera, then again the lone Ar^* and the lone Rb MOT from the right camera. We wrote a Mathematica script to combine and process the images, as seen in Fig. 64. Using the processed images as a guide, we make a single small adjustment to either an alignment mirror or a shim coil. After an adjustment, another set of photographs

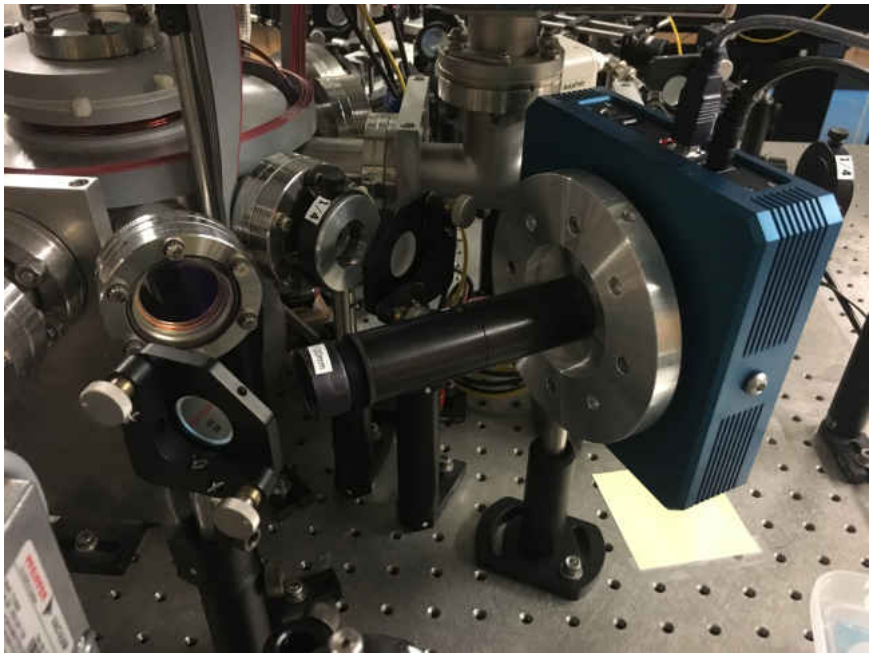

FIG. 63: A photo showing one of the two Apogee Alta cameras mounted in place.

is taken and the process may be repeated in an iterative manner as many times as necessary.

5.4.2 EXCESS ION COUNTS

Collisions within the Ar* MOT between highly energetic metastable Ar atoms produce a continuous stream of ions through Penning and associative ionization. We regularly detect and use these ion counts as a measure of the Ar* MOT density. In addition to these expected counts, we found an upsurge in ion production when the Rb MOT was both present and well overlapped. We refer to the counts as "Excess Ion Counts," as they are in excess of what we would expect from just the Ar* MOT with no PA laser present. They are likely also due to Penning and associative ionization that are a result of collisions between Rb and Ar*. In this section we describe the utility the excess ion counts provide, but an investigation into the cause of the counts is discussed later. We found that monitoring the excess counts provided an excellent overlap diagnostic tool. Excess ion counts only appear when the two MOTs are highly overlapped. For example, in the first two alignment pictures in Fig. 64, we would not expect to see excess ion counts. When they were fully overlapped, as seen

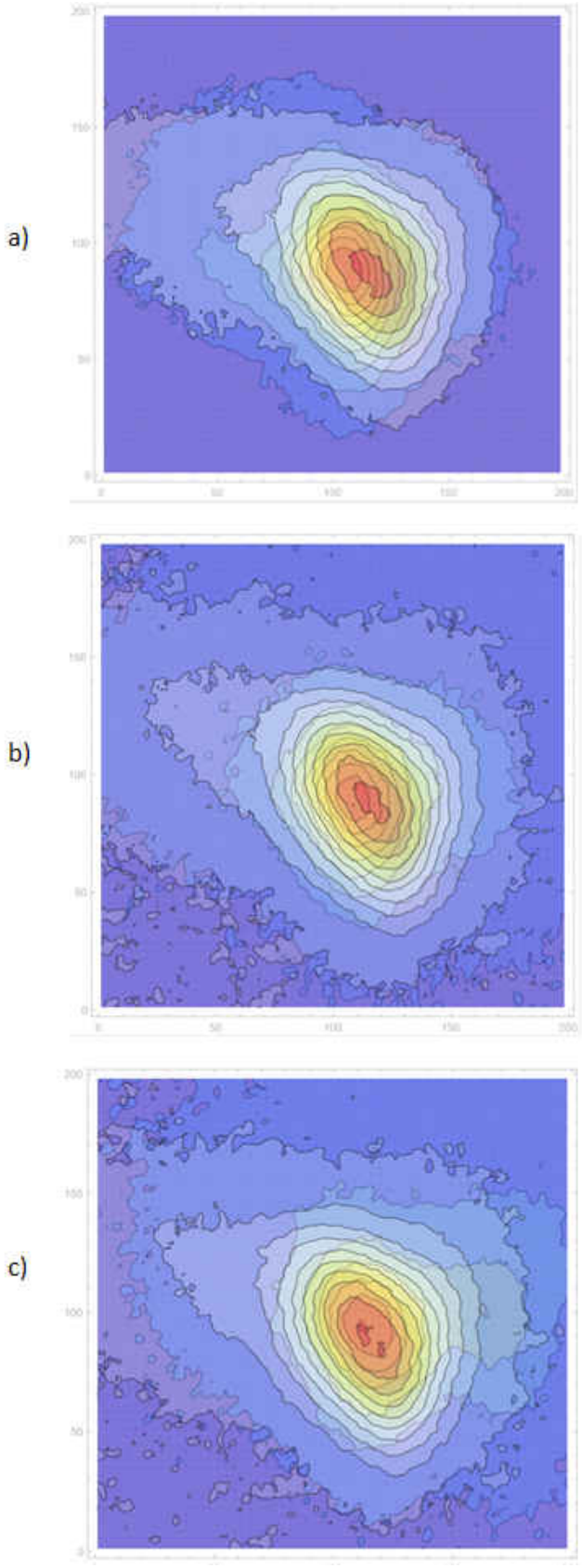

FIG. 64: A series of photos showing the progression of MOT overlap.

in the last stage shown in Fig. 64, we might then to start detecting excess counts.

Once the Apogee Alta cameras have the MOTs overlapped enough to start producing excess ion counts, we then maximize the excess counts by making minute adjustments to the mirrors and shim coils. Under optimal alignment, we expect around 600 extra ion counts per second. Comparing images taken immediately before and immediately after ion count maximization shows no appreciable difference, suggesting excess ion count maximization has a higher sensitivity than the camera alignment described in Section 5.4.1.

5.4.3 DECREASED MOT FLUORESCENCE

Atom number within a dual species MOT may be calculated by solving for the steady-state solution to Eqn. 78. Atoms are gained through capture, and lost through collisions with background vapor, same species collisions, and collisions with atoms in a second MOT occupying the same space. Trap loss from inter-species collisions may be observed as a decrease in fluorescence. This effect was investigated in depth by Mike Shaffer, who used trap loss to calculate the trap loss rate coefficient for Ar/Rb dual species MOTs. He observed a fluorescence decrease of up to 3%. [1]

In an attempt to use trap loss as an overlap indicator, we installed a narrow band 810 nm filter on one of the Apogee Alta cameras. With the filter present, 780 nm light from the Rb MOT is removed and the camera will only view Ar^* MOT fluorescence. We then take a set of ten images consisting of the Ar^* MOT, alternating between the Rb MOT being present and its being blocked. Under good overlap conditions, we expect there to be less Ar^* fluorescence when the Rb MOT is unblocked. A Mathematica script crops all the images, sums up the total counts across all the pixels, and finds the difference in each of the five pairs. Using this method, we have detected a fluorescence decrease of up to $2.5\,\% \pm 0.8\%$. However, we did not add this technique to our standard overlap procedure. There is a large variance between single pairs of images, which requires us to take many shots and turns the method into a time intensive process. This is problematic for a method involved in an iterative process that may have to be repeated many times. However, having successfully used this technique to replicate previous results, we have added confidence in our overlap detection via the dual cameras and excess ion counts.

5.5 PA LASER ALIGNMENT

Not only do the two MOTs have to overlap precisely. The PA laser has to come to a focus on top of the densest part of the overlap. At the start of each day, and many times throughout a particularly temperature-unstable or noisy day, the PA laser beam must be realigned. It is hard to overstate how sensitive PA spectra are to alignment of the PA laser beam. It is equally hard to overstate how sensitive the PA spectra are to the alignment of the retroreflection, in particular. If the retroreflection does not exquisitely balance out the force from the forward propagating PA laser, as the PA beam approaches resonance, it will push atoms away and destroy the MOT. In subsequent scans, the PA spectra will be masked by deterioration within MOT densities.

Over many weeks we developed an alignment procedure that allowed us to reliably produce high quality homonuclear Ar^* PA spectra. For the benefit of any future graduate students who work on the same apparatus in the future, we have included the procedure below:

1. Block the retroreflection.
2. Tune the laser to resonance.
3. Using the X-Y control knobs on the f=400 mm mirror, adjust the beam until it blows the MOT away.
4. Lower the power in the PA beam, and repeat step 2. Continue to do this until the PA beam is so low power that it has little to no effect.
5. Select a power for the PA laser that is high enough that the MOT becomes faint, but not so high that the MOT is fully obliterated.
6. Unblock the retroreflection and coarsely align it back on top of itself, all the way back to the fiber launcher.
7. Using the X-Y control on either the second lens or the retro mirror, make very small adjustments to the retroreflection. When the system is well-aligned, the two beams will counter each other's momentum transfer, and the MOT will shine brightly.

CHAPTER 6

MAIN PHOTOASSOCIATION EXPERIMENTS

In this chapter, we discuss the methodologies and results from two separate photoassociation spectroscopy experiments. Within the discussion of the first experiment, we describe our data collection cycle and justify the time frames chosen with experimental data. We also show results that are in agreement with previous studies. The first experiment involved taking sets of scans with both the Ar^* and Rb MOT present, and sets of scans with just the Ar^* MOT present. The difference between the two sets could be analyzed for signs of RbAr molecular excitation. During data collection, we found that we were susceptible to fluctuations within the RF discharge. A second experiment was designed to interlace data points during the data collection process both with and without the Rb MOT. This was done in the hope that changes in the plasma will show up identically in both sets of data and be subtracted out.

6.1 FIRST EXPERIMENT OVERVIEW

Our first experiment was very briefly described above. In essence, we produce a MOT made from Ar^* atoms, and a second MOT made from Rb atoms. The MOTs are well overlapped and a photoassociation laser is focused through the densest part of their volumes. The laser is tuned several GHz below the Ar^* $4p[5/2]_3$ + Rb $5^2S_{1/2}$ asymptote and slowly scanned. When the PA laser is correctly tuned we expect to see a change in ion production as well as a decrease in MOT fluorescence, both of which are monitored. This experiment has an added complication. The energy difference between the Ar^* $4s[3/2]_2$ + Rb $5^2S_{1/2}$ to the Ar^* $4p[5/2]_3$ + Rb $5^2S_{1/2}$ is the same as the separation between the Ar^* $4s[3/2]_2$ + Ar^* $4s[3/2]_2$ asymptote to the Ar^* $4p[5/2]_3$ + Ar^* $4s[3/2]_2$ asymptote, which we know will show PA structure. Scans must be completed with and without the Rb MOT present, and only those features that correlate with the Rb being present may be considered to be from Rb + Ar^* interactions.

The distribution of internuclear separations within the system is a function of density, however, at any given time there will be far fewer atom pairs with small

separations than with large ones. Additionally, molecular transition probabilities will often decrease as internuclear separations start to decrease from long range, as described by the Landau−Zener approximation. As a result, when scanning over frequencies that correspond to sparsely populated internuclear separations, a higher laser intensity is required. A low power laser scanning far from resonance, where there are already few atom pairs, will only excite a small portion of them and will not produce a detectable signal. Conversely, a high power laser scanning near resonance will obliterate a MOT, and will also fail to produce a detectable signal. From previous work within the group, we understand of at which detunings various PA laser intensities start to damage the MOT. We have chosen the following intensities: 78 mW/cm^2, 390 mW/cm^2, 780 mW/cm^2, 3,900 mW/cm^2, and 16,000 mW/cm^2.

In this section we discuss the first experiment in more detail. We start with a detailed description of the timing cycles chosen and justifications of these timings based on experimental data. We then show successful replication of previous photoassociation spectroscopy done within an Ar* MOT, and finally, we present our results.

6.1.1 FIRST EXPERIMENT TIMING

We are only interested in single photon spectroscopy, therefore the Ar* and Rb trap lights must be off during data collection. Turning off MOT-trapping beams is inherently destructive to the MOTs, as is tuning the PA laser near resonance. This forces us to take data in short bursts, allowing the MOTs to reload in the time between data collection periods. If we extend data collection for too long, MOT density and our data quality suffer. Each data point is made up of hundreds of cycles, quickly switching between collecting data and reloading the MOTs hundreds of times each second, slowly building up statistics.

A single data run can take up to several hours, and over that time the density of the MOT may sometimes drift. Also, as described in Section 5.2.1, from time to time the Ar discharge changes plasma modes, dramatically altering background ion production. It is critical for us to have a measure of not only PA, but also of the corresponding MOT health, so that we do not mistake laboratory fluctuations as PA features. As such, our data collection cycle has three phases:

1. Phase 1 - MOT health measurement,

2. Phase 2 - PA measurement,

3. Phase 3 - MOT recovery time.

Phase 1 lasts 100 μs, during which we measure the ion counts from both MOTs while the trapping laser is on and the PA laser is off. Gate A on the SR400 photon counter is closed, and Gate B is open. Phase 2 lasts 200 μs, and during it we turn off the trapping beams and close Gate B. We turn on the PA laser and open Gate A, collecting ions that may signify photoassociative production of molecules. During Phase 3 both Gate A and Gate B are closed for 2.7 ms while the MOTs reload. Described in Section 5.3.2, the PMT measures 780 nm Rb fluorescence for the first 15 μs of Phase 3, as there is no fluorescence with the trapping beams off during Phase 2. To form a single data point, this entire 3 ms cycle is repeated 1333 times over 4 seconds. Each of these timings is controlled by a series of TTL pulses and internal delays. The length of Phase 1 was kept at a constant 100 μs for ease of comparison. In this section we discuss the rationale behind the other two lengths chosen.

6.1.2 EXAMINATION OF PHASE 2 LENGTH - DATA COLLECTION TIME

Before we could reasonably create our timing scheme, we needed to improve our understanding of the PA production phase. The following questions needed to be answered: First, what is the response time of the MOTs to TTL commands sent from our pulse generator; is there a long rise and fall time? Second, does PA occur throughout the data collection period, or does the PA laser quickly deplete available atom pairs? We performed these experiments on an Ar* MOT without the Rb present. With times of flight that only vary by a factor of $\sqrt{2}$ due to similar masses, comparable atom numbers, and comparable densities, timing information learned about the Ar* MOT is readily transferable to the Rb MOT. In addition, performing these tests in the Ar* MOT gave us a homonuclear PA signal with which we could optimize our system.

We are able to answer both of the above questions using an SR430 multichannel scalar (MCS). By rerouting the Channeltron output from the photon counter to the MCS and triggering off the data collection cycle start trigger, we are able to map the temporal profile of the incoming ion counts. Figure 66 is an example of one such test.

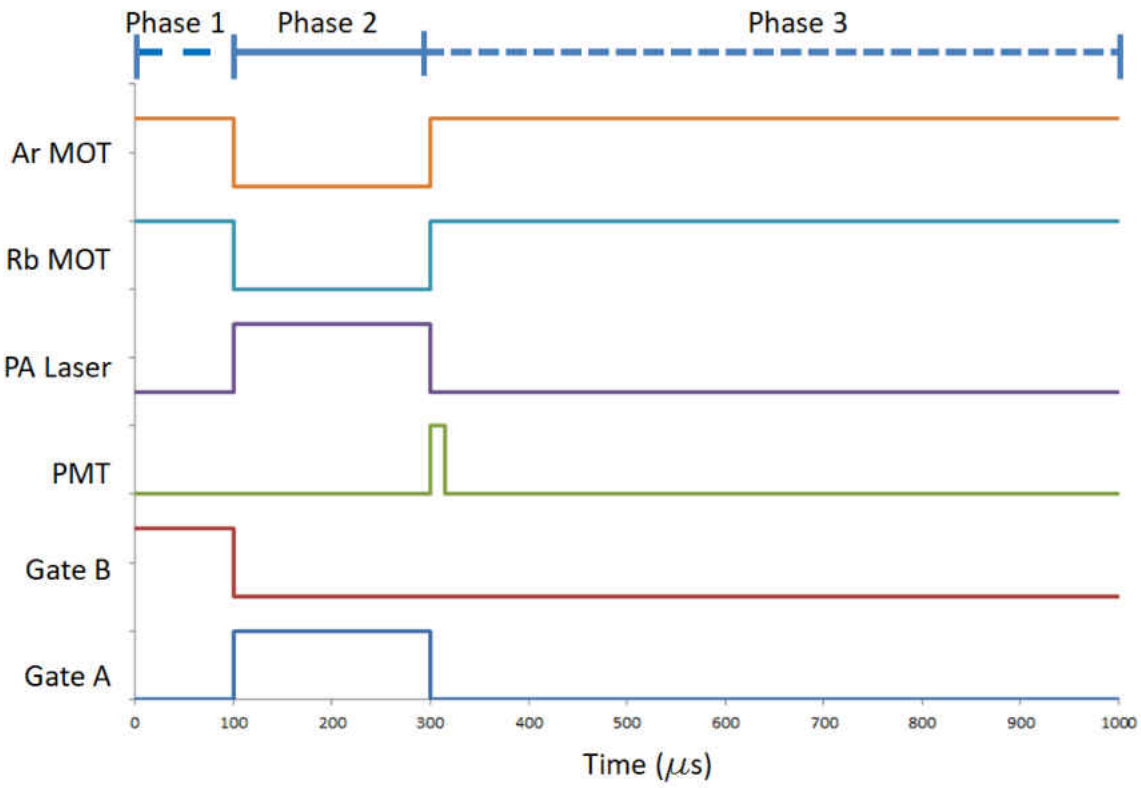

FIG. 65: A diagram showing the generic timing cycle.

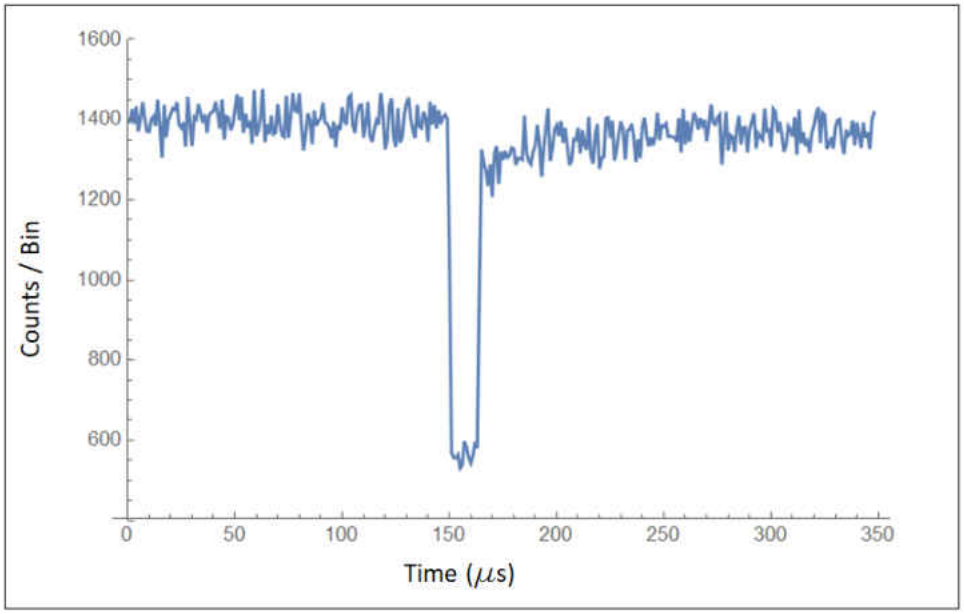

FIG. 66: A diagram from the MCS, showing the ion count response time to the trapping beams being shut off. After the trap lights come back on, one can see the MOT start to reload itself.

We determined that the fall time was consistently two 5.12 μs-wide collection bins, and that the rise time was equally as quick. Note, the MOT can be seen starting to reload atoms that were lost during the test. This shows up on the right half of the figure. With this data in hand, we are confident that our experimental system had fast enough response time that we were able to avoid extending the photon counter gates open into Phase 3.

In a similar experiment, we set the PA laser intensity to 780 mW/cm^2 and detuned it to 700 MHz below resonance, which are conditions that we know produce excellent Ar* + Ar* PA. We then used the MCS to map the incoming ion counts both with and without the presence of the PA laser. Subtracting the two scans from each other to view just the PA counts, we saw that they arrive evenly throughout the entire data collection period. This implies that over these time frames, existing atom pairs are depleted at a similar rate that new pairs are produced.

In a further examination of the data collection timing, we conducted PA scans in Ar, while varying the length of Phase 2 from 140 μs up to 450 μs, while maintaining the same long recovery time. We found that the signal to noise was highest in the 200 μs to 250 μs range, and that the absolute size of the feature started to decrease

above this range.

Finally, we wanted to confirm that the Rb MOT would be fine over these time ranges. We took fluorescence measurements immediately before and immediately after turning off the Rb trapping lasers. We measured trap loss at a variety of Phase 2 lengths, and determined that the trap loss in the Rb MOT due to the trapping light being off was inconsequential over the time frames we cared about. In the 200 μs to 250 μs range, trap loss was less than 1%. This level of trap loss makes sense when compared to the low velocities found at ultracold temperatures. Over 250 μs, we might only expect a trapped Rb atom to move 5 μm.

6.1.3 EXAMINATION OF PHASE 3 - MOT RELOADING TIME

In addition to optimizing the data collection length, we had to determine an appropriate length of time for Phase 3, the MOT reloading time. Ideally we want this time to be as short as possible while still allowing for the MOT to fully reload. Excessively large reloading times will dramatically lengthen the time of a single data run, and expose us to risk of plasma fluctuations without giving any added benefit. We fixed the Phase 2 time to 200 μs, varied the Phase 3 time, and counted the total ion counts over 10 seconds. The PA laser was turned on and detuned -700 MHz from resonance. We found that at 780 mW/cm^2 intensity, the system came to equilibrium around 8,000 μs recovery time. At 3,900 mW/cm^2 intensity, the system did not come to equilibrium until a recovery time of 15,000 μs was reached.

We selected a Phase 3 recovery time of 2800 μs. This was long enough that the Ar* MOT could fully reload at all except the highest powers, even with the PA laser relatively close to resonance. We decided there was no added value in lengthening the Phase 3 time so that the Ar* MOT could always be fully recovered because: 1) the times required were excessively long, 2) and the point of the higher power scans is to look further away from resonance than the low power scans can, making it irrelevant that they cannot also look close to resonance.

6.1.4 REPLICATION OF PREVIOUS DATA

As described above, we have chosen to search below the Ar* 4p[5/2]$_3$ + Rb $5^2S_{1/2}$ asymptote. From previous work, we know that in addition to any RbAr PA features that might be found, broad Ar* + Ar* photoassociative spectra will also appear over this range. A natural starting point is replication of previous work, which ensures

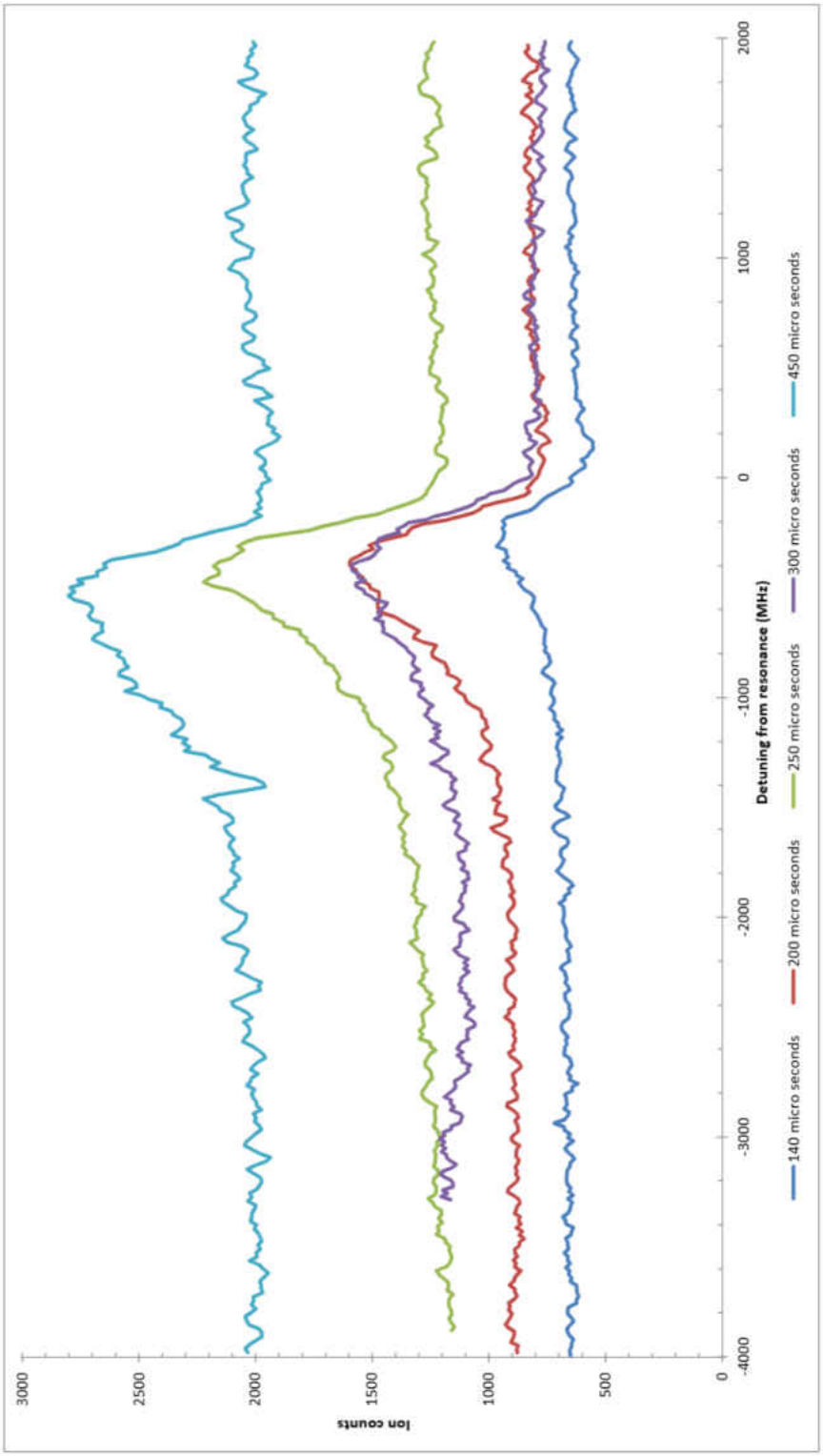

FIG. 67: A graph showing a series of data runs. In this experiment, we were interested in finding the optimal width for Phase 2 of our data cycle (The portion with the PA laser on and trap beams off). We varied the length and examined peak heights and background noise. The large dip in the 450 μs line, located around -1500 MHz, is due to a laser breaking lock and may be ignored.

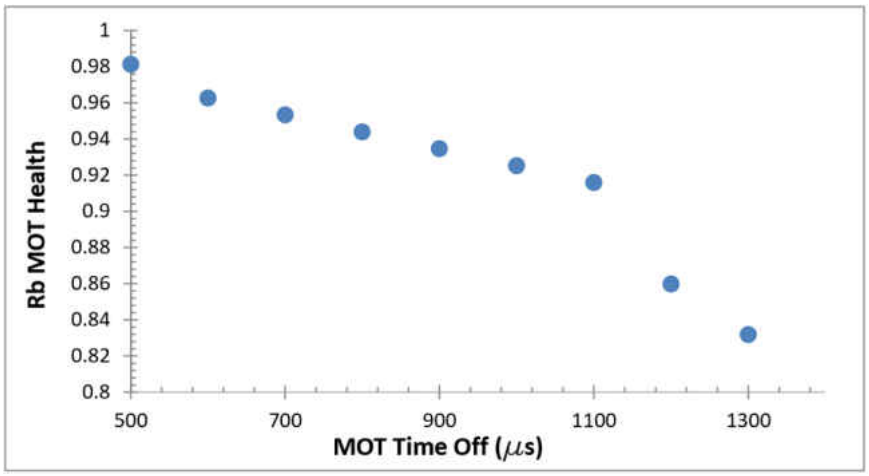

FIG. 68: A plot showing decrease in trap storage within the Rb MOT as a function of the amount of time the trapping beams are shut off.

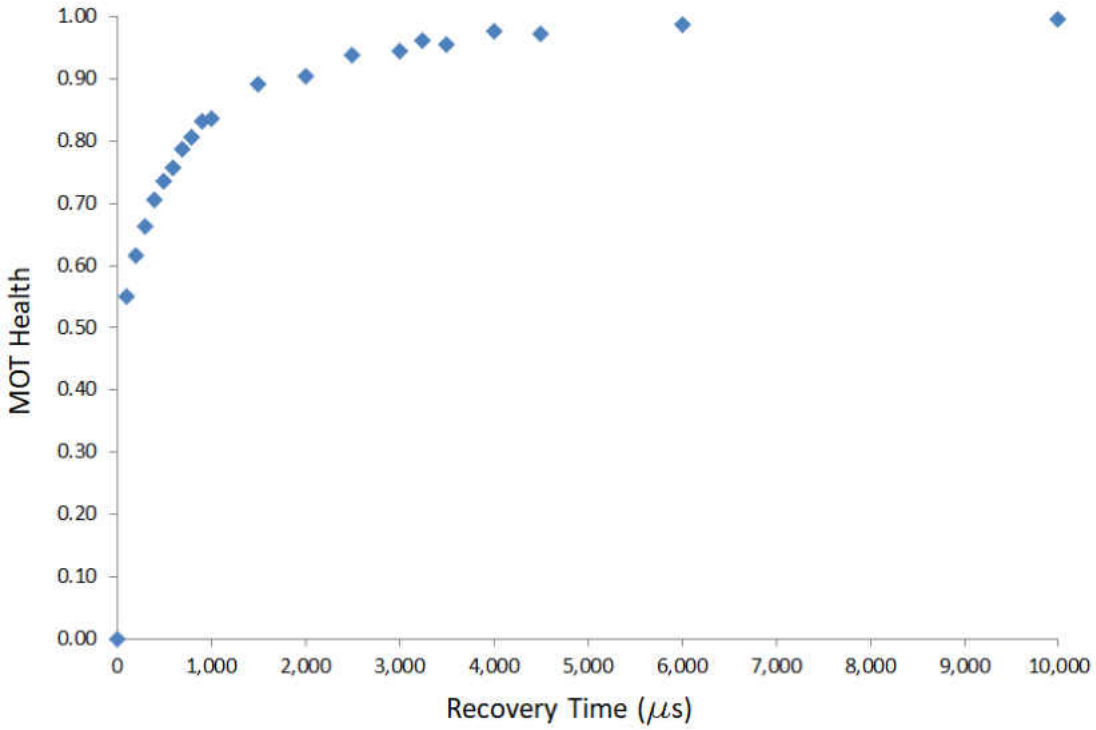

FIG. 69: A plot showing MOT health while spanning a range of Phase 3 recovery times. This data set was taken at an intensity of 780 mW/cm^2.

equipment is functioning properly even after many modifications and improvements, and gives us confidence as we move into previously uncharted waters.

We present two figures. Figure 70 shows $Ar^* + Ar^*$ photoassociation spectroscopy recently performed across a range of PA laser intensities using the newly modified apparatus. The scans shown are from single runs as opposed to composites assembled out of multiple separate runs. Figure 71 also shows $Ar^* + Ar^*$ photoassociation spectroscopy performed across a range of PA laser intensities. The figure displays a composite data set assembled from multiple scans performed by the previous graduate student, Maha Omar. Omar's scans are taken under similar overall conditions as the recent ones, and the complete data set and description may be found in her dissertation [3]. Comparing the two sets, we see that we have the same broad features over the same ranges and have successfully replicated the previous work.

However, there is one difference between the two data sets. When determining PA laser intensities, Omar calculated the theoretical focal point diameter of her beam to be 90 μm. Unless carefully removed with a multi-optic system, spherical aberrations and other distortions will often prevent theoretical focus widths from being realized via a single lens. Instead of relying on a calculation, we used a WM100 Omega meter to experimentally measure the width of our focal point, and we determined it was actually 350 μm. In Fig. 70, we have listed the experimentally determined intensities above each run. For making comparisons between the two data sets, in parentheses we have included what the intensity would have been calculated to be if we had used the theoretical focus size instead of the experimental one.

6.1.5 EXAMPLES OF SINGLE SCANS

Figures 72 and 73 are examples of a typical single scan when the plasma is stable. They show the ion count data from the Channeltron and the 780 nm fluorescence data from the PMT, respectively. This particular run was taken when the PA laser had an intensity of 780 mW/cm^2, and with no Rb MOT present. In Fig. 72, the dark red line is the PA data taken during Phase 2, and the faint red line is the MOT health and background data taken during Phase 1.

Studying this example, broad photoassociative spectra from $Ar^* + Ar^*$ interactions dominate the ion count data. As the photoassociation laser moves closer to resonance, the number of available atom pairs continues to increase, resulting in molecular excitation and higher ion production. Around -1 GHz, the PA laser scans

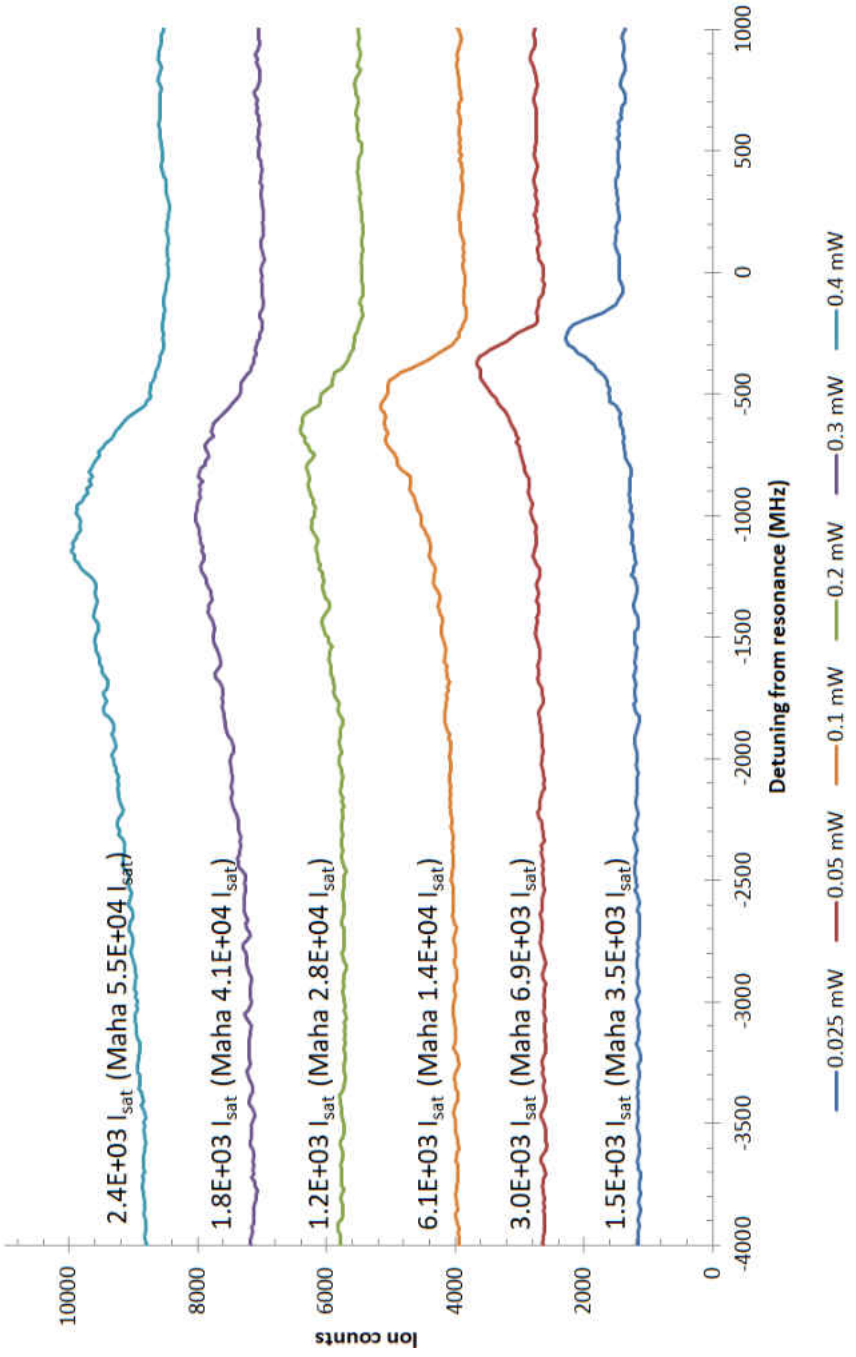

FIG. 70: A plot of photoassociatve spectra over a range of intensities, taken on our updated apparatus. These specific data sets are all single runs taken on the same day. These runs were performed to verify that we could replicate work done by the previous graduate student.

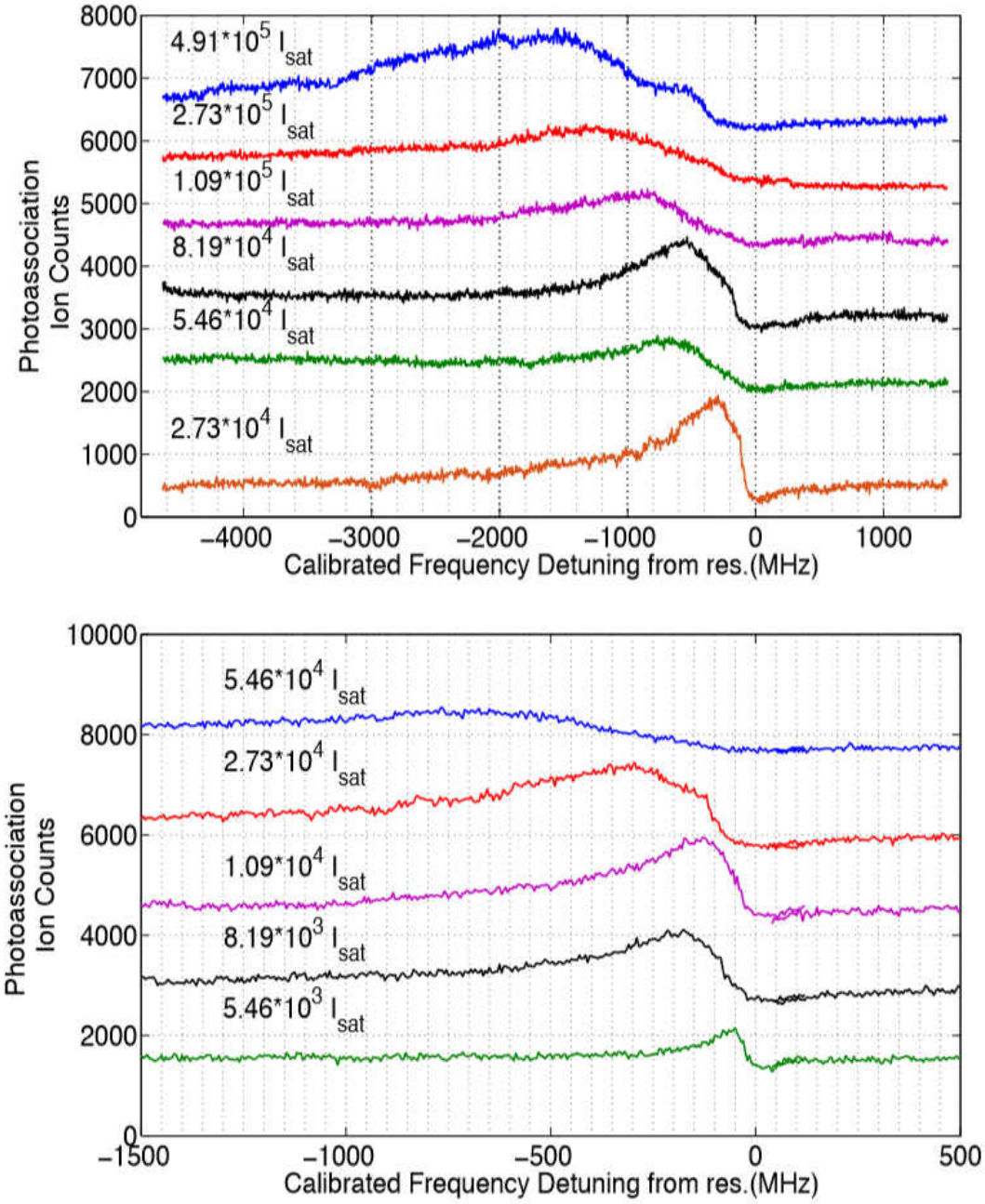

FIG. 71: Two plots displaying data taken from the previous work within the group [3]. They show photoassociative spectra for a range of PA laser intensities. The data shown is a composite of many scans taken and averaged together.

closely enough to resonance that it starts to damage the Ar^* MOT density, suddenly and dramatically reducing the number of atom pairs available. The background has been stable up until this point, implying that the plasma has remained in the same mode the entire run. The stable background also implies that any features observed in the Phase 2 data are most likely from molecular spectra. When the laser has a detuning of 0 MHz, it completely extinguishes the Ar^* MOT, and we see that the background ion production is about 1200 per point. This corresponds to around 9000 ion counts per second from the plasma background, which is on the higher side. However, this is not a problem as long as the plasma remains stable. Studying the fluorescence data for this particular scan is less interesting. The Rb MOT will not be damaged by the PA laser unless it is scanning over a range where Rb and Ar^* atoms may be excited into molecular state, so generally we expect it to look flat. The scan shown in Fig. 73 is representative of results from a typical scan. Ideally, we hope for peaks to appear at a PA laser detuning that corresponds to a simultaneous change in ion production.

Figure 74 shows us what happens when the plasma is unstable. This scan was taken at the same intensity, earlier the same day as the previous figures while we were working to stabilize the plasma. Upon first glance, one might mistakenly believe that in addition to the broad feature, narrow features are appearing between -4 GHz and -2 GHz. However, each of these "features" also appears in the Phase 1 background data, signifying that they came from background fluctuations. In other scans, fluctuations have manifested themselves as long, gentle slopes that have the potential to change the shape of broad $Ar^* + Ar^*$ spectra when averaged into the complete data set. A large amount of effort went into monitoring the background in real time and attentively stabilizing the plasma each day.

6.1.6 ION COUNT RESULTS

In this subsection, we present the Rb + Ar^* ion count net results from photoassociation spectroscopy performed over a range of PA laser intensities: 78 mW/cm^2 (Figure 75), 390 mW/cm^2 (Figure 76), 780 mW/cm^2 (Figure 77), and 3900 mW/cm^2 (Figure 78). At each power, scans were run repeatedly to build up statistics and average out fluctuations. The total number of scans for each figure ranges from 12 the case of 79 mW/cm^2, to 28 in the case of 790 mW/cm^2. These figures represent months of data collection.

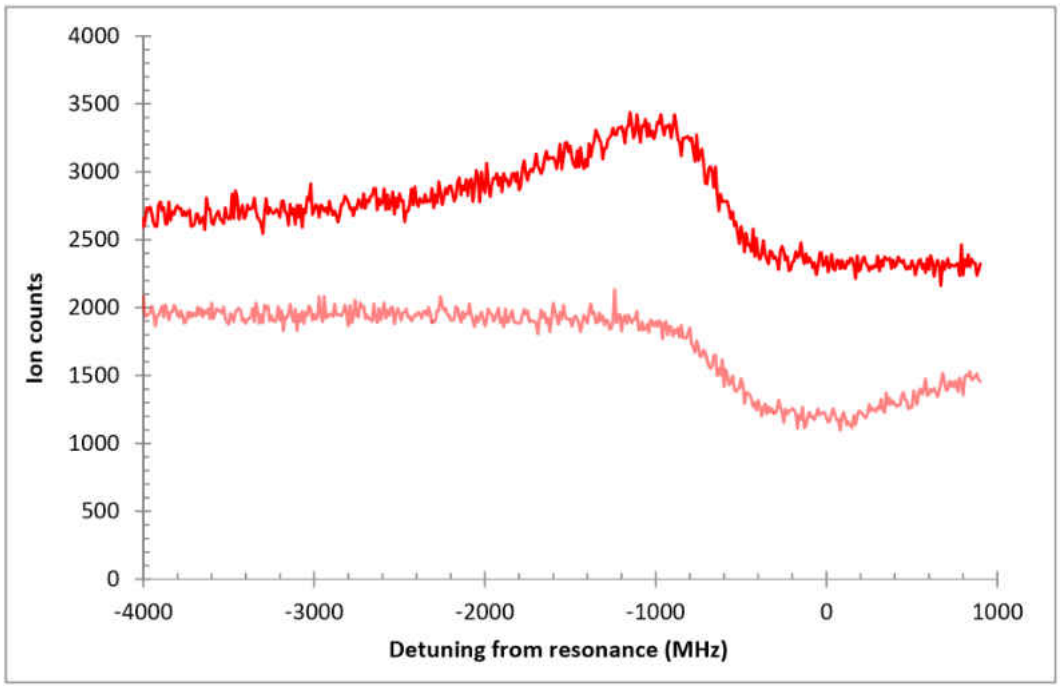

FIG. 72: A plot showing ion data from a single scan with plasma stable and the PA laser well aligned. The dark red is taken during Phase 2 of the timing cycle, when the trapping lasers are turned off and the PA laser is turned on. The faint red line is a measure of the MOT health and plasma stability, taken immediately before each PA data point when the trapping light is still present.

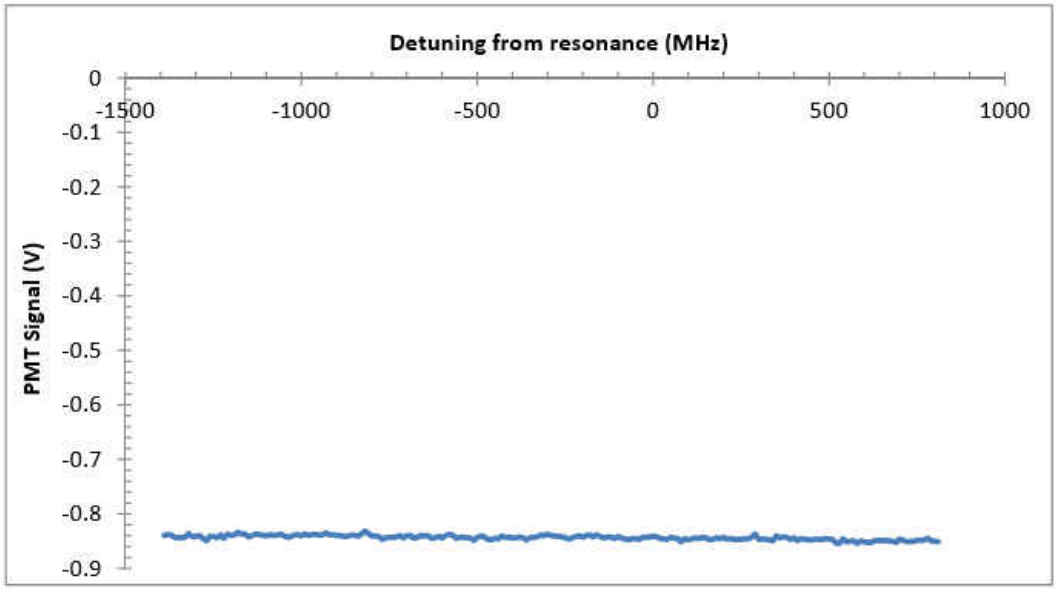

FIG. 73: A plot that is representative of typical fluorescence data when both the plasma and the MOTs are stable.

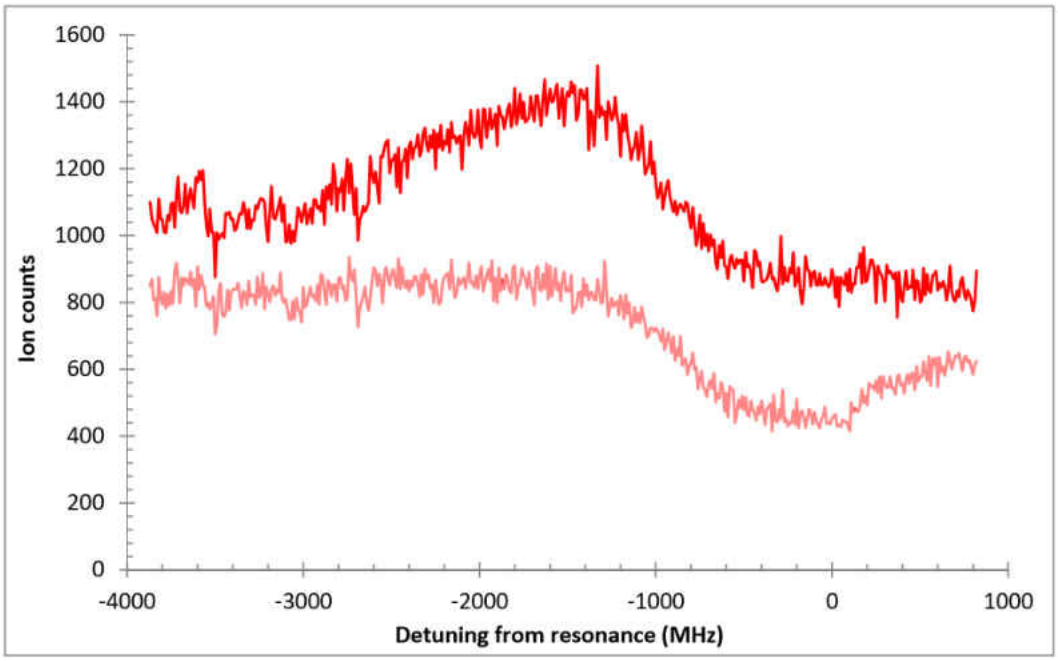

FIG. 74: A plot showing ion data from a typical scan when the plasma is unstable. The dark red is taken during Phase 2 of the timing cycle, when the trapping lasers are turned off and the PA laser is turned on. The faint red line is a measure of the MOT health and plasma stability, taken immediately before each PA data point when the trapping light is still present. Quite clearly we see that fluctuations in the background show up in the Phase 2 PA data, and could easily be mistaken for real features.

The data set was taken while the PA laser scanned continuously at a rate of 2.5 MHz/s. Each data point represents the total number of ions detected over a 10 MHz range, giving us the resolution to detect features with spectral widths of only a few 10's of MHz. We have high confidence in the overlap of both MOTs, as seen by the excess ion counts, and equally high confidence in the overlap of the PA laser, as shown by the large $Ar^* + Ar^*$ photoassociative spectra.

Surprisingly, an examination of the scans does not reveal any features that might suggest molecular excitation involving Rb. Photoassociative spectra from $Ar^* + Ar^*$ interactions are easily distinguished. In every case, the spectra taken with the Rb MOT present (shown in green) are nearly identical to the spectra taken without the Rb MOT (shown in blue). The only difference is a small, nearly constant offset between the two that vanishes at resonance. Any small dips or spikes may all be accounted for in the background data, or from single, large, unrepeatable peaks in one of the many scans making up the data set.

There is a possibility that like the Ar data, the vibrational features are so closely overlapped that it is impossible to distinguish them. In that case, RbAr spectra over this range would appear as large broad features similar to the $Ar^* + Ar^*$ spectra. This result could manifest itself as a subtle difference in shape between the two sets of scans at each power. To search for small, yet broad, distortions, a residual analysis was performed, and may be seen in blue on the lower plot of each figure. Again, a careful examination of the residuals does not reveal any sign of molecular excitation involving Rb. We note that Figs. 76, 77, and 78 all show a dip on the right-hand side of the graph. Each of these dips is the result of a case where either the Ar^* or Rb MOT trapping lasers broke lock near the end of the scan. This might give the appearance that our trapping lasers tended to break lock near that same PA laser detuning. This is in fact not the case. They were equally likely to break lock anywhere; however, when this occurred earlier in a scan or over a region of key interest, the scan would subsequently be halted.

A small peak appears in the residual data of Fig. 75, the 79 mW/cm^2 data set, over the same frequency range corresponding to the steepest part of the slopes above. However, we strongly suspect that this is an artifact. In subsequent scans using Experimental Method 2, we were unable to duplicate the result. As the scans became lower power, the damage to the MOT occurred over a smaller range, resulting in much steeper slopes. We suspect that small errors in aligning the scans caused an

effect similar to that discussed in 6.2.2. High power scans had shallower slopes, and would be as vulnerable to similar small uncertainties.

We found the behavior of the excess ion counts to be the most interesting aspect of this data set. Near resonance, as the PA laser damages the Ar^* MOT and lowers densities, we see the excess ion counts completely disappear, reinforcing the idea they the counts come from collisions between Rb and metastable Ar. However, throughout the rest of the scans, the rate of Rb-dependent excess ion counts remains constant, regardless of PA laser tuning. The lack of dependence raises a number of questions, and is investigated more in Section 6.3.

6.1.7 CIRCULARLY POLARIZED PA LIGHT

In addition to the scans previously described, which utilized linearly polarized light, we also performed a set of scans using circularly polarized light. In this test, the PA laser was scanned at the same 2.5 MHz/s as the previously displayed data, and its intensity was set to 780 mW/cm^2. A $\lambda/4$-waveplate was optimized to produce σ^+ polarization, and placed in PA laser beam as it entered the science chamber. Sixteen scans were performed, and the ion counting results can be seen in Fig. 79 and the fluorescence results can be seen as part of Fig. 81. Again, $Ar^* + Ar^*$ photoassociation was readily visible in the data, and again there was no sign of photoassociation involving $Rb + Ar^*$.

6.1.8 HIGH POWER

Our highest power scan had an intensity of 16,000 mW/cm^2, and scanned to 8.25 GHz below resonance. The high power results can be seen in Fig. 80. At this large detuning, the time required to produce a single scan exceeded the typical length of time that the plasma would remain stable. This made it exceedingly difficult to complete scan at this power. In fact, after many attempts, we were only able to produce one successful high power $Rb + Ar^*$ scan. Without a pair of homonuclear/heteronuclear scans, we were unable to perform a residual analysis. However, the completed high power scan is stable and shows no sign of any excited molecular structure. In a comparable heteronuclear PAS experiment performed at similar densities to ours, J. Shaffer et al. saw clear structure within 1 GHz of resonance. The spectra they produced can be seen in Fig. 2. Given these results and the large effort required to perform high power scans, we decided that it would likely be more

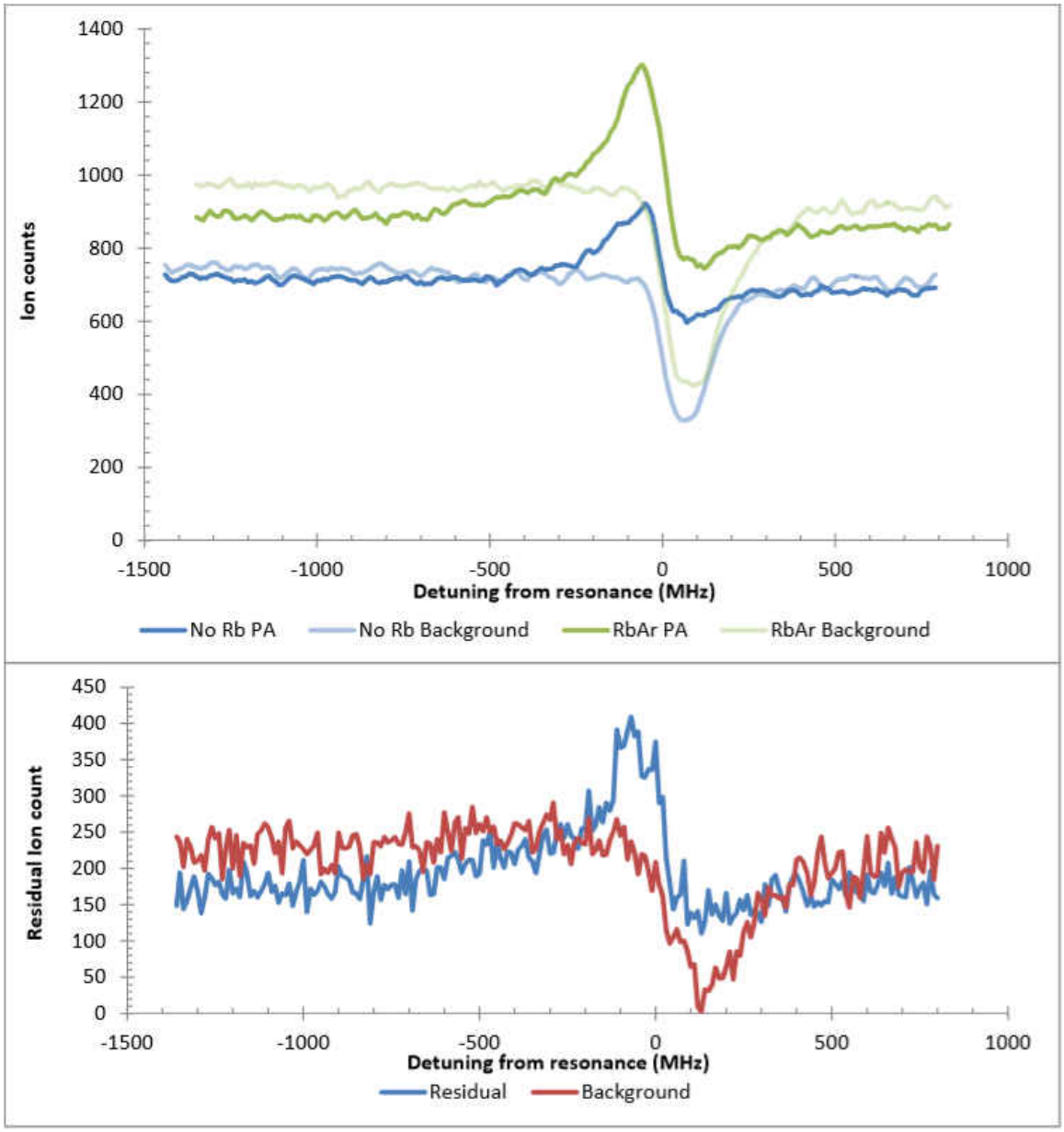

FIG. 75: These graphs are the final output with a 78 mW/cm^2 intensity PA laser. The upper graph is the average of every run, and the lower graph is the residual analysis. We do not believe that the blue residual peak is real. Its location coincides with the steepest portion of the slopes above it, and we suspect that it is a result of frequency uncertainties introducing a phase shift to the data. The "feature" is not seen at higher powers where the slope is less steep.

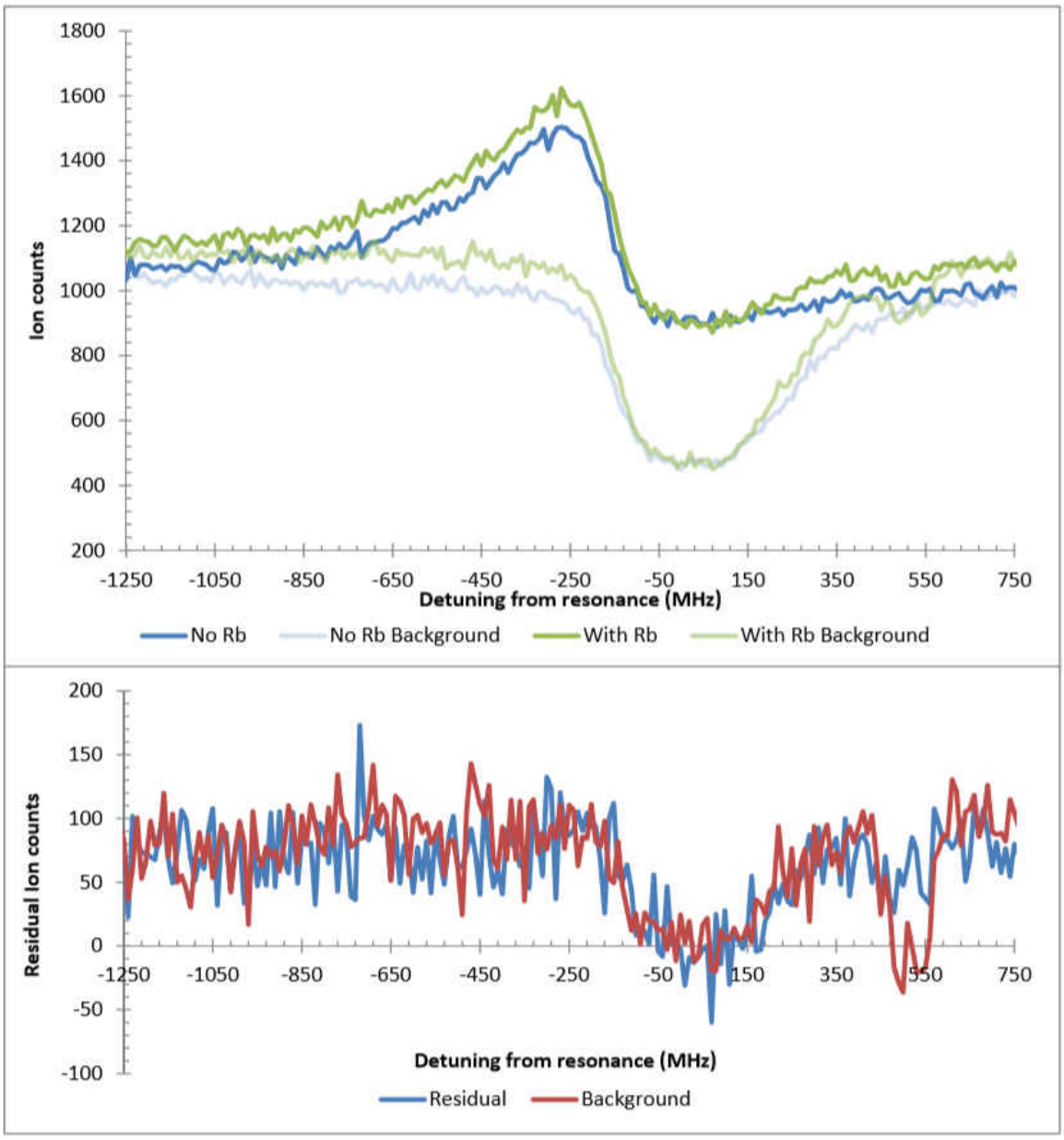

FIG. 76: These graphs are the final output with a 390 mW/cm^2 intensity PA laser. The upper graph is the average of every run, and the lower graph is the residual analysis.

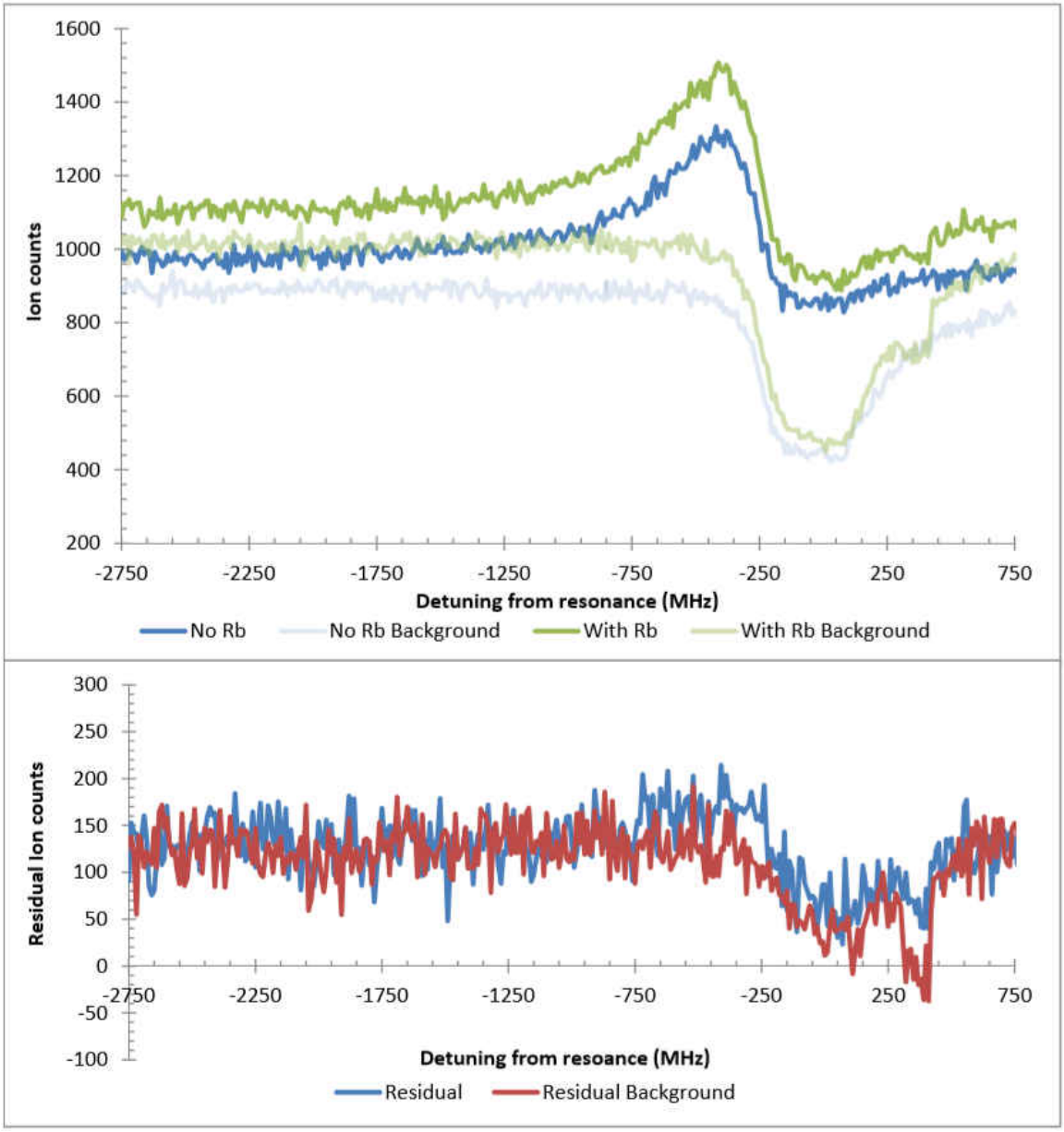

FIG. 77: These graphs are the final output with a 780 mW/cm^2 intensity PA laser. The upper graph is the average of every run, and the lower graph is the residual analysis.

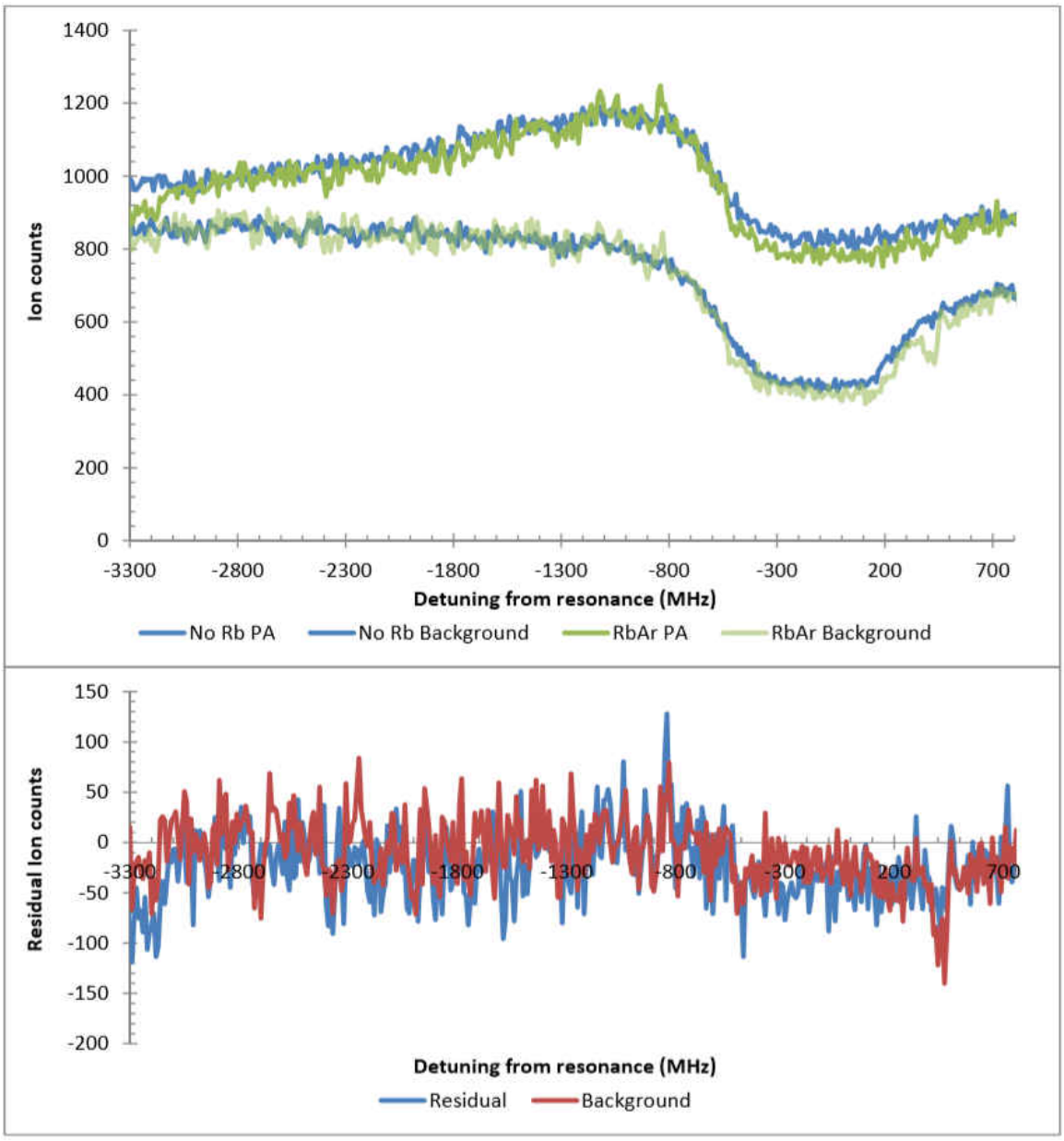

FIG. 78: These graphs are the final output with a 3,900 mW/cm^2 intensity PA laser. The upper graph is the average of every run, and the lower graph is the residual analysis.

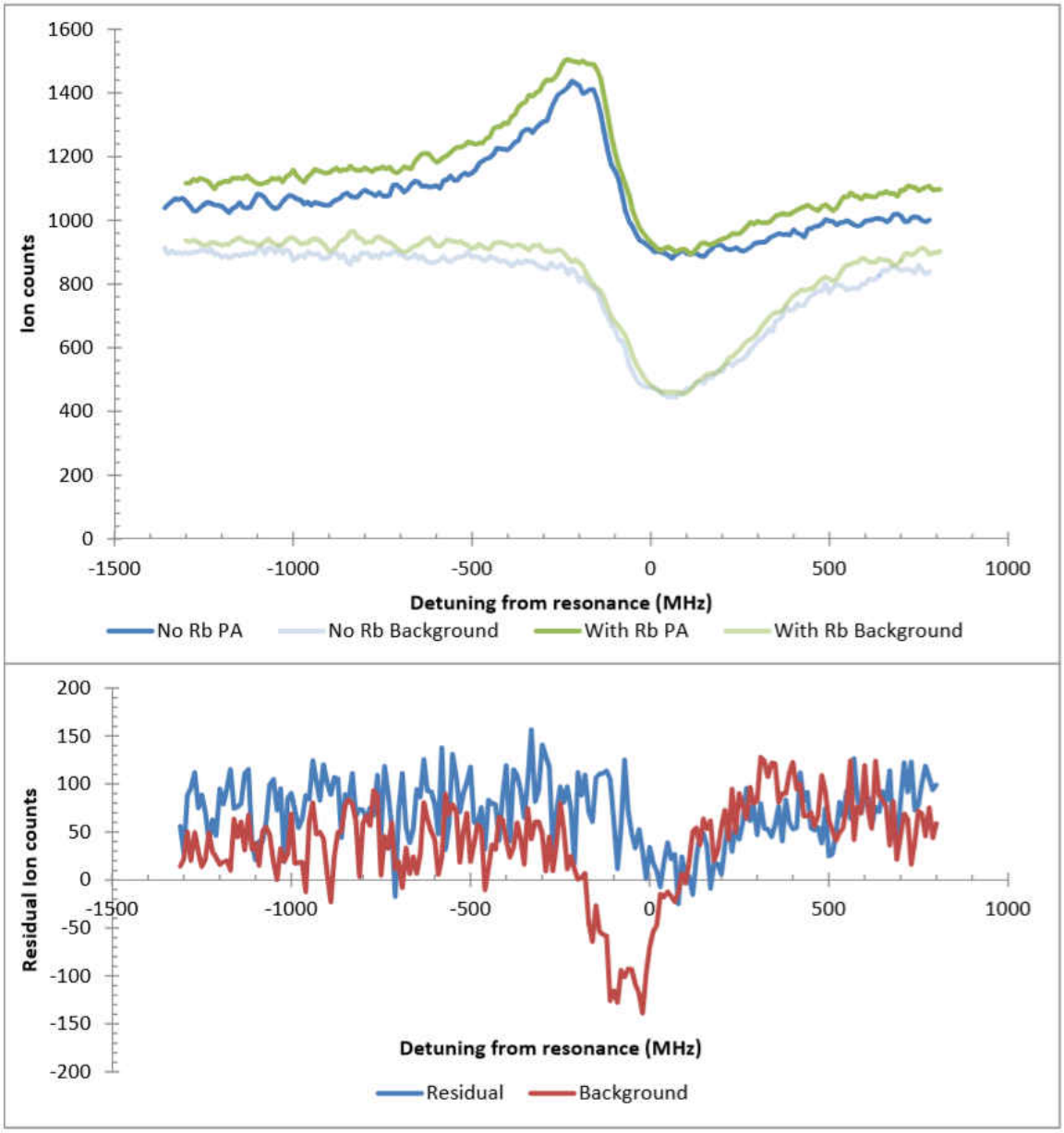

FIG. 79: These graphs are the final output of all the scans from when the PA laser was circularly polarized. The scans were taken with a PA laser intensity of 780 mW/cm^2. The upper graph is the average of every run, and the lower graph is the residual analysis.

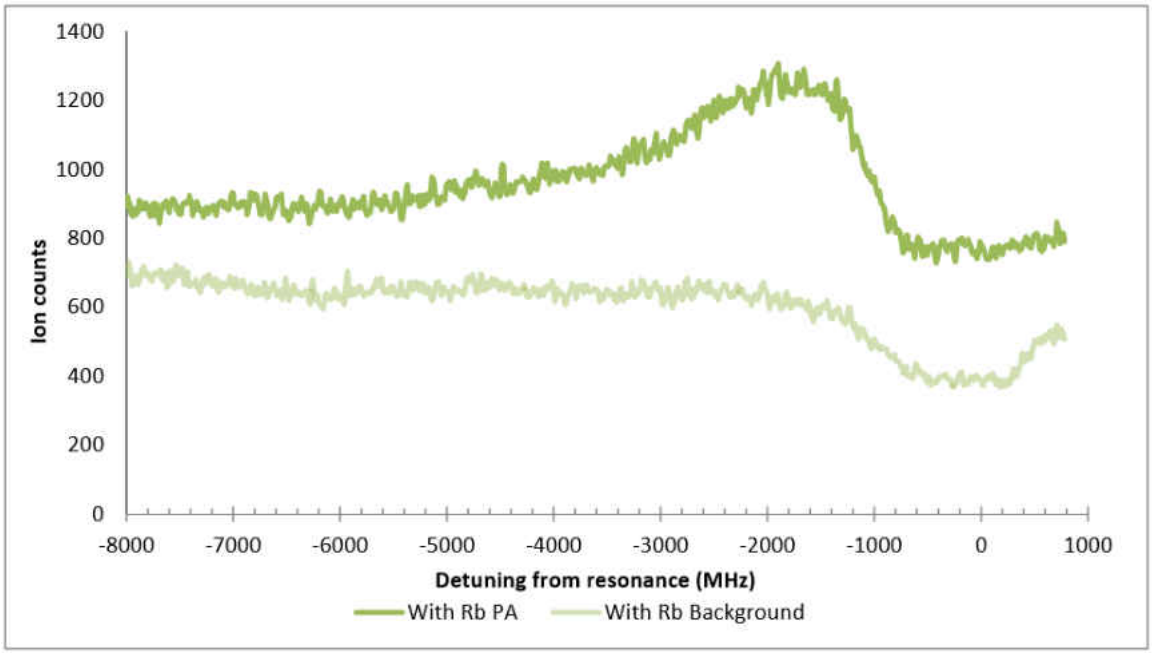

FIG. 80: This graph is the final output with a 16,000 mW/cm^2 intensity PA laser.

fruitful to continue our search at lower powers. We have a few ideas to improve our ability to scan further out, and they are discussed in Chapter 7.

6.1.9 PMT FLUORESCENCE DATA

Spectroscopic fluorescence data is presented in Fig. 81. The data presented is averaged together from each run performed at the specified intensity. Other than combining the runs and changing the offsets so that they will all appear on the same graph, the fluorescence data is raw. As the PMT's output is negative, trap loss will appear as a positive spike on this graph. An examination of that data yields no sign of Rb trap loss. This is consistent with experimental results from ion detection.

6.1.10 CONCLUSIONS FROM EXPERIMENT 1

After examining months worth of data from Experiment 1, we were surprised to find no sign of any Rb + Ar* photoassociation. With our resolution, we would have been able to detect features as narrow as a few 10's of MHz, either by ion or fluorescence detection. Equally surprising was the determination that the Rb + Ar* PI and AI counts were independent of the PA laser tuning. While slightly disappointed

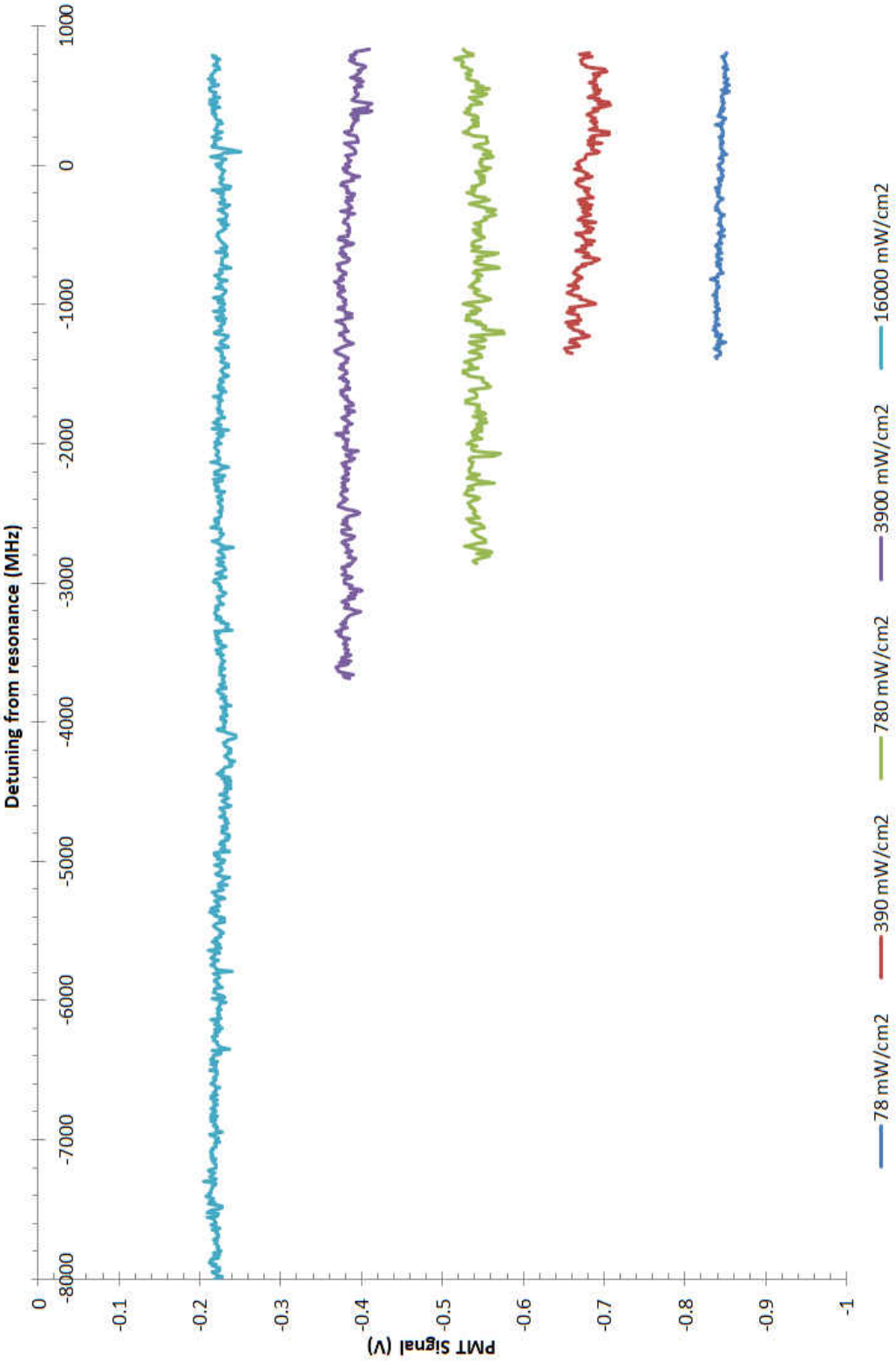

FIG. 81: A plot showing the net PMT data from all the scans. The data measures Rb MOT fluorescence, and trap loss would appear as a peak.

not to have found any structure, we started this experiment understanding that photoassociation spectroscopy is a region of interest where experimental progress tends to lead theoretical progress. In this case, we seem to have found more questions than answers. A tremendous amount of effort was required to maintain stable plasma and MOTs, however fluctuations still made it very difficult to scan over large ranges. In our next experiment, we implemented a new timing scheme in hopes of being less susceptible to fluctuations in the RF plasma discharge.

6.2 SECOND EXPERIMENT OVERVIEW

Experiment 1 produced two unexpected results. We did not see any evidence of RbAr photoassociation, and we detected ion production from Rb + Ar^* collisions that was independent of PA laser tuning (except when the PA laser obliterated the Ar^* MOT). We implemented a redesigned timing scheme that we hoped would be less vulnerable to changes in the plasma. Instead of repeating scans and slowly building up a heteronuclear data set, and then again slowly building up a homonuclear data set, we would interlace the two into a single process. The hope being that any changes in plasma ion production would show up identically in both sets, and be subtracted out in the residual analysis. With this new scheme, we set out to confirm or refute the results from Experiment 1.

We modified the LabView data acquisition code to send out a TTL analog signal, which was sent to the pulse generator controlling all of the timings. When the TTL was high, the Rb MOT trap lights would be shut off, and when the TTL was low, the Rb MOT would reload. With this new capability, we could interlace Rb + Ar^* PA measurements with heteronuclear Ar^* PA measurements, and take residual data from a single scan instead of two.

6.2.1 SECOND EXPERIMENT TIMING

In our new timing scheme, the core data-taking cycle remained unchanged from the first experiment. Phase 1 is again a 100 μs period to measure the MOT health and background. Phase 2 is again a 200 μs period where the trap light is shut off and the PA laser is turned on. And Phase 3 is again a 2800 μs recovery period for the MOTs to reload after trap loss. These three phases are continuously repeated 3333 times to form a single data point. The core data cycle is still well described by Fig. 65, where:

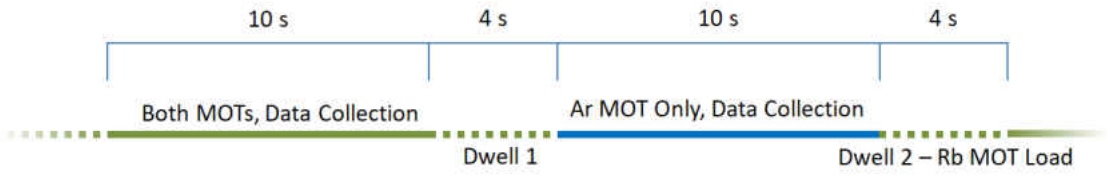

FIG. 82: A diagram of the data collection cycle for Experiment 2. Data is collected when the lines are solid, and the Rb MOT is turned off where the line turns blue. One complete cycle provides two data points.

1. Phase 1 - MOT health measurement,
2. Phase 2 - PA measurement,
3. Phase 3 - MOT recovery time.

However previously we either took an entire scan with both MOTs present, or with just the Ar* MOT present. In our new methodology, we take one data point with the Rb MOT, then one data point without the Rb MOT, alternating back and forth the entire time. The benefit is that both sets of data will inherently share any plasma fluctuations, ideally allowing us to subtract out that source of noise.

1. Take data with both Rb and Ar* MOTs (10 seconds),
2. Dwell time, Ar* MOT remains and Rb is shut off (4 seconds),
3. Take data with only the Ar* MOT (10 seconds),
4. Dwell time, Ar* MOT remains, Rb MOT turns on and fully loads (4 seconds).

In between the each pair of data points, four seconds had be left to allow for the Rb MOT to fully reload after having been shut off. Unfortunately, firmware restrictions within our hardware forced us to include another dwell time as shown in Fig. 82. To keep from having a data collection duty cycle of 50%, we lengthened our data collection period from 4 seconds in Experiment 1, to 10 seconds in Experiment 2. While this results in fewer data points overall and a reduced resolution, we find this an acceptable trade-off, because Experiment 2 is only looking for broad features. The first experiment was very capable of detecting any smaller features by itself.

6.2.2 REMOVING THE PHASE SHIFT

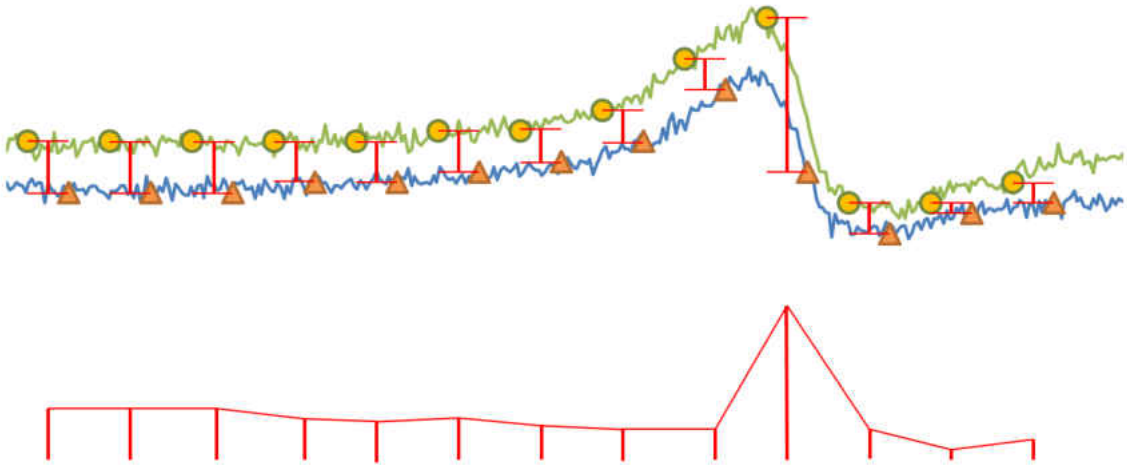

FIG. 83: An exaggerated illustration of how a phase shift between the two sets of data can cause a fake peak in the residual. We have superimposed a series of circles and triangles on top of the composite data for 780 mW/cm^2 intensity from Experiment 1. The red line shows the difference between each pair. Below, we have centered and collected the red lines to see what a residual between the two sets would look like if uncorrected.

The long integration times in Experiment 2 introduce a subtle problem. Each residual data point is the difference between two 10-second data points. The PA laser continuously scans at a rate of 1.4 MHz/second throughout the entire run, so these two 10-second data points are in fact taken 19.6 MHz apart. This introduces a phase shift, and over frequency ranges where the slope is steep will create an artificial peak very similar to the peaks we purposely created when phase-locking our lasers. This effect is shown in Fig. 83. However, in the figure, the midpoint between each pair of triangles is perfectly lined up with the circle above, and we may use that to our advantage. For each data point in the Yes-Rb-MOT data set, we may estimate a corresponding No-Rb-MOT data point by finding the midpoints between the No-Rb-MOT points. Doing this replaces the artificial peak at the steepest part of the slope with a resonant dip around zero detuning.

6.2.3 RESULTS FROM EXPERIMENT 2

Results from Experiment 2 may be seen in Fig. 84. It is a composite of 12 scans

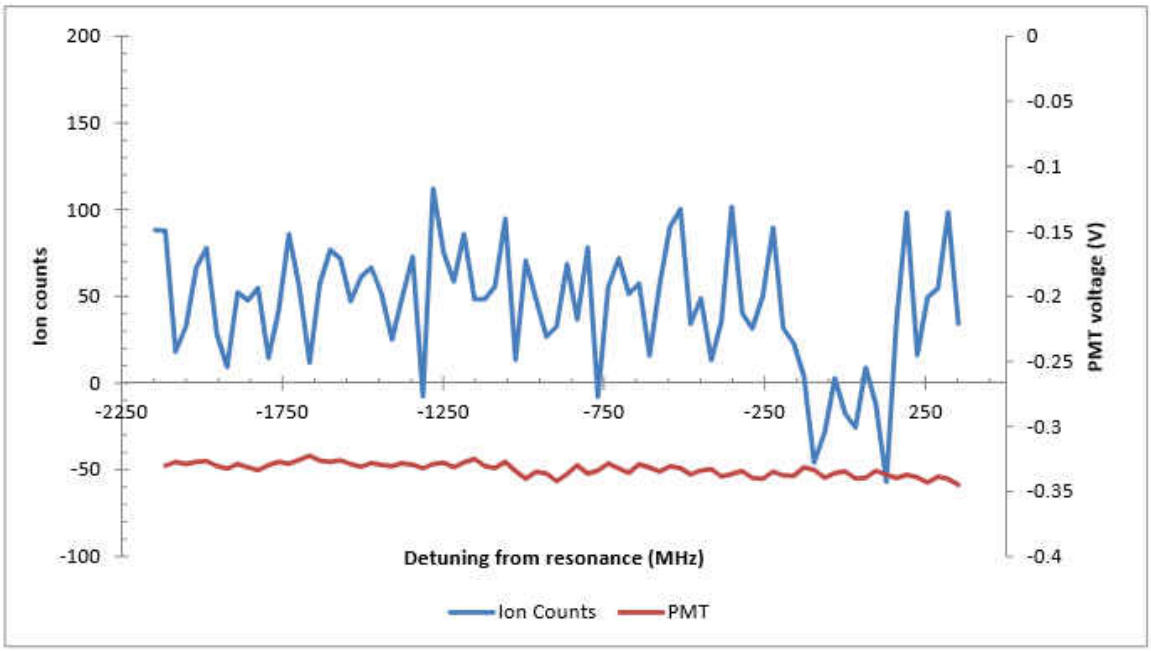

FIG. 84: A plot showing the results from Experiment 2.

completed using the new timing scheme. We were able to replicate the Experiment 1 results for the 780 mW/cm^2 intensity. There were no features that could be attributed to Rb + Ar* photoassociative interaction. However, we again found an increase in ion production associated with the presence of the Rb MOT, independent of the PA laser tuning. The fluorescence measurements showed no sign of any trap loss at any point of the scans. Time constraints kept us from completing scans at more powers, but we were pleased to have successfully confirmed our previous results.

6.2.4 CONCLUSIONS FROM EXPERIMENT 2

The primary outcome of Experiment 2 is confirmation of the results from the first experiment. Once again, Rb-required excess ion counts were present and constant at all PA laser tunings, except near resonance. Secondly, it had been hoped that by interlacing Rb/No-Rb measurements, we would inoculate the results from plasma fluctuations. While it is true that distortions from plasma fluctuations were reduced, the added loading time between data collection periods reduced our ability to fully remove fluctuations. Any background changes that happened faster than 10 s to 15 s were too fast to be removed. The length of data collection periods is a delicate

balance. If they are too short, we have a very low active duty cycle, because it is still necessary to load the Rb MOT for four seconds each data point. With lower total counts built up, our data becomes vulnerable to the random fluctuations that are inherent in ion counting experiments. If the data collection periods are too long, we lose much of our ability to remove plasma fluctuations. Finally, the longer time per data point makes large-detuning scans take an unreasonably long amount of time when compared with the average length of MOT stability. We have come to the conclusion that the only way to scan out at longer distances is to make some significant changes to the apparatus, which are discussed in the next chapter.

6.3 DISCUSSION OF EXCESS ION COUNTS

As mentioned above, the Rb-required excess ion counts were unexpected. While we did expect ion production to be changed by the presence of the Rb MOT, we also anticipated that this change would be highly dependent on the PA laser tuning. In a final experiment to shed some light on their source, we tried to determine if they came from ground state collisions, excited state collisions, or some combination.

To some extent, we could control what proportion of the atoms are in ground state with the trapping beams. When the trapping lights are on, around 40% of the atom population is in the excited state at any given time. When either of the trapping lights are turned off, their respective atom population relaxes into the ground state within a few tens of nanoseconds. We measured the excess ion count rate when 1) both atom populations were in the ground state, 2) when the Ar^* atoms were all ground state and the Rb trapping light was on, 3) when the Rb atoms were all ground state and the Ar^* trapping light was on, and 4) when both sets of trapping beams were on.

Both MOTs were well overlapped using the procedure described in Section 5.4. Ion production was measured for 10 seconds while both MOTs were fully formed, and then measured again with just the Ar^* MOT. The cycle was repeated 15 times for each of the four conditions listed above. At no time was the PA laser involved.

- All atoms in ground state: 290±70 counts/s
- Ar trap beams on, Rb in ground state: 437±138 counts/s
- Ar in ground state, Rb trap beams on: 304±79 counts/s

- Both Trap beams on: 420±92 counts/s

These data suggest that a large portion of the excess ion counts come from ground state collisions between Ar^* and Rb, but that the collision rate may be increased by exciting Ar from an S orbital to a P orbital. This outcome introduces a new question: If the trapping beams can increase excess ion production, why didn't the PA laser? The experimental data was thorough and quite clear: excess ion counts are not dependent on PA laser tuning. We feel that there is likely an interesting mechanism at work, and that it warrants further study.

CHAPTER 7

CONCLUSIONS AND PROSPECTS FOR THE FUTURE

7.1 CONCLUSIONS FROM THE METASTABLE Kr STUDY

Three methods of all-optical Kr^* excitation were investigated. We demonstrated Kr^* production with 193 nm light pulses from an ArF excimer laser and found the efficiency to be in line with our calculations. However, it was determined that this method was too resource intensive to be realistically applied to ATTA. We showed that the JLab FEL is not a sensible choice for RF discharge replacement. As mentioned previously, while investigating the UV lamp as a source of high energy photons, funding considerations compelled us to divert our efforts to the photoassociation spectroscopy work that makes up the second part of this dissertation. However, before the transition to PAS, we developed several detection schemes and our calculations showed that UV lamp excitation is a particularly promisng method. This is highlighted by the fact that several other research groups have been using their own versions of the UV lamp excitation method [13][18]. In post-experimental analysis, we believe we correctly identified the primary issue that prevented us from detecting Kr^* atoms with the UV lamp. New measurements of the Kr^* collisional cross section show that our atoms' mean free path was likely shorter than we had originally calculated. As a result, we believe Kr^* atoms were successfully excited, but were collisionally quenched before they could be detected.

As of the time of writing this dissertation, work is underway on a new UV lamp experiment. To avoid the peril of Kr^* atoms collisionally quenching before being detected, current work is being undertaken within a cell, and relies on detection of the 760 nm decay photon. An optical build-up cavity has been constructed around the cell to provide even higher efficiency 819 nm excitation. We hope to see measurable results soon.

7.2 CONCLUSIONS FROM PHOTOASSOCIATION SPECTROSCOPY OF RbAr

We completed a search for RbAr molecular excitation via photoassociation just below the Ar^* $4p[5/2]_3$ + Rb $5^2S_{1/2}$ asymptote. Surprisingly, the search did not find any evidence of excited state molecular production. In post-experimental analysis, we discussed the idea that perhaps the MOTs were not dense enough, as the photoassociation rate scales with density squared. However, this would not be a trivial explanation to probe. Penning ionization scales with density squared, making it impossible to make metastable species MOTs that are as dense as those made from a species with fewer collisional losses. We know of at least one case where a FORT temporarily increased the density of a metastable MOT for short periods of time, allowing for recovery, but this is a large undertaking in its own right. A second possibility is that our detection was not sensitive enough. Fluctuations in ion production within the atomic beam might have masked a small signal. There is also the possibility that the excited molecular potential does not allow for PI and AI detection. A very flat excited molecular state might fail to accelerate the atoms enough before they decay back down. We are confident that there was no problem with the overlap of our PA laser with the MOTs, because of the clear Ar^* + Ar^* excitation. We also are confident in the overlap of the two MOTs with each other due to the 1) cameras, 2) measured trap loss, and 3) excess ion counts. These excess ion counts warrant further exploration. Before the experiment, we would have expected any Rb-required ion production to be dependent on PA laser tuning. The fact that excess ion production was flat over many GHz suggests that there is more about our system to explore.

While this work left us with new questions, we have a number of interesting future prospects. We would prioritize removing background ion counts from the RF discharge. A second pair of deflection plates further downstream would likely accomplish this. Instead of relying on PI and AI to produce detectable ions, we might add an additional laser to ionize directly out of the excited molecular state, thereby bypassing any problems from excited molecular states not enabling small internuclear separations. We might also make significant changes to the science chamber to improve fluorescence detection. Installing a large lens inside the chamber would increase the collection solid angle, and adding beam blocks and a baffle system may reduce scattered light from the Zeeman slower. Finally, as we have previously

stated, we believe that the excess ion counts we detected warrant further study. With our current ion detection, we cannot tell the difference between Ar^+, Rb^+, Ar_2^+, Rb_2^+ or $RbAr^+$. Reinstalling a quadrupole mass spectrometer to differentiate between these species is an excellent place to start.

BIBLIOGRAPHY

[1] M. Shaffer, "Photoassociative spectroscopy of ultracold metastable argon and study of dual species trap loss in a rubidium-metastable argon mot," Ph.D. thesis, Old Dominion University (2008).

[2] H. Busch, "Experimental investigation of a rubidium-argon dual species magneto-optical trap," Ph.D. thesis, Old Dominion University (2004).

[3] M. Omar, "Photoassociative spectrosocpy of ultracold argon and krypton confined in a magneto optical trap," Ph.D. thesis, Old Dominion University (2015).

[4] C. Faunt, R. Hanson, and K. Belitz, "Groundwater availability of the Central Valley aquifer, California," Tech. rep., United States Geological Survey (2009).

[5] P. Collon, W. Kutschera, and Z.-T. Lu, "Tracing noble gas radionuclides in the environment," Annu. Rev. Nucl. Part. Sci. **54**, 39–67 (2004).

[6] W. F. Libby, "Radiocarbon dating," Science **133**, 621–629 (1961).

[7] L. Plummer and P. Glynn, *Isotope Methods for Dating Old Groundwater* (Vienna, Austria: IAEA, 1992).

[8] Z.-T. Lu, "Radiokrypton dating coming of age," National Science Review **3**, 172–173 (2015).

[9] J. R. Arnold, "Scintillation counting of natural radiocarbon: I. the counting method," Science **119**, 155–157 (1954).

[10] D. Elmore and F. M. Phillips, "Accelerator mass spectrometry for measurement of long-lived radioisotopes," Science **236**, 543–550 (1987).

[11] C. Chen, Y. Li, K. Bailey, T. O'Connor, L. Young, and Z.-T. Lu, "Ultrasensitive isotope trace analyses with a magneto-optical trap," Science **286**, 1139–1141 (1999).

[12] N. Sturchio, X. Du, R. Purtschert, B. Lehmann, M. Sultan, L. Patterson, Z.-T. Lu, P. Müller, T. Bigler, K. Bailey *et al.*, "One million year old groundwater in the Sahara revealed by krypton-81 and chlorine-36," Geophysical Research Letters **31**, L05503 (2004).

[13] J. Zappala, "Atom trap trace analysis: Developments & applications," Ph.D. thesis, The University of Chicago (2017).

[14] C. Chen, K. Bailey, Y. Li, T. OConnor, Z.-T. Lu, X. Du, L. Young, and G. Winkler, "Beam of metastable krypton atoms extracted from a rf-driven discharge," Review of Scientific Instruments **72**, 271–272 (2001).

[15] X. Du, K. Bailey, Z.-T. Lu, P. Mueller, T. O'Connor, and L. Young, "An atom trap system for practical ^{81}Kr dating," Review of Scientific Instruments **75**, 3224–3232 (2004).

[16] L. Young, D. Yang, and R. Dunford, "Optical production of metastable krypton," Journal of Physics B: Atomic, Molecular and Optical Physics **35**, 2985–2992 (2002).

[17] Y. Ding, S.-M. Hu, K. Bailey, A. Davis, R. Dunford, Z.-T. Lu, T. OConnor, and L. Young, "Thermal beam of metastable krypton atoms produced by optical excitation," Review of Scientific Instruments **78**, 023103 (2007).

[18] H. Daerr, M. Kohler, P. Sahling, S. Tippenhauer, A. Arabi-Hashemi, C. Becker, K. Sengstock, and M. B. Kalinowski, "A novel vacuum ultra violet lamp for metastable rare gas experiments," Review of Scientific Instruments **82**, 073106 (2011).

[19] M. Dakka, G. Tsiminis, R. Glover, C. Perrella, J. Moffatt, N. Spooner, R. Sang, P. Light, and A. Luiten, "Laser-based metastable krypton generation," Physical Review Letters **121**, 093201 (2018).

[20] W. D. Phillips, "Nobel lecture: Laser cooling and trapping of neutral atoms," Reviews of Modern Physics **70**, 721–741 (1998).

[21] G. K. Campbell and W. D. Phillips, "Ultracold atoms and precise time standards," Philosophical Transactions of the Royal Society A: Mathematical, Physical and Engineering Sciences **369**, 4078–4089 (2011).

[22] P. Berg, S. Abend, G. Tackmann, C. Schubert, E. Giese, W. Schleich, F. Narducci, W. Ertmer, and E. Rasel, "Composite-light-pulse technique for high-precision atom interferometry," Physical Review Letters **114**, 063002 (2015).

[23] I. Bloch, J. Dalibard, and S. Nascimbene, "Quantum simulations with ultracold quantum gases," Nature Physics **8**, 267–276 (2012).

[24] E. B. Norrgard, "Magneto-optical trapping of diatomic molecules," Ph.D. thesis, Yale (2016).

[25] D. Egorov, T. Lahaye, W. Schöllkopf, B. Friedrich, and J. M. Doyle, "Buffer-gas cooling of atomic and molecular beams," Physical Review A **66**, 043401 (2002).

[26] L. D. Carr, D. DeMille, R. V. Krems, and J. Ye, "Cold and ultracold molecules: science, technology and applications," New Journal of Physics **11**, 055049 (2009).

[27] P. D. Lett, P. Julienne, and W. Phillips, "Photoassociative spectroscopy of laser-cooled atoms," Annual Review of Physical Chemistry **46**, 423–452 (1995).

[28] M. Santos, P. Nussenzveig, L. G. Marcassa, K. Helmerson, J. Flemming, S. C. Zilio, and V. S. Bagnato, "Simultaneous trapping of two different atomic species in a vapor-cell magneto-optical trap," Physical Review A **52**, 4340–4343 (1995).

[29] K. M. Jones, E. Tiesinga, P. D. Lett, and P. S. Julienne, "Ultracold photoassociation spectroscopy: Long-range molecules and atomic scattering," Reviews of Modern Physics **78**, 483–535 (2006).

[30] H. Busch, M. Shaffer, E. Ahmed, and C. Sukenik, "Trap loss in a dual-species Rb-Ar* magneto-optical trap," Physical Review A **73**, 023406 (2006).

[31] L. Byron, R. Dall, W. Rugway, and A. Truscott, "Suppression of Penning ionization in a spin-polarized mixture of rubidium and He," New Journal of Physics **12**, 013004 (2010).

[32] J. Schütz, T. Feldker, H. John, and G. Birkl, "Heteronuclear collisions between laser-cooled metastable neon atoms," Physical Review A **86**, 022713 (2012).

[33] J. Shaffer, W. Chalupczak, and N. Bigelow, "Photoassociative ionization of heteronuclear molecules in a novel two-species magneto-optical trap," Physical Review Letters **82**, 1124–1127 (1999).

[34] H. Metcalf and P. van der Straten, *Laser Cooling and Trapping* (New York, N.Y.: Springer-Verlag New York, 1999).

[35] C. Foot, *Atomic Physics* (Oxford, United Kingdom: Oxford University Press, 2007).

[36] R. Loudon, *The Quantum Theory of Light* (Oxford, United Kingdom: Oxford Science Publications, 2000).

[37] P. Pezé, A. Paillous, J. Siffre, and B. Dubreuil, "Quantitative measurements of oxygen atom density using LIF," Journal of Physics D: Applied Physics **26**, 1622–1629 (1993).

[38] D. J. Bamford, "Absolute two-photon absorption and three-photon ionization cross sections for atomic oxygen," Phys. Rev. A **34**, 185–198 (1986).

[39] N. M. Khambatta, J. A. Oertel, R. Silk, L. J. Radziemski, and J. M. Mack, "Absolute excited state and ion densities from two- and three-photon processes in some 6 p levels of atomic krypton," Journal of applied physics **64**, 4809–4814 (1988).

[40] W. Steckelmacher, "Knudsen flow 75 years on: the current state of the art for flow of rarefied gases in tubes and systems," Reports on Progress in Physics **49**, 1083–1107 (1986).

[41] W. Steckelmacher, R. Strong, and M. Lucas, "A simple atomic or molecular beam as target for ion-atom collision studies," Journal of Physics D: Applied Physics **11**, 1553–1566 (1978).

[42] S. Hooker and C. Webb, *Laser Physics* (Oxford, United Kingdom: Oxford University Press, 2010).

[43] N. Ramsey, *Molecular Beams* (Oxford, United Kingdom: Oxford University Press, 1956).

[44] N. J. Mason and W. R. Newell, "Total cross sections for metastable excitation in the rare gases," Journal of Physics B: Atomic and Molecular Physics **20**, 1357–1377 (1987).

[45] J. N. Brunt, G. C. King, and F. H. Read, "A study of resonance structure in helium using metastable excitation by electron impact with high energy resolution," Journal of Physics B: Atomic and Molecular Physics **10**, 433–448 (1977).

[46] J. Dalibard and C. Cohen-Tannoudji, "Laser cooling below the Doppler limit by polarization gradients: simple theoretical models," JOSA B **6**, 2023–2045 (1989).

[47] W. Demtroder, *Atoms, Molecules and Photons* (New York, N.Y.: Springer, 2006).

[48] P. F. Bernath, *Spectra of Atoms and Molecules* (Oxford, United Kingdom: Oxford University Press, 2016).

[49] J.-Y. Zhang and J. Mitroy, "Long-range dispersion interactions. I. Formalism for two heteronuclear atoms," Physical Review A **76**, 022705 (2007).

[50] J.-Y. Zhang, L.-Y. Tang, T.-Y. Shi, Z.-C. Yan, and U. Schwingenschlögl, "Long-range interactions between excited helium and alkali-metal atoms," Physical Review A **86**, 064701 (2012).

[51] M. Doery, E. Vredenbregt, J. Tempelaars, H. Beijerinck, and B. Verhaar, "Long-range diatomic s + p potentials of heavy rare gases," Physical Review A **57**, 3603–3620 (1998).

[52] H. Wang and W. C. Stwalley, "Ultracold photoassociative spectroscopy of heteronuclear alkali-metal diatomic molecules," The Journal of Chemical Physics **108**, 5767–5771 (1998).

[53] D. Comparat, "Improved LeRoy-Bernstein near-dissociation expansion formula, and prospect for photoassociation spectroscopy," The Journal of Chemical Physics **120**, 1318–1329 (2004).

[54] D. M. Mattox, *Handbook of physical vapor deposition (PVD) processing film formation, adhesion, surface preparation and contamination control* (Westwood, N.J.: Noyes Publications, 1998).

[55] M. Bartenstein, A. Altmeyer, S. Riedl, R. Geursen, S. Jochim, C. Chin, J. H. Denschlag, R. Grimm, A. Simoni, E. Tiesinga *et al.*, "Precise determination of ^{6}Li cold collision parameters by radio-frequency spectroscopy on weakly bound molecules," Physical Review Letters **94**, 103201 (2005).

[56] M. Shaffer, G. Ranjit, C. Sukenik, and M. Walhout, "Photoassociative spectroscopy of ultracold metastable argon," Physical Review A **83**, 052516 (2011).

[57] L. E. de Araujo, J. D. Weinstein, S. D. Gensemer, F. K. Fatemi, K. M. Jones, P. D. Lett, and E. Tiesinga, "Two-color photoassociation spectroscopy of the lowest triplet potential of ^{2}Na," The Journal of Chemical Physics **119**, 2062–2074 (2003).

[58] B. Fröhlich, T. Lahaye, B. Kaltenhäuser, H. Kübler, S. Müller, T. Koch, M. Fattori, and T. Pfau, "Two-frequency acousto-optic modulator driver to improve the beam pointing stability during intensity ramps," Review of Scientific Instruments **78**, 043101 (2007).

VITA

Grady R. White
Department of Physics
Old Dominion University
Norfolk, VA 23529

Education

Ph.D. in Physics, Old Dominion University, Norfolk VA, May 2019
M.S. in Physics, Old Dominion University, Norfolk VA, May 2011
B.A. in Physics, St. Mary's College of Maryland, St. Mary's City MD, May 2008

Experience

Graduate Research Assistant in Experimental Ultracold Atomic, Molecular, and Optical Physics, Old Dominion University. Advisor - Dr. Charles Sukenik, May 2011-Present

Course Instructor and Graduate Teaching Assistant at Old Dominion University, August 2009-Present

Research Scientist in Ultracold Atomic Physics at the Naval Air Warfare Center Aircraft Division, Patuxent River NAS, May 2008-August 2009

Typeset using LaTeX.